Nonlinear optics approach towards precision spectroscopy of highly charged ions and nuclei

by

Prannay Balla

A dissertation submitted to the Faculty of
Mathematics, Informatics and Natural Sciences
Department of Physics
for the degree of

DOCTOR RERUM NATURALIUM

UNIVERSITÄT HAMBURG

November 2023

NONLINEAR OPTICS APPROACH TOWARDS PRECISION SPECTROSCOPY OF HIGHLY CHARGED IONS AND NUCLEI

Author: Prannay Balla
ORCID ID: 0000-0003-2428-7918

Uniform Resource Name is urn:nbn:de:gbv:18-ediss-115505

Gutachter/innen der Dissertation:	Dr. Christoph Heyl Prof. Dr. Franz Kärtner
Zusammensetzung der Prüfungskommission:	Dr. Christoph Heyl Prof. Dr. Franz Kärtner Prof. Dr. Markus Drescher Prof. Dr. Daniela Pfannkuche Dr. Andrea Trabattoni
Vorsitzende/r der Prüfungskommission:	Prof. Dr. Daniela Pfannkuche
Datum der Disputation:	21.12.2023
Vorsitzender des Fach-Promotionsausschusses PHYSIK:	Prof. Dr. Markus Drescher
Leiter des Fachbereichs PHYSIK:	Prof. Dr. Wolfgang J. Parak
Dekan der Fakultät MIN:	Prof. Dr.-Ing. Norbert Ritter

Abstract

Spectroscopy of highly charged ions and nuclei is a field with great potential to open new frontiers for precision meteorology, act as a scientific test bed for quantum electrodynamics, and contribute to the advancement of technology in applied physics. However, precision spectroscopy of these species typically requires laser sources with high photon energies and narrow line widths in the vacuum ultraviolet (VUV) part of the electromagnetic spectrum. The aim of this dissertation is to develop key methods which will enable to create a VUV laser source tailored to the demands set by this spectroscopy application.

Laser pulses with a duration of few optical cycles have a key potential for VUV generation, and therefore for spectroscopy of highly charged ions or nuclei. Furthermore, high average power lasers play a key role in addressing narrow transitions. However, laser sources supporting high average power such as Ytterbium-based laser systems, have a pulse duration of a few hundred femtoseconds. It is therefore essential to compress the pulses to a short duration. In this dissertation, we address temporal pulse compression of such high average power laser sources to few cycles.

A well-known demanding objective for VUV spectroscopy is the low energy transition of the Thorium 229 (^{229}Th) nucleus. When this dissertation work started, the energy of this transition was known within a range of 149.7 ± 3.1 nm. However, a laser with a narrow linewidth, high-power and wavelength tunability covering this range is not yet available. This dissertation addresses the development of a high-power frequency comb laser to support tunable VUV generation to drive the low energy nuclear transition of ^{229}Th.

Finally, we discuss a preliminary experiment to investigate the low energy VUV nuclear transition of highly charged ^{229}Th^{89+} ions. This experiment has the potential to locate the low energy nuclear transition of ^{229}Th at a precision two orders of magnitude higher than the currently known uncertainty range.

Zusammenfassung

Die Spektroskopie hochgeladener Ionen und Kerne ist ein Gebiet mit großem Potenzial, neue Grenzen für die Präzisionsmeteorologie zu eröffnen, als wissenschaftlicher Prüfstand für die Quantenelektrodynamik zu dienen und zur Entwicklung von Technologien in der angewandten Physik beizutragen. Allerdings erfordert die Präzisionsspektroskopie dieser Spezies in der Regel Laserquellen mit hohen Photonenenergien und schmalen Linienbreiten im Vakuum-Ultravioletten (VUV) Bereich des elektromagnetischen Spektrums. Das Ziel dieser Dissertation ist die Entwicklung von Schlüsselmethoden zur Herstellung einer VUV-Laserquelle, die auf die Anforderungen dieser Spektroskopieanwendung zugeschnitten ist.

Laserpulse mit einer Dauer von wenigen optischen Zyklen haben ein großes Potenzial für die Erzeugung von VUV-Licht und damit für die Spektroskopie von hochgeladenen Ionen oder Kernen. Darüber hinaus spielen Laser mit hoher mittlerer Leistung eine Schlüsselrolle bei der Untersuchung schmaler Übergänge. Laserquellen mit hoher mittlerer Leistung, wie Ytterbium-basierte Lasersysteme, haben jedoch Pulsdauern von einigen hundert Femtosekunden. Daher ist es notwendig, die Pulse auf eine kurze Dauer zu komprimieren. In dieser Dissertation beschäftigen wir uns mit der zeitlichen Kompression von Pulsen solcher Laserquellen mit hoher mittlerer Leistung auf wenige Zyklen.

Ein bekanntes und anspruchsvolles Ziel für die VUV-Spektroskopie ist der Niederenergieübergang des Thorium 229 (^{229}Th)-Kerns. Zu Beginn der Arbeit an dieser Dissertation war die Energie dieses Übergangs in einem Bereich von 149,7 $\pm$3,1 nm bekannt. Ein Laser mit einer schmalen Linienbreite, hoher Leistung und Wellenlängenabstimmbarkeit, die diesen Bereich abdeckt, ist jedoch noch nicht verfügbar. Diese Dissertation addressiert die Entwicklung eines Hochleistungs-Frequenzkammlaser zur durchstimmbaren VUV-Erzeugung, um den niederenergetischen Kernübergang von ^{229}Th zu treiben.

Schließlich wird ein vorläufiges Experiment zur Untersuchung des niederenergetischen VUV-Kernübergangs von hochgeladenen ^{229}Th^{89+}-Ionen vorgestellt. Dieses Experiment hat das Potenzial, den niederenergetischen Kernübergang von ^{229}Th mit einer Genauigkeit zu lokalisieren, die um zwei Größenordnungen höher ist als der derzeit bekannte Unsicherheitsbereich.

LIST OF PUBLICATIONS

Articles published in peer review journals during this dissertation:

I **Post-compression of picosecond pulses into the few cycle regime**
Prannay Balla, Ammar Bin Wahid, Ivan Sytcevich, Chen Guo, Anne-Lise Viotti, Laura Silletti, Andrea Cartella, Skirmantas Alisauskas, Hamed Tavakol, Uwe Große-Wortmann, Arthur Schönberg, Marcus Seidel, Andrea Trabattoni, Bastian Manschwetus, Tino Lang, Francesca Calegari, Arnaud Couairon, Anne L'Huillier, Cord L. Arnold, Ingmar Hartl, and Christoph M. Heyl
Optics letters, 45(9):2572–2575, 2020.

II **60 fs, 1030 nm fel pump–probe laser based on a multi-pass post-compressed Yb:YAG source**
Anne-Lise Viotti, Skirmantas Alisauskas, Ammar Bin Wahid, Prannay Balla, Nora Schirmel, Bastian Manschwetus, Ingmar Hartl, and Christoph M Heyl.
Journal of synchrotron radiation, 28(1):36–43, 2021.

III **Factor 30 pulse compression by hybrid multi-pass multi-plate spectral broadening**
Marcus Seidel, Prannay Balla, Chen Li, Gunnar Arisholm, Lutz Winkelmann, Ingmar Hartl, and Christoph M Heyl.
Ultrafast Science, 2022

IV **Spectrally tunable high power Yb:fiber chirped pulse amplifier**
Valentina Shumakova, Vito F. Pecile, Jakob Fellinger, Michael Leskowschek, P. E. Collin Aldia, Aline S. Mayer, Lukas W. Perner, Sarper Salman, Mingqi Fan, Prannay Balla, Stéphane Schilt, Christoph M. Heyl, Ingmar Hartl, Gil Porat, and Oliver H. Heckl
Photonics Research, 10(10):2309–2316, 2022.

V **Dispersion engineered multi-pass cell for single stage post-compression of an ytterbium laser**
Laura Silletti, Ammar bin Wahid, Esmerando Escoto, Prannay Balla, Supriya Rajhans, Katinka Horn, Lutz Winkelmann, Vincent Wanie, Andrea Trabattoni, Christoph M. Heyl, and Francesca Calegari
Optics Letters, 48(7):1842–1845, 2023

VI **Ultrafast serrodyne optical frequency translator**
Prannay Balla, Henrik Tünnermann, Sarper H Salman, Mingqi Fan, Skirmantas Alisauskas, Ingmar Hartl, and Christoph M Heyl.
Nature Photonics, 17(2):187–192, 2023

Conference contributions published during this dissertation:

I **Factor 40 pulse post-compression of 200 W in-burst average power pulses via single-stage multi-pass spectral broadening**
Prannay Balla, Ammar Bin Wahid, Ivan Sytcevich, Chen Guo, Anne-Lise Viotti, Laura Silletti, Andrea Cartella, Skirmantas Alisauskas, Hamed Tavakol, Uwe Große-Wortmann, Arthur Schönberg, Marcus Seidel, Andrea Trabattoni, Bastian Manschwetus, Tino Lang, Francesca Calegari, Arnaud Couairon, Anne L'Huillier, Cord L. Arnold, Ingmar Hartl, and Christoph M. Heyl
CLEO: Science and Innovations, page SW3E-8. Optica Publishing Group, 2020.

II **Post-compression of picosecond pulses to four optical cycles via multi-pass spectral broadening**
Prannay Balla, Ammar Bin Wahid, Ivan Sytcevich, Chen Guo, Anne-Lise Viotti, Laura Silletti, Andrea Cartella, Skirmantas Alisauskas, Hamed Tavakol, Uwe Große-Wortmann, Arthur Schönberg, Marcus Seidel, Andrea Trabattoni, Bastian Manschwetus, Tino Lang, Francesca Calegari, Arnaud Couairon, Anne L'Huillier, Cord L. Arnold, Ingmar Hartl, and Christoph M. Heyl
International Conference on Ultrafast Phenomena, pages Tu4B–16. Optica Publishing Group, 2020.

III **Post-compression of picosecond pulses to four optical cycles**
Prannay Balla, Ammar Bin Wahid, Ivan Sytcevich, Chen Guo, Anne-Lise Viotti, Laura Silletti, Andrea Cartella, Skirmantas Alisauskas, Hamed Tavakol, Uwe Große-Wortmann, Arthur Schönberg, Marcus Seidel, Andrea Trabattoni, Bastian Manschwetus, Tino Lang, Francesca Calegari, Arnaud Couairon, Anne L'Huillier, Cord L. Arnold, Ingmar Hartl, and Christoph M. Heyl
High Intensity Lasers and High Field Phenomena, page HTh3B–3. Optica Publishing Group, 2020.

IV **Post-compression of high average power picosecond pulses for few cycle generation and FEL pump-probe experiments**
Anne Lise Viotti, Skirmantas Alisauskas, Prannay Balla, Ammar Bin Wahid, Ivan Sytcevich, Chen Guo, Laura Silletti, Andrea Cartella, Hamed Tavakol, Uwe Große-Wortmann, Arthur Schönberg, Marcus Seidel, Andrea Trabattoni, Bastian Manschwetus, Tino Lang, Francesca Calegari, Arnaud Couairon, Anne L'Huillier, Cord L. Arnold, Ingmar Hartl, and Christoph M. Heyl
EPJ Web of Conferences, volume 243, page 21002. EDP Sciences, 2020.

V **Ultrafast pulse compression in bulk with > 20 times spectral broadening factor from a single stage**
Marcus Seidel, Prannay Balla, Gunnar Arisholm, Lutz Winkelmann, Ingmar Hartl, and Christoph M Heyl.
CLEO: Science and Innovations, pages STh2I–3. Optica Publishing Group, 2021.

VI **Spectral shaping of 100 W Yb:fiber laser system with preservation of the low noise performance**
Vito Fabian Pecile, Valentina Shumakova, Jakob Fellinger, Collin Aldia, Aline Sophie Mayer, Sarper Salman, Mingqi Fan, Prannay Balla, Stephane Schilt, Christoph

Heyl, , Ingmar Hartl, Gil Porat, Oliver Hubert Heckl.
EOS Annual Meeting (EOSAM) 2021, 2021.

VII **Wavelength shifting concept for high power femtosecond lasers**
Prannay Balla, Henrik Tünnermann, Sarper H Salman, Mingqi Fan, Skirmantas Alisauskas, Ingmar Hartl, and Christoph M Heyl
2022 Conference on Lasers and Electro-Optics (CLEO), Optica Publishing Group, 2022,

VIII **Serrodyne optical frequency shifting using a nonlinear multi-pass cell**
Henrik Tünnermann, Balla Prannay, Sarper H Salman, Mingqi Fan, Skirmantas Alisauskas, Ingmar Hartl, and Christoph M Heyl
EPJ Web of Conferences, volume 267, page 02036. EDP Sciences, 2022.

IX **Flexible wavelength shifting of ultrafast lasers at high power levels**
Henrik Tünnermann, Prannay Balla, Sarper H Salman, Mingqi Fan, Mindaugas Mecejus, Ingmar Hartl, and Christoph M Heyl.
Conference on Lasers and Electro Optics/Pacific Rim, page CTuP1C_01. Optica Publishing Group, 2022.

X **Sub-20 fs single stage post-compression of an ytterbium fiber laser**
Laura Silletti, Ammar bin Wahid, Prannay Balla, Esmerando Escoto, Katinka Horn, Vincent Wanie, Andrea Trabattoni, Francesca Calegari, and Christoph M Heyl.
High Intensity Lasers and High Field Phenomena, page HTh5B–3. Optica Publishing Group, 2022.

XI **Smart and agile 88 W Yb-fiber frequency comb laser**
Sarper Salman, Mingqi Fan, Henrik Tünnermann, Prannay Balla, John Darvill, Dominic Laumer, Vito F Pecile, Jakob Fellinger, Valentina Shumakova, Christoph Mahnke, Yuxuan Ma, Christian Mohr, Oliver H Heckl, Christoph M Heyl, Ingmar Hartl
EPJ Web of Conferences, Volume 267, Page 01057. EDP Sciences, 2022.

ACRONYMS

AR anti-reflection

BBO beta barium borate

CEP carrier–envelope phase

CW continuous wave

DCM dispersion compensating mirrors

EM electromagnetic

EOMs electro-optic modulators

ESR experimental storage ring

FEL free electron laser

FL fourier limit

FROG frequency resolved optical gating

FWHM full-width at half-maximum

GDD group delay dispersion

GSI Gesellschaft für Schwerionenforschung

GVD group velocity dispersion

HCF hollow core fibers

HCI highly charged ions

HHG high harmonic generation

HWP half wave plate

IR infrared

LBO lithium triborate

LIDT laser induced damage threshold

MPC multi-pass cell

NALM nonlinear amplifying loop mirror

OPA optical parametric amplification

OSA optical spectrum analyzer

PDH Pound-Drever-Hall

PZT peizoelectric transducer

QED quantum electrodynamics

RF radio frequency

SF-HCF stretched flexible hollow core fibers

SHG second-harmonic generation

SPM self phase modulation

SRS stimulated Raman scattering

THG third harmonic generation

TIA trans-impedance-amplifier

TOD third order dispersion

UV ultraviolet

VUV vacuum ultraviolet

XUV extreme ultraviolet

CONTENTS

1 Introduction 1
1.1 VUV and XUV laser technology . . . 2
1.2 Introduction to nonlinear optical processes and higher order harmonic generation . . . 3
1.3 Laser systems for VUV generation . . . 3
1.4 The Frequency comb . . . 4
1.5 Challenges addressed in this dissertation . . . 5
1.6 Outline . . . 6

2 Theoretical Background 9
2.1 Introduction to ultrashort laser pulses and wave equations . . . 9
2.1.1 Propagation in vacuum . . . 10
2.1.2 Propagation in a dielectric medium . . . 11
2.1.3 Carrier envelope phase and the frequency comb . . . 12
2.2 Nonlinear effects and methods . . . 14
2.2.1 Self phase modulation . . . 15
2.2.2 Pulse post-compression . . . 16
2.2.3 Serrodyne-frequency-shift . . . 17
2.3 Basic properties of an optical resonator . . . 19
2.3.1 Fabry-Pérot cavity . . . 21
2.3.2 Enhancement cavities . . . 22
2.3.3 Multi-pass cells . . . 26
2.4 Nonlinear multi-pass cells . . . 29
2.4.1 Limitations on fluence . . . 29
2.4.2 Limitations on B-integral . . . 30

3 Post-compression of high power lasers using multi-pass cells 33
3.1 Post-compression of picosecond pulse to few cycles . . . 33
3.1.1 Scaling limits of setup for HCF and MPC . . . 35
3.1.2 Experimental setup . . . 36
3.1.3 Results . . . 38
3.1.4 Limitations of the post-compression setup . . . 40
3.2 Post-compression of a high average power frequency comb laser . . . 40

4 Towards the generation of a wavelength tunable VUV frequency comb 43
4.1 Approaches to the development of VUV laser sources . . . 44
4.2 Driving Laser . . . 45
4.3 Serrodyne-frequency-shifting of the high-power driving laser . . . 45

4.3.1 Phase applied by the pulse shaper 46
4.3.2 Spectral shifting 48
4.3.3 Efficiency limitations of the serrodyne-frequency-shift 49
4.3.4 Temporal contrast 51
4.3.5 Coherence 54
4.4 Enhancement cavity 54
4.4.1 Vacuum chamber 55
4.4.2 Gas jet 56
4.4.3 Laser-cavity stabilization 57
4.4.4 Intensity determination at the cavity focus 58
4.4.5 Plasma distortion 61
4.4.6 Out-coupling of VUV radiation from the cavity 61
4.5 A complementary path towards a high average power VUV frequency comb laser 62
4.5.1 SHG and enhancement cavity at 515 nm 63
4.5.2 Non-collinear cavity 64

5 Study of the low energy nuclear transition in ^{229}Th at the ESR ion storage ring **67**
5.1 Low energy nuclear transition in ^{229}Th 67
5.1.1 Low energy nuclear transition in the highly charged ^{229}Th^{90+} and ^{229}Th^{89+} ions 68
5.1.2 Relativistic longitudinal Doppler effect 68
5.2 Experimental setup 69
5.3 Results 70

6 Summary and outlook **71**
6.1 Path towards locating the low energy nuclear transition of ^{229}Th 71
6.1.1 Linewidth of the laser 71
6.1.2 Possible route towards a Watt-class VUV frequency comb laser . 71
6.2 Scientific impact on laser research and development 72
6.2.1 High peak power few cycle lasers 72
6.2.2 Wavelength tunablity of high average/peak power lasers 73

Appendix A Specifications of mirrors used in the MPC for pulse post-compression to few optical cycles **75**

Appendix B In-coupling of the laser into an MPC **77**

Appendix C The influence of pulse shaper dispersion on the laser spectrum **79**

Appendix D Side-band generation for the PDH lock **81**

Appendix E Characteristics of the PZT mount of the enhancement cavity **83**

Appendix F Characteristics of the mirrors used in the enhancement cavities at 1030 nm and 515 nm **85**

Appendix G Serrodyne-shift using broad-bandwidth dielectric mirrors **87**

CHAPTER 1

INTRODUCTION

The aim of precision spectroscopy is to make precise measurements of the physical properties e.g. of atoms and materials, as well as to determine the values of fundamental constants. In the field of precision spectroscopy, our ability to measure the characteristics of materials and fundamental constants of nature is primarily limited by the instruments we have available. The resolving power, which is also known as the fractional spectral resolution or more commonly as resolution ($\delta\nu/\nu$), is a quantity that is useful for quantifying our ability to measure. The development of precision spectroscopy is intrinsically linked to the improvement in resolving power. In this dissertation, we focus our discussion on the resolving power in the context of light sources with wavelengths in the range from 10 nm to 200 nm. After the invention of coherent light sources (in particular the laser[1]) in the 1960's, and the development of wavemeter and optical spectrum analyzer (OSA), by the end of the 1980's, we observed a significant improvement in the resolving power up to 10^{-6} in the infrared (IR), visible and ultraviolet (UV)[2,3,4,5,6,7]. However, the resolving power at shorter wavelengths lagged behind and took longer to reach a similar value. A significant improvement in resolving power at short wavelengths was seen in 2000, when an free electron laser (FEL) was able to achieve a resolving power of 10^{-5} at a wavelength of 19 nm[8].

By the 1990s, the use of phase-coherent frequency chain of oscillators, ranging from a stable reference transition at a microwave frequency (such as caesium) to the optical frequencies, has enabled record high resolving powers of up to 10^{-12}[9]. This was soon followed by the development of the frequency comb laser. This was a bold step towards achieving much higher resolution using a relatively simple design. A frequency comb laser is a type of laser source whose frequency components appear as a fine comb-like structure, with regular intervals between each frequency line. By using a radio or optical reference standard, the location of the comb lines can be accurately determined[10,11]. This fine comb-like line of frequencies has resulted in the ability to reach record resolving powers of 10^{-14} and accurately determine frequencies over wide spectral ranges[12,13,14]. Some notable works based on frequency combs are the experiments on the size of the proton radii[15], development of atomic clocks[16], and dual comb spectroscopy of transitions of molecules[17].

Most precision spectroscopy experiments have been conducted in the IR, visible, and UV. Therefore, certain regions of the electromagnetic (EM) spectrum are still widely unexplored and considered exotic. Two of these regions are referred to as vacuum ultraviolet (VUV) and extreme ultraviolet (XUV). Together, they cover the wavelength ranges from 10 nm to 200 nm. Research focusing on precision spectroscopy in VUV and XUV is crucial, as many transitions in highly charged ions (HCI) and a few nuclear transitions lie in these spectral ranges.

HCIs are ions with several electrons removed from their neutral atom counterparts. The study of highly charged ions and nuclei has seen significant growth in recent years due to the development of ion traps (such as electron beam ion trap[18], cryogenic linear Paul trap[19], etc.,) and ion storage rings[20,21,22,23,24], as these instruments facilitate the storage of ions for a long time (in the order of 10^3 s). There is a tremendous interest in studying HCIs because, with the increasing charge state, they have increasing sensitivity to effects described by quantum electrodynamics (QED)[25]. A notable experiment involving HCIs is the hyperfine measurement involving the transitions of electronic states in lithium like $^{209}Bi^{82+}$ ion. The data obtained from this experiment indicated a large discrepancy from QED predictions, resulting in the ”hyperfine puzzle”[26]. Other experiments include e.g. transition energy measurements of the electronic states in HCIs with one, two or three electrons[27,28,29,30]. In the context of this dissertation, the study of the low energy nuclear transition in ^{229}Th is of interest because, compared to an atom, an atomic nucleus is much smaller and it is thus expected to be more insulated from external influences[31]. In addition, several nuclear transitions have narrow linewidths and a higher transition frequencies than those of atoms and ions that are used to make atomic clocks.[32,33,34]. These properties make the transitions in a nucleus a perfect choice for building a clock.

Sections 1.1, 1.2, 1.3 of this chapter provide an introduction to VUV laser technology. In section 1.4, we provide a brief introduction to frequency combs. In section 1.5 of this chapter, we will review the challenges addressed in this dissertation. Finally, in section 1.6, we discuss the outline of this dissertation.

1.1 VUV and XUV laser technology

he VUV region and the XUV region of the electromagnetic spectrum range from photon energies from 6.2 eV to 12.4 eV (wavelength range from 100 nm to 200 nm) and 10 eV to 124 eV (wavelength range from 10 nm to 124 nm) respectively. The fact that the VUV and XUV regions are still relatively unexplored is partly due to the inability to build a laser directly in these regions of the EM spectrum. Although several transitions are available to facilitate the three- or higher level laser schemes supporting population inversion in this spectral region, the high-power pump needed to achieve a population inversion is not available. The power required to maintain the population inversion scales as $1/\lambda^4$. This means that for the construction of a laser in the VUV and XUV region, a pump is required with a power of 10^2 times higher than for a laser in the IR[35]. A suitable option, however, is to build a VUV and XUV laser by frequency conversion using a nonlinear optical process. For example, the nonlinear process could be a second, third or high-harmonic generation process.

VUV and XUV radiation can also be generated from an FEL and other syncrotron-based radiation sources that have developed in the last few decades. In a FEL, electrons are accelerated to relativistic speeds and interact with the varying magnetic fields, as a result, emitting coherent radiation. In 1971, John M. J. Madey developed the first FEL[36]. The free electron lasers can produce short pulses in the VUV and XUV, with pulse energies reaching a few tens of micro joules. One of the primary limitations for FELs and other radiation sources that use synchrotron technology is that the monochromators used to resolve the EM radiation in the VUV and XUV are usually only able to achieve a resolving power of 10^{-6} [37]. This is several orders of magnitude above the resolution that can be achieved with a frequency comb[37,38].

1.2 Introduction to nonlinear optical processes and higher order harmonic generation

In 1961, the nonlinear conversion to higher frequency EM radiation was observed experimentally in a quartz crystal. Such a process is possible because due to large electric fields, the electric field of the laser pulse polarizes the atoms in a medium[39]. The large electric field causes a nonlinear response of the medium, leading to the generation of harmonics of the fundamental field frequency, such as second-harmonic generation (SHG) or third harmonic generation (THG). Another nonlinear process, in which the polarized atom interacts with the pulse and influences its phase (and amplitude), is called self phase modulation (SPM). As a result, the frequency components of the original pulse change. The nonlinear interaction of high intensity pulses with matter therefore provides a way to change the initial frequency of the laser.

In order to reach the VUV or XUV region of EM spectrum, a nonlinear process is needed to generate higher-order harmonics far beyond the initial laser frequency. Such a process called high harmonic generation (HHG) was discovered in 1987[40,41]. Today, with the HHG process, laser sources can reach even photon energies of a few keV[42,43]. The HHG process is described in detail in section 2.2.

1.3 Laser systems for VUV generation

Up to recently, the most popular lasers used as HHG-Driver lasers for VUV generation were Kerr-lens mode-locked Ti:Sapphire lasers. Kerr-lens mode locking refers to the generation of short pulses with the SPM effect. The Kerr-lens mode-locked Ti:Sapphire lasers have a broad emission spectrum ($\geq$ 200 nm around the 800 nm center wavelength) and therefore provide short pulses (20 fs). However, as much higher average powers are often beneficial, there has been a growing interest in fiber laser systems based on Ytterbium (Yb), Erbium (Er) and Thulium (Th).

Fiber laser systems based on Yb, Er and Th can be pumped with high-power average laser diodes. This property, together with better thermal characteristics, is responsible for the high performance of these laser systems. The Yb-based laser system, which emits light at 1030 nm, is currently the most developed laser system in terms of average power, reaching an average power up to the kW range[44,45]. However, the pulse duration of lasers based on Yb-based amplifiers is limited to a few hundred fs. This is due to the limitation of the bandwidth of the Yb based gain medium. As a result, current laser technology faces a major challenge in building high-average power lasers with a short pulse duration.

A technology known as optical parametric amplification (OPA) has been developed to build short pulse lasers outside the bandwidth of the gain medium. In an OPA, two short pulses of different central frequencies ω_1, ω_2 interact in a nonlinear medium to generate two short pulses with frequencies $\omega_{\text{sum}} = |\omega_1 + \omega_2|, \omega_{\text{difference}} = |\omega_1 - \omega_2|$. OPA has been used to create tunable lasers. However, OPA suffers from the high complexity of the laser system and has limited efficiency[46,47].

Another process that has been investigated to adjust the wavelength of the laser is stimulated Raman scattering (SRS). In this process, a pulse interacts with a material and excites its rotational or vibrational modes. This excitation increases the wavelength of the laser pulses. This process has been used as an extremely flexible method for producing tunable laser light for continuous wave or low-power pulsed lasers. As SRS is relatively broadband, arbitrary wavelengths can also be generated in one or more cascaded Raman lasers. SRS has also been used in hollow core fibers to shift the wavelength of high power lasers[48,49]. However, tunable-wavelength high power femotsecond lasers based on SRS have an efficency $<$40%[50,51,52,53,54]. Therefore, the development of efficient wavelength-tunable high-power lasers remains a challenge for current laser technology. Figure 1.1 presents a schematic of a high power laser system, consisting of post-compression, wavelength-tuning and VUV generation units, for spectroscopy of low energy nuclear transition in ^{229}Th.

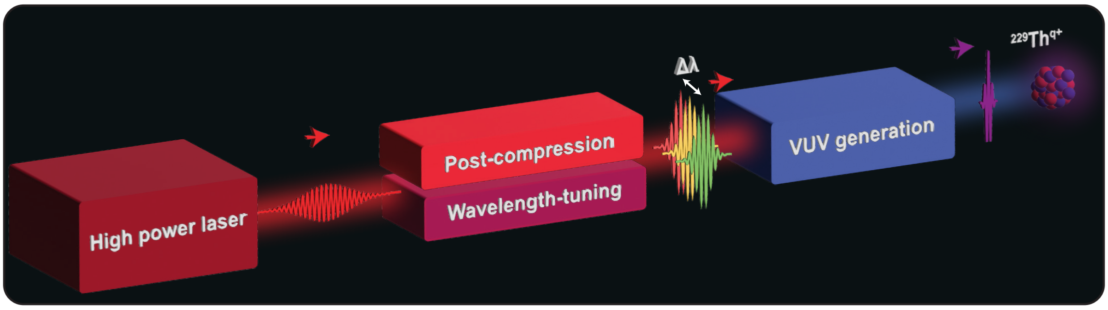

Figure 1.1: Schematic of a VUV frequency comb system, similar to the laser developed in this dissertation, consisting of a high power laser followed by a post-compression unit, a wavelength-tuning unit and a VUV generation unit, for spectroscopy of the low energy nuclear transition in ^{229}Th.

1.4 The Frequency comb

A frequency comb laser is a short pulse laser that has a series of regularly spaced frequency components, similar to the teeth of a comb. Furthermore, each of the comb-like teeth is connected to a radio frequency standard or an optical frequency standard. This means that each frequency component of the frequency comb laser can be determined with an accuracy limited by the radio frequency standard. Since the broadband spectrum of a laser is turned into a comb of narrow lines, a frequency comb laser is ideally suited to directly probe narrow transitions. Another advantage is that each of the comb teeth has a much higher power spectral density than what is typically seen in a broadband femtosecond laser.

Frequency comb lasers are now commonly used in frequency mixing processes to produce lasers of different frequencies in the IR, visible, and UV regions of the EM spectrum. This is possible because the coherence of the frequency comb lasers is maintained during nonlinear frequency mixing. In recent years, experimental evidence has demonstrated that a very highly nonlinear, non-perturbative process, such as HHG, can preserve the coherence of the driver laser[55]. Therefore, the VUV and XUV electric field produced by the HHG process also forms a frequency comb, with the same spacing between adjacent lines in the comb.

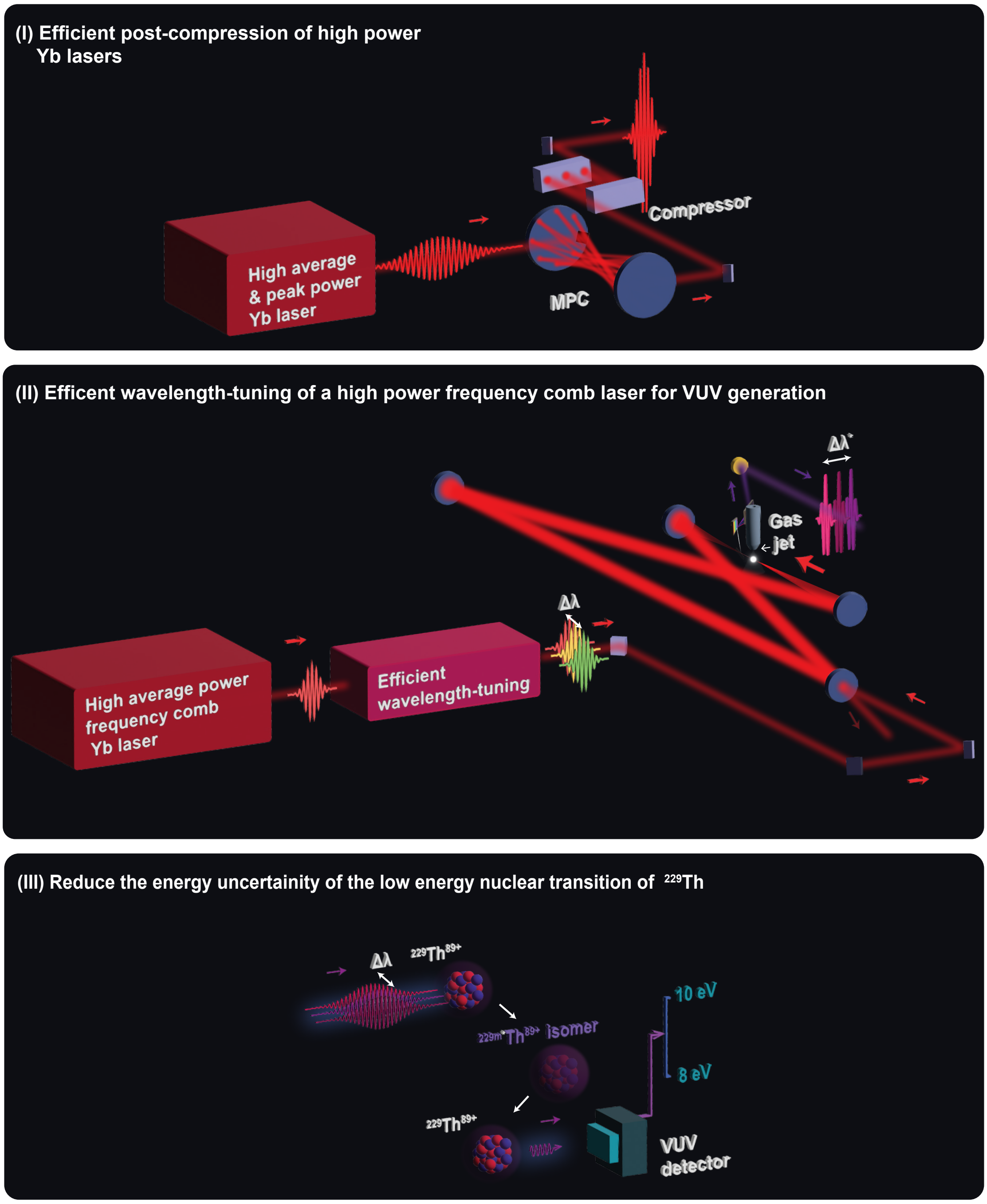

Figure 1.2: Illustration of the challenges addressed in this dissertation.

1.5 Challenges addressed in this dissertation

This section summarizes the key challenges addressed within this dissertation:

- Challenge: "Efficient post-compression of high-power Ytterbium lasers to provide ultrashort pulses for VUV generation": In this dissertation, we identified multi-pass cell post-compression as an important and scalable approach to compress high-power laser pulses. Therefore, in parallel to the development of a VUV source, we develop a method with another laser to compress high-power laser pulses from picoseconds to a few optical cycles.

- Challenge: ”A route to efficiently tune a high average power femtosecond laser while preserving its frequency comb properties”: We develop a method to efficiently shift the wavelength of a high-power frequency comb laser system. At the beginning of the dissertation, the ^{229}Th nucleus was identified a promising spectroscopy target. When this dissertation work started, the energy of this transition was known within a range of 149.7 ± 3.1 nm[32]. Therefore, we develop a wavelength-tunable laser that can be used as a driver laser for VUV generation to perform spectroscopy of the low energy nuclear transition of ^{229}Th.

- Challenge: ”Reduce the energy uncertainty of the low energy nuclear transition in ^{229}Th via direct laser spectroscopy”: We are investigate a method for reducing the energy uncertainty range of the low energy nuclear transition of the ^{229}Th nuclear isomer at the experimental storage ring (ESR) at Gesellschaft für Schwerionenforschung (GSI) located at Darmstadt as part of a greater collaboration.

Figure 1.2 illustrates the above challenges addressed in this dissertation.

1.6 Outline

This section summarises the content of the chapters in this dissertation:

- Chapter 1 of the dissertation summarizes the current state of laser technology in the VUV and XUV. In addition, it describes the challenges that we address in this dissertation.

- In Chapter 2, we discuss the theoretical background to understand the linear and nonlinear effects experienced by laser pulses when propagating in a dielectric medium. In addition, chapter 2 describes the concepts of post-compression and serrodyne-frequency-shift, and introduces the theoretical background for optical cavities used in this dissertation. Finally, chapter 2 provides a brief overview of the nonlinear properties that need to be taken into account when building a multi-pass cell (MPC).

- In Chapter 3, we address the challenge of efficiently post-compressing high peak power Yb based lasers to deliver pulses with a pulse duration of a few optical cycles. We further discuss post-compression of a high average power Yb based fiber laser delivering a pulse with a μJ pulse energy from a pulse duration of 200 fs to sub-40 fs.

- Chapter 4 describes in detail key steps taken toward demonstrating a tunable VUV laser suitable for locating the low energy nuclear transition of ^{229}Th. In sections 4.1, we examine viable approaches to build a suitable VUV laser. In section 4.3, we develop and deploy a method to shift the wavelength of a high-power frequency comb laser. Later in section 4.4, we build an enhancement cavity for VUV conversion. Finally, in section 4.5, we discuss the preliminary steps taken to demonstrate a record high average power VUV frequency comb laser.

- In Chapter 5, we describe an experiment to reduce the energy uncertainty of the low energy nuclear transition in ^{229}Th by direct laser spectroscopy, that is carried out at the ESR in GSI Darmstadt.
- Finally, in chapter 6, we outline the next steps to be taken in order to locate the low energy nuclear transition in ^{229}Th, and review the significance of the methods developed in this dissertation on the research and development of lasers.

CHAPTER 2

THEORETICAL BACKGROUND

To address the challenges mentioned in section 1.5, the concepts of post-compression and enhancement of the peak power of a laser pulse are critical methods. This chapter provides the theoretical background required to understand these concepts in detail. The linear properties of the EM waves are described in section 2.1. Later in section 2.2, we discuss nonlinear effects and methods used in this dissertation to post-compress a high-power Yb based laser and to build a laser suitable for spectroscopy of low energy nuclear transition of ^{229}Th. Since optical resonators and MPCs are the backbone of this dissertation, we examine the principles of these systems and their properties in section 2.3. In section 2.4, we discuss key properties of nonlinear MPCs used for post-compression of high peak power laser pulses.

2.1 Introduction to ultrashort laser pulses and wave equations

An ultrashort laser pulse is a coherent electromagnetic radiation that is confined in space and limited to a short time interval. In this dissertation, an ultrashort laser pulse refers to a pulse with a duration in the range from a few femtoseconds to a few picoseconds. In this section, we briefly introduce the linear effects, such as dispersion and diffraction, that are experienced by such pulses during propagation. The presented derivations closely follows Refs.[56,57].

Maxwell's equations provide a comprehensive description of electromagnetic fields. For a non-magnetic dielectric medium, the Maxwell-Faraday equation and Maxwell-Ampere equation can be written as:

$$\nabla \times \mathbf{E}(x,y,z,t) = -\frac{\partial \mathbf{B}(x,y,z,t)}{\partial t}, \tag{2.1}$$

$$\nabla \times \mathbf{B}(x,y,z,t) = \mu_0 \left(\mathbf{J}(x,y,z,t) + \frac{\partial \mathbf{D}(x,y,z,t)}{\partial t} \right), \tag{2.2}$$

where **E** and **B** are electric and magnetic fields, **D** is the electric displacement field, **J** is the current density, and μ_0 is the vacuum magnetic permeability. In this dissertation, the main factor that contributes to the electric displacement vector is the polarization of the medium, and the main factor contributing to the current density is the free charges generated by plasma formation. The coupled equations (2.1) and (2.2) can be merged in order to obtain equation (2.3):

$$\nabla^2 \mathbf{E}(x,y,z,t) - \nabla\left(\nabla \cdot \mathbf{E}(x,y,z,t)\right) = \mu_0 \left[\frac{\partial \mathbf{J}(x,y,z,t)}{\partial t} + \frac{\partial^2 \mathbf{D}(x,y,z,t)}{\partial t^2} \right]. \tag{2.3}$$

In the Fourier domain, the electric displacement field can be written as:

$$\widetilde{\mathbf{D}}(x,y,z,\omega) = \varepsilon_0 \widetilde{\mathbf{E}}(x,y,z,\omega) + \widetilde{\mathbf{P}}(x,y,z,\omega), \tag{2.4}$$

and the polarization vector can be written as:

$$\begin{aligned} \widetilde{\mathbf{P}}(x,y,z,\omega) &= \widetilde{\mathbf{P}}^{L}(x,y,z,\omega) + \widetilde{\mathbf{P}}^{NL}(x,y,z,\omega), \\ \widetilde{\mathbf{P}}(x,y,z,\omega) &= \varepsilon_0 \chi^{(1)} \widetilde{\mathbf{E}}(x,y,z,\omega) + \widetilde{\mathbf{P}}^{NL}(x,y,z,\omega). \end{aligned} \tag{2.5}$$

Where ε_0 is vacuum electric susceptibility and $\chi^{(1)}$ is first order susceptibility of medium, $\mathbf{P}^L$ and $\mathbf{P}^{NL}$ are the linear and nonlinear components of the polarization vector. Using equations (2.3), (2.4) and (2.5), equation (2.3) can be rewritten in the frequency domain as:

$$\begin{aligned} \nabla^2 \widetilde{\mathbf{E}}(x,y,z,\omega) - \nabla\left(\nabla \cdot \widetilde{\mathbf{E}}(x,y,z,\omega)\right) + \frac{\omega^2 n^2(\omega)}{c^2}\widetilde{\mathbf{E}}(x,y,z,\omega) \\ = \mu_0 \Bigg[- i\omega \mathbf{J}(x,y,z,\omega) - \omega^2 \widetilde{\mathbf{P}}^{NL}(x,y,z,\omega) \Bigg], \end{aligned} \tag{2.6}$$

where $n(\omega)$ is the refractive index of medium and c is the velocity of light in vacuum.

2.1.1 Propagation in vacuum

While propagating in vacuum, due to the absence of a dielectric medium, free charges and currents, equation (2.3) simplifies to a homogeneous wave equation, which can be written as:

$$\nabla^2 \mathbf{E}(x,y,z,t) - \frac{1}{c^2}\frac{\partial^2 \mathbf{E}(x,y,z,t)}{\partial t^2} = 0. \tag{2.7}$$

In order to simplify the mathematical formalism, in the context of this dissertation, let us consider that the EM wave has a linear polarization. For a linearly polarized EM wave, equation (2.6) can be written as a scalar equation by omitting vector fields. Therefore, in the remainder of this chapter we continue to write scalar equations. From the method of separation of variables, commonly used to solve partial differential equations, it is known that the solutions of homogeneous wave equations can be separated into a temporal and spatial component. Therefore, the electric field can be written as $E(x,y,z,t) = E_s(x,y,z)E_t(t)$. The equation (2.7) can therefore be written as:

$$(\nabla^2 + k^2)E_s(x,y,z) = 0, \tag{2.8}$$

$$\left(\frac{\partial^2}{\partial^2 t} + +\omega^2\right)E_t(t) = 0, \tag{2.9}$$

where $k = |\mathbf{k}|$ is the absolute value of the wave vector and $\omega = kc$ is the angular frequency of the EM wave. When the EM wave propagates at small angles close to the optical axis (i.e. $\mathbf{k}.\hat{z} \approx k$), equation (2.8) can be simplified further into a paraxial form, that can be written as:

$$\left(\nabla_\perp^2 - 2ik\frac{\partial}{\partial z}\right)E_s(x,y,z) = 0, \tag{2.10}$$

where $\nabla_\perp^2 = \frac{\partial^2}{\partial^2 x} + \frac{\partial^2}{\partial^2 y}$ is a component of the Laplace operator orthogonal to the optical axis. Solutions to equation (2.10) are called Hermite-Gaussian modes. Most of the effects discussed in this dissertation use the lowest order Hermite-Gaussian mode (also known simply as Gaussian mode). However, in an enhancement cavity, higher order Hermite-Gaussian modes also need to be considered. This is discussed in section 2.3.2. The expression for the spatial beam profile of a Gaussian beam can be written as:

$$E_s(x,y,z) = E_{0s}\frac{w_0}{w(z)}\exp\Big[-\frac{\rho^2}{w^2(z)}\Big]\exp\Big[-ikz - ik\frac{\rho^2}{2R(z)} + i\eta(z)\Big], \tag{2.11}$$

where $\rho = \sqrt{x^2+y^2}$, E_{0s} is the amplitude of the EM wave, and $w(\rho) = w_0\sqrt{1+(z/z_R)^2}$ is the $1/e^2$ beam radius of the intensity profile of the Gaussian beam at position z. The variable $z_R = \pi w_0^2/\lambda$ denotes the Rayleigh length of the Gaussian beam, $R(z) = z\sqrt{1+(z_R/z)^2}$ defines the curvature radius of the wavefront of the Gaussian beam and $\eta(z) = \tan^{-1}(z/z_R)$ is the Gouy phase.

The solution of the temporal part of the homogeneous wave equation (2.9) can be written as $E_t(t) = E_{0t}\exp(i\omega t)$, where E_{0t} is the amplitude of the electromagnetic wave. Based on the principle of superposition, the sum of the monochromatic waves is also a solution to equation (2.9). Hence, the temporal expression of a laser pulse can be written as:

$$E_t(t) = E_0(t)\exp\Big[i\Big(\omega_0 t - \varphi(t)\Big)\Big], \tag{2.12}$$

where $E_0(t)$ is the field envelope. For a Gaussian pulse, the expression for the field envelope is $E_0(t) = E_0\exp\Big(2\ln 2(t-t_0)^2)/\tau^2\Big)$, where τ is the full-width at half-maximum (FWHM) of the pulse duration, t_0 is the location of the center of the pulse in the time domain, ω_0 is the carrier frequency, and $\varphi(t)$ is the time-dependent phase.

2.1.2 Propagation in a dielectric medium

When a pulse is propagated through a dielectric medium, the different frequency components travel at different speeds, resulting in a frequency-dependent wave vector. This phenomenon is called dispersion. To discuss this effect in more detail, let us assume that the intensity of the pulse is low, such that the nonlinear polarization term $P_{NL}(x,y,z,t) \approx 0$. Also, let us assume that there are no free currents, i.e. the current density term $J(x,y,z,t) \approx 0$. Hence, equation (2.3) can be written as:

$$\nabla^2 E(x,y,z,t) - \frac{1}{c^2}\frac{\partial^2 E(x,y,z,t)}{\partial t^2} = \frac{1}{\varepsilon_0 c^2}\frac{\partial P_L(x,y,z,t)}{\partial t^2}, \tag{2.13}$$

where $P_L(x,y,z,t) = \varepsilon_0\chi E(x,y,z,t)$ is a linear component of the polarization vector, and χ is the electric susceptibility. The refractive index of the medium $n(\omega) = \sqrt{1+\widetilde{\chi}(\omega)}$ and the wavevector k is given by:

$$k = \big[\Re\big(n(\omega)\big) + i\Im\big(n(\omega)\big)\big]\frac{\omega}{c}, \tag{2.14}$$

where $\Re(\mathbb{C})$ and $\Im(\mathbb{C})$ are the real and imaginary parts of a complex number $\mathbb{C}$. The amplitude and phase of the pulse changes when it propagates through a dielectric medium, which can be written as:

$$\widetilde{E}_f(\omega) = \widetilde{E}_i(\omega) \exp\Big[ik(\omega)z - \kappa(\omega)z\Big], \tag{2.15}$$

where $\widetilde{E}_i(\omega)$ is the initial electric field, $\widetilde{E}_f(\omega)$ is the electric field after propagating a distance z, $k(\omega) = \Re\big(n(\omega)\big)\frac{\omega}{c}$ and $\kappa(\omega) = \Im\big(n(\omega)\big)\frac{\omega}{c}$. In order to distinguish the different effects that contribute to the change in the phase of the electric field, we perform a Taylor expansion of the wavevector $k(\omega)$ around the carrier frequency, which can be written as:

$$k(\omega) = k_0 + k_1(\omega - \omega_0) + \frac{1}{2!}k_2(\omega - \omega_0)^2 + ... \tag{2.16}$$

The 0^{th} order term $k_0 = \omega_0/c$, is called the phase velocity v_φ. The coefficient of the first-order term, $k_1 = \big(\partial k/\partial\omega\big)\big|\omega_0$, defines the group velocity of the envelope of the electric field, $v_g = 1/k_1$. When $v_g \neq v_\varphi$, the electric field changes relative to the envelope of the pulse during propagation. The coefficient of the second-order term $k_2 = \big(\partial^2 k/\partial\omega^2\big)\big|\omega_0$ is called the group velocity dispersion (GVD), which represent the rate of change of the group velocity of each frequency component.

2.1.3 Carrier envelope phase and the frequency comb

Using equation (2.16), the carrier–envelope phase (CEP) can be defined as:

$$\varphi_{\text{CEO}} = 2\omega_c L\left(\frac{1}{v_g} - \frac{1}{v_p}\right), \tag{2.17}$$

where L is the length of propagation in a dispersive medium and ω_c is the center angular frequency of the pulse. φ_{CEO} provides information about the shape of the electric field in relation to the envelope profile as shown in Figure 2.1.

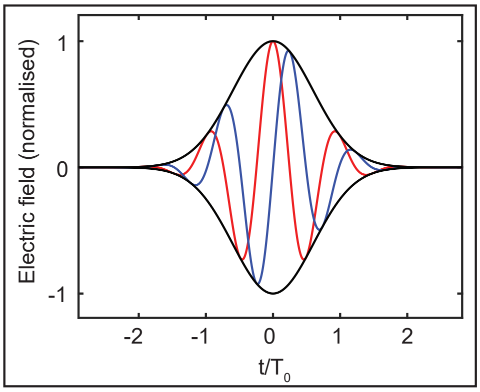

Figure 2.1: Schematic of the electric field of a Gaussian pulse with $\varphi_{\text{CEP}} = 0$ (red), and $\varphi_{\text{CEP}} = \pi/2$ (blue). The envelope of the electric field is shown with a black line. T_0 is the duration of one optical cycle.

The CEP plays an important role for a frequency comb laser. This is because, the CEP, the repetition rate and each of the frequency comb lines in a frequency comb laser are related. The derivations in this section closely follow Refs.[58,59]. The expression for the jth comb line can be written as:

$$\omega_{\mathrm{j}} = \omega_{\mathrm{CEO}} + 2\pi j\, f_{\mathrm{rep}},$$
$$\omega_{\mathrm{CEO}} = \mathrm{mod}(\frac{\varphi_{\mathrm{CEO}}}{2\pi})\ 2\pi f_{\mathrm{rep}}, \tag{2.18}$$

where ω_{CEO} is the carrier envelope offset angular frequency, f_{rep} is the pulse repetition rate, j is a positive integer and ω_j is the angular frequency of the j^{th} comb line in the frequency comb. To understand the role of CEP in a frequency comb, we consider an infinitely long train of equidistant coherent pulses separated by a pulse duration of $1/f_{\mathrm{rep}}$. Let us also consider that the CEP is such that the electric field profile repeats itself after a duration of $2\pi/\omega_{\mathrm{ceo}}$. The expression of the pulse train can then be written as:

$$E(t) = \Sigma_{j=0}^{\infty} A_j e^{-i(\omega_{\mathrm{ceo}}+2\pi\, j\, f_{rep})t} + c.c, \tag{2.19}$$

where A_j is the amplitude of the pulse. By performing a Fourier transformation of equation (2.19), the expression for the pulse train in the frequency domain can be written as:

$$\widetilde{E}(\omega) = \Sigma_{j=0}^{\infty} \widetilde{A}_j \delta\left(2\pi\, j\, f_{\mathrm{rep}} + \omega_{\mathrm{ceo}} - \omega\right). \tag{2.20}$$

From equation (2.20), we observe that the pulse train forms a comb like structure in the frequency domain, and the distance between the adjacent comb teeth is $2\pi f_{\mathrm{rep}}$. Hence, an ultrashort laser with a stabilized ω_{CEO} and f_{rep} is called a frequency comb laser. Figure 2.2 shows an illustration of a frequency comb laser as described by equations (2.19) and (2.20).

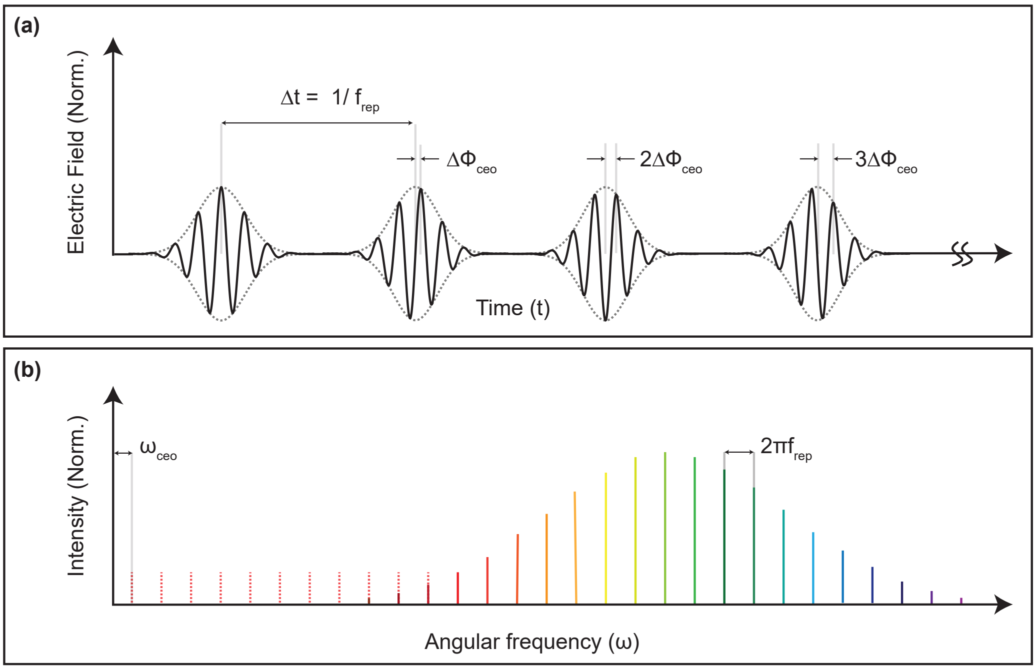

Figure 2.2: An illustration of a frequency comb laser. (a) Temporal profile of the electric field and (b) the intensity profile of the electric field in the frequency domain.

From equation (2.18), we observe that the instability of ω_{ceo} causes an uncertainty in the frequency of the comb teeth. Each comb tooth also has a finite linewidth. The instability of the ω_{ceo} of the laser effectively increases the linewidth of the frequency comb. Therefore, a large instability of the f_{rep} and the ω_{ceo} can render a frequency comb laser unsuitable as a spectroscopy tool. Hence, stabilization of f_{rep} and ω_{ceo} is crucial. Alternatively, a laser can also be stabilized by locking to a stable reference continuous wave (CW) laser. In this dissertation, the f_{rep} of the high power ultrashort frequency comb laser in section 4.2 is stabilized by locking to a stabilized CW laser at 1064 nm. The ω_{CEO} can be stabilized using the self referencing method[58]. In this method, a laser spectrum is first broadened using a nonlinear process called supercontinuum generation[60] in order to generate an octave spanning spectrum. Then, the frequency of a lower frequency comb line is frequency doubled and interfered with a higher frequency comb line in order to obtain a heterodyne beat-signal, whose angular frequency can be written as[58]:

$$\begin{aligned}\omega_{\text{beat-signal}} &= 2\omega_{\text{j}} - \omega_{2\text{j}}, \\ &= 2(\omega_{\text{CEO}} + 2\pi j f_{\text{rep}}) - (\omega_{\text{CEO}} + 4\pi j f_{\text{rep}}), \\ &= \omega_{\text{CEO}}.\end{aligned} \tag{2.21}$$

The heterodyne beat-signal is used stabilize the ω_{CEO}. A detailed description of the stabilization of f_{rep} and ω_{CEO} of the high power ultrashort frequency comb laser discussed in section 4.2 can be found in Ref.[61].

The most common method for broad bandwidth operation and tuning of the wavelength of the ultrashort frequency comb is to use supercontinuum generation[62]. However, tunable-wavelength frequency comb lasers based on supercontinuum generation are limited to a low average power per comb line. Therefore, a method for coherent spectral tuning for high-power ultrashort lasers is needed. This problem is solved with the serrodyne-frequency-shifting-method discussed in section 2.2.3, which provides an effective way to tune the wavelength of high-power frequency comb lasers.

2.2 Nonlinear effects and methods

In order to understand the propagation dynamics of an ultrashort laser pulse, equation (2.6) can be solved using a finite-difference time domain method. However, such calculations are computationally intensive and take a considerable amount of time. Hence, we need to simplify equation (2.6) to reduce the computation time.

Let us assume that the electric field, current density and polarization vector are orthogonal to the direction of propagation. In this case $\nabla(\nabla \cdot \mathbf{E}) = 0$. The operator ∇^2 in equation (2.6) can be expressed as $\partial/\partial^2 z + \Delta_\perp^2$, where $\Delta_\perp^2 = \partial/\partial^2 x + \partial/\partial^2 y$. In the frequency domain, we can rewrite the operator $\Delta_\perp^2$ for an EM wave as a product of forward and backward propagators, $\left(\partial/\partial z + in\omega/c\right)\left(\partial/\partial z - in\omega/c\right)$. These propagators represent the EM waves that propagate along the optical axis in the forward and backward direction respectively. By assuming that the backward propagating component of the EM wave can be neglected, the equation (2.6) can be rewritten as:

$$\frac{\partial}{\partial z}\widetilde{E}(x,y,z,\omega) = ik(\omega)\widetilde{E}(x,y,z,\omega) + \frac{i}{2k(\omega)}\Delta_\perp^2 \widetilde{E}(x,y,z,\omega) - \frac{\mu_0 J(x,y,z,\omega)}{n(\omega)c} + \frac{i\omega}{n(\omega)c}\widetilde{P}^{\text{NL}}(x,y,z,\omega). \tag{2.22}$$

In contrast to equation (2.6), equation (2.22) can be solved using a computationally less intensive finite difference method, such as the Euler method. Since the backward propagating component of the EM wave is ignored, equation (2.22) is called the forward Maxwell equation. In the remaining part of this section, the nonlinear effects that contribute to the polarization vector P^{NL} and the current density J are discussed. The Taylor expansion for the nonlinear polarization term P^{NL} can be written as:

$$P^{\mathrm{NL}}(x,y,z,t) = \varepsilon_0\chi^{(2)}E^2(x,y,z,t) + \varepsilon_0\chi^{(3)}E^3(x,y,z,t) + ... \tag{2.23}$$

In an EM wave, $E(x,y,z,t) \propto e^{i\omega t}$. Hence, the $\mathrm{n^{th}}$ order term of the perturbation expansion in equation (2.23) is proportional to $e^{in\omega t}$. Thus, each of the terms in the Taylor expansion for the nonlinear polarization term are responsible for the production of harmonics of the initial frequency ω. We also note that, since equation (2.23) is a Taylor expansion, each successive term typically comprises a decreasing amplitude with increasing nonlinearity. Hence, in the presence of large electric fields, equation (2.23) is no longer accurate. This is because when the electric field strength is in the order of the coulomb forces exerted by the nucleus on the valance electron, the dipole response of the atom can no longer be describe by a Taylor expansion. In the presence of such large electric fields, high harmonics of the initial frequency are produced by a process known as HHG. An intuitive picture of HHG in monoatomic gases, which can explain the main characteristics observed in experiments, was presented by Paul Corkum[63], complemented by a quantum-mechanical model by Maciej Lewenstein[64]. The process of HHG can be described briefly in three steps as:

- Step 1: An atom is ionized by an intense laser field.
- Step 2: In the electromagnetic field of the laser, the electron accelerates. Since the electric field of a laser oscillates, the electron returns to the ion.
- Step 3: The electron and ion recombine and the excessive energy that the electron possesses is released as a photon.

A quantitative description of the HHG process can be found in Ref.[64]. In this dissertation, we take steps to develop a VUV laser by ultizting 7^{th} harmonic generation of a 1030 nm high power driving laser in a gas in section 4.4. However, 7^{th} harmonic generation is located in the region that is in-between the perturbative process described by the Taylor expansion and the quantum mechanical model used to describe the HHG process, a regime which still lacks in-depth exploration[65].

2.2.1 Self phase modulation

The atoms of a solid or gas get polarized in the presence of an intense electric field. In an isotropic medium, the second-order electric susceptibility os: $\chi^{(2)} = 0$. As a result, we do not observe SHG or OPA in an isotropic material. The next significant contribution is therefore the macroscopic 3^{rd} order polarization term, which causes SPM. When an intense ultrashort pulse travels through a medium, it will induce a varying refractive index due to the macroscopic 3^{rd} order polarization term. This varying refractive index, also known as the optical Kerr effect, can be written as:

$$n(x,y,z,t) = n_0 + n_2\frac{1}{2}\varepsilon_0 c n_0|E(x,y,z,t)|^2, \tag{2.24}$$

where $n_0 = \sqrt{1 + \chi^{(1)}}$, and the nonlinear refractive index coefficient $n_2 = 3\chi^{(3)}/4\varepsilon_0 c n_0^2$. The varying refractive index in return influences the pulse by introducing a nonlinear phase φ_{SPM} that is dependent on the intensity of the pulse, and can be written as:

$$\begin{aligned}
\varphi_{SPM}(x, y, z, t) &= \varphi_{total}(x, y, z, t) - \varphi_{linear}(x, y, z, t), \\
\varphi_{SPM}(x, y, z, t) &= \left[\omega_0 t - k(x, y, z, \omega_0)z\right] - \left[\omega_0 t - k_0(\omega_0)z\right], \\
&= z\left[k_0(\omega_0) - k(x, y, z, \omega_0)\right], \\
&= -\frac{\pi n_2 \varepsilon_0 c^2}{\lambda_0}|E(x, y, z, t)|^2 z.
\end{aligned} \tag{2.25}$$

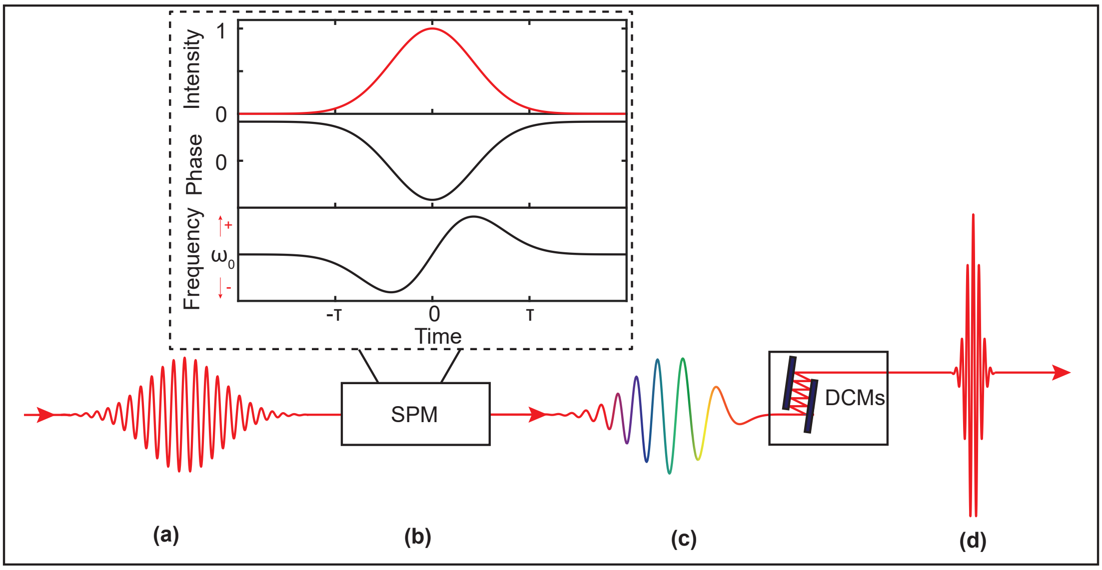

Figure 2.3: Schematic of pulse post-compression: DCMs dispersion compensating mirrors. The figure shows that a Fourier limited Gaussian pulse (a) acquires spectral components in the presence of SPM (b). The spectrally broadened pulse (c) is compressed (with a compressor made of e.g. dispersive mirrors) to obtain a post-compressed pulse (d).

2.2.2 Pulse post-compression

Post-compression refers to a process of compressing the temporal duration of a pulse below the fourier limit (FL), which is defined by the spectral bandwidth. SPM is an extremely useful process for post-compression because the nonlinear phase imprinted by SPM increases the bandwidth and thus reduces the achievable pulse duration to a value below the initial FL.

Figure 2.3 shows an illustration of the post-compression process. In Figure 2.3 (a), we see the electric field of a Gaussian pulse entering a nonlinear medium. SPM in the nonlinear medium causes the pulse to acquire the nonlinear phase φ_{SPM} defined by equation (2.25). This nonlinear phase is shown in Figure 2.3 (b). The instantaneous frequency components of the pulse are obtained by taking the derivative of the phase, as shown in the bottom plot in the panel in Figure 2.3 (b). Due to the nonlinear phase acquired by the pulse, the spectrum broadens, and the FL of the pulse decreases. As shown in Figure 2.3 (c), the leading part of the pulse contains the lower frequency components of the electric field, and the trailing part of the pulse contains higher frequency components of the electric field. It should be noted that the duration of the pulse remains almost the same as the input pulse. However, the temporal duration of the pulse can vary depending on the setup of the experiment. Then the pulse can be compressed using dispersion compensating mirrors (DCM) or a grating compressor and a post-compressed pulse can be obtained, as shown in Figure 2.3 (d).

When a pulse propagates in a medium, while SPM causes the spectrum to broaden, the linear properties of the medium, such as dispersion and diffraction, also play a critical role in determining the spectral broadening process.

The dispersion of the medium can contribute to a phase that influences the temporal duration of the pulse, as described in section 2.1.2. When the pulse experiences normal dispersion, the pulse gains a spectral phase due to the GVD of the medium. For long propagation distances in a dispersive medium, dispersion leads to a longer pulse duration, thereby reducing the peak intensity of the pulse. The reduction of the peak intensity of the pulse leads to a reduction in the nonlinear phase acquired due to SPM[66,67]. Therefore, we will see ineffective post-compression. On the other hand, when the pulse experiences anomalous dispersion, the pulse gains a spectral phase that can compensate the spectral phase acquired by SPM. This can lead to pulse compression while the pulse undergoes spectral broadening, which effectively increases the nonlinear phase acquired by SPM when propagated further[68,69]. It should also be noted that, depending on the experimental setup and the nonlinear medium used for spectral broadening, it is also possible that the pulse accumulates an excessive negative chirp when propagating in medium providing an anomalous dispersion, leading to a longer temporal pulse duration and thus a decrease in the nonlinear phase acquired by SPM. In a recent work by N. Daher et al, the authors have used a negatively chirped input pulse in a post-compression setup to obtain a narrower output spectrum[70]. The management of dispersion is therefore important for effective post-compression.

The nonlinear phase introduced by SPM causes focusing of the pulse in the transverse dimensions and can lead to filamentation if the peak intensity at the focus is greater than the critical intensity[56]. Therefore, the management of diffraction is important for effective post-compression. In order to reduce undesired diffraction, a guiding structure such as a waveguide, a capillary or a quasi-guiding structure is used during post-compression. The quasi-guiding structure used for post-compression in this dissertation is an MPC. The properties of MPCs are discussed in detail in section 2.3.3. We choose an MPC in this dissertation because it has several advantages compared to other guiding/ quasi-guiding structures available for post-compression such as a dispersion control, high efficiency and an ability to build a smaller setup size for large compression ratios[71,72,73]. The advantages of using MPCs compared to other guiding / quasi-guiding structures available for post-compression are discussed in detail in section 3.1.

2.2.3 Serrodyne-frequency-shift

The serrodyne principle states that applying a linear phase in the time domain for a given signal leads to a shift in frequency. Raymond C. Cumming first explained this principle

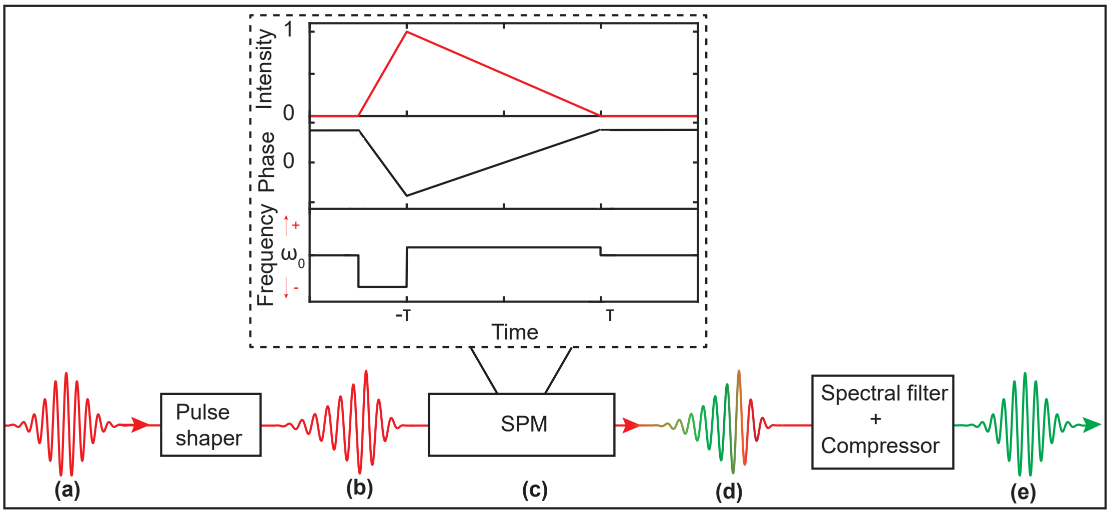

Figure 2.4: Schematic of the frequency shift of an ultrashort pulse using serrodyne principle. The figure shows that the waveform of a pulse (a) is tailored to a triangular shape approaching a sawtooth profile (b). The spectral components of the tailored pulse (b) undergo a frequency shift in the presence of a nonlinear medium via SPM (c). The spectrally shifted pulse (d) is filtered to remove undesirable spectral components and compressed to obtain a spectrally shifted pulse (e).

in his seminal paper in 1957 [74]. In this paper, Cumming used the method for the translation of amplitude and frequency-modulated waves in the radio frequency (RF) spectrum. Shortly after Cumming's paper, in 1959, H. Scharfman and F. J. O. Hara introduced the serrodyne principle in the microwave domain of the EM spectrum [75]. With the advent of electro-optic modulators (EOMs), the serrodyne principle was also applied by K. Wong and S. Wright in the optical domain to CW lasers in 1981 [76]. Over the last two decades, the frequency of CW lasers has been shifted by a few GHz using the serrodyne principle [77,78,79,80]. In all of the above works, a direct linear phase modulation was used to shift the frequency of the EM wave. However, the application of a direct phase modulation to a laser pulse with high peak and high average power is not feasible with devices such as EOMs. Furthermore, in this dissertation, we need to shift the frequency of a laser by several THz, in order to cover the energy range of the low energy nuclear transition of ^{229}Th [32]. Hence, here we extend the serrodyne principle by translating an ultrashort amplitude modulation via SPM into a phase modulation, thereby reaching a much steeper modulation ramp and thus a larger frequency shift.

Figure 2.4 illustrates the serrodyne-frequency-shift process for an ultrashort pulse. In Figure 2.4 (a), a pulse enters a pulse shaper that tailors the electric field. Figure 2.4 (b) shows a pulse, whose intensity profile is approximately tailored to a sawtooth profile. We here consider for simplicity that the intensity profiles of the leading and trailing sides of the pulse have a linear slope. Figure 2.4 (b) shows a sawtooth pulse with most of the pulse energy located on the trailing side of the pulse. We consider the medium provides a net zero dispersion to avoid the change in shape of the waveform during pulse propagation. Due to the SPM in the medium, both the leading side and the trailing side of the electric field acquire a linear phase in time, as shown in the panel in Figure 2.4 (c). The derivative of the phase plotted in the panel in Figure 2.4 (c) shows that both the leading and the trailing parts of the pulse acquire a frequency shift. We note that the leading side of the pulse receives a negative frequency shift, know as a red shift, and the trailing side of the pulse receives a positive frequency shift, also known as a blue shift. This is illustrated in Figure 2.4 (d). Since most pulse energy is located on the trailing side, we find that most frequency components of the pulse contain the blue-shifted frequency components. Thus, by filtering unwanted spectral components present in the leading side of the pulse and then compensating the undesired remaining spectral phase with dispersive optical elements, we can obtain a frequency-shifted pulse, as shown in Figure 2.4 (e).

Similar to pulse post-compression, the management of dispersion is crucial for the effective shifting of the frequency of a pulse. The reason for this is that the dispersion can distort the waveform of the pulse from a sawtooth shape, leading to an ineffective frequency shift. The ideal landscape of dispersion for a serrodyne-frequency-shift is the absence of dispersion. This is a crucial aspect that needs to be taken into account when designing the guiding / quasi-guiding structure used to support pulse propagation in the medium that provides SPM. In guiding structures, such as capillaries or hollow core fibers, material dispersion typically prevents zero dispersion. An MPC, on the other hand, can provide a net-zero dispersion characteristic by using dispersion-engineered optical elements. Therefore, the MPC is a crucial element in the experiment setup required for serrodyne-frequency-shift.

In order to achieve the maximum efficiency through the serrodyne-frequency-shifting method, the corresponding slanted side of the tailored waveform should contain the maximum pulse energy. This would mean the opposite side should have the lowest energy possible, i.e., a steep edge. However, an ultrashort pulse with a very steep edge would produce frequency components during the serrodyne-frequency-shift, which are far from the frequency components of the initial frequency of the pulse. Therefore, while choosing the steepness of the steep edge of the pulse, we need to consider that the guiding/ quasi-guiding structure used to support the medium that provides SPM also ideally supports all the required frequency components generated during the serrodyne-frequency-shift, while fulfilling a net zero dispersion requirement for all frequency components during the pulse propagation. If not all frequency components generated during the serrodyne-frequency-shift are supported by the guiding structure, the intensity profile of the pulse will change during propagation, limiting the efficient of the serrodyne-frequency-shift. For example, technological limitations make it impossible to find mirrors with infinite spectral bandwidth in an MPC. Therefore, the temporal pulse shape needs to be optimized taking into account bandwidth and dispersion characteristics of the wave guide of the MPC.

In this dissertation, we use the serrodyne-frequency-shift to develop a wavelength-tunable driver laser for VUV generation discussed in section 4.3.

2.3 Basic properties of an optical resonator

Optical cavities (also know as resonators) are essential tools used in this dissertation. In an optical cavity, a pulse can be confined, leading to clearly defined modes in spatial (also referred to as transverse) and / or temporal (also referred to as longitudinal) dimensions.

The ray transfer matrix formalism (also known as ABCD matrix formalism) offers a simple approach to derive the conditions necessary for the formation of a cavity. Furthermore, the ray transfer matrix helps us to understand the similarities and differences between different cavities. The derivation of the stabity condition for a resonator in this section closely follows Ref.[81]. Consider an optical resonator described by the following general ray transfer matrix:

$$\mathbf{M} = \begin{bmatrix} A & B \\ C & D \end{bmatrix}. \tag{2.26}$$

where the matrix **M** is normalized such that determinant $|\mathbf{M}| = 1$ (i.e. $AD - BC = 1$). In order to derive the stability conditions for a resonator, we solve for the eigenvalues of matrix **M** using the equation: $\mathbf{M}\,\mathbf{I} = \mathrm{m}_{1,2}\,\mathbf{I}$, where **I** is a second order identity matrix and $\mathrm{m}_{1,2}$ are the eigenvalues. The eigenvalues $\mathrm{m}_{1,2}$ can be written as:

$$\mathrm{m}_{1,2} = \frac{A+D}{2} \pm \sqrt{(\frac{A+D}{2})^2 - 1}. \tag{2.27}$$

Let us consider the case where $|A + D| \leq 2$. In this case, we can write $(A + D)/2 = \cos(\theta)$, where θ is an angular variable. The eignvalues $\mathrm{m}_{1,2}$ can be written as:

$$\mathrm{m}_{1,2} = \cos(\theta) \pm i\sin(\theta) = e^{\pm i\theta}. \tag{2.28}$$

The displacement vector $\mathbf{r}_n$ of a ray after making n round trips in the resonator can be written as:

$$\mathbf{r}_n = c_1\mathbf{r}_1 e^{in\theta} + c_2\mathbf{r}_2 e^{-in\theta}, \tag{2.29}$$

where $\mathbf{r}_{1,2}$ are the eigenvectors corresponding to the eignvalues $\mathrm{m}_{1,2}$, and $c_{1,2}$ are constants. Equation (2.29) can be written as:

$$\mathbf{r}_n = \mathbf{r}_a \cos(n\theta) + \mathbf{r}_b \sin(n\theta), \tag{2.30}$$

where $\mathbf{r}_a = (c_1\mathbf{r}_1 + c_2\mathbf{r}_2)/2$ and $\mathbf{r}_b = i(c_1\mathbf{r}_1 - c_2\mathbf{r}_2)/2$. From equation (2.30), we observe that the maximum value of the displacement vector has an upper limit of $\mathbf{r}_a + \mathbf{r}_b$ and is independent of the number of round trips thorough the optical resonator. Hence, when the condition $|A+D| \leq 2$ is fulfilled, the ray matrix **M** represents a stable optical resonator that can support transverse modes.

A complex parameter q, which is useful to derive the properties of the beam in a resonator, such as the radii of curvature of the wavefront of the optical beam $R(z)$, and the beam size $w(z)$, can be written as[82]:

$$\frac{1}{q} = \frac{1}{R(z)} - i\frac{\lambda}{\pi n w(z)^2}, \tag{2.31}$$

where λ is the the wavelength of the transverse optical mode and n is the refractive index. To derive the transverse properties of the optical beam, we can use the fact that for certain eignmodes, the q parameter for a cavity would repeat after a round trip[82], which can be written as:

$$\begin{bmatrix} q \\ 1 \end{bmatrix} = M \begin{bmatrix} q \\ 1 \end{bmatrix} \tag{2.32}$$

In the remainder of this section, we discuss the longitudinal and transverse modes formed in Fabry-Pérot cavities, enhancement cavities and MPCs.

2.3.1 Fabry-Pérot cavity

A Fabry-Pérot cavity is an optical cavity formed by two parallel optical surfaces. The Fabry-Pérot cavity is one of the first optical cavities described in the literature. Charles Fabry and Alfred Perot have investigated Fabry-Pérot cavity in two seminal papers in 1899[83,84]. The derivations in this section closely follow Ref.[85]. To understand the properties of a Fabry-Pérot cavity, let us consider a cavity formed in an etalon of thickness l, whose ray transfer matrix can be written as:

$$\mathbf{M} = \begin{bmatrix} 1 & l \\ 0 & 1 \end{bmatrix}. \tag{2.33}$$

We observe that the ray transfer matrix of an etalon satisfies the stability condition as $|A + D| = 2$. However, the cavity is on the edge of the stability zone, which means that stable mode formation cannot be guaranteed. Let us consider that the surfaces of the etalon have a reflectivity of R_1, R_2 for the intensity. When an ultrashort pulse $E_{\text{in}}(\omega)$ enters the resonator formed by the etalon, the electric field in the etalon ($E_{\text{etalon}}(\omega)$) and the electric field transmitted through the etalon ($E_{\text{transmitted-etalon}}(\omega)$) can be written as:

$$\begin{aligned} E_{\text{etalon}}(\omega) &= E_{\text{in}}(\omega)\sqrt{(1-R_1)}\left[1 + \sqrt{R_1R_2}e^{i\varphi(\omega)} + (\sqrt{R_1R_2})^2 e^{2i\varphi(\omega)} + \ldots\right], \\ E_{\text{transmitted-etalon}}(\omega) &= E_{\text{in}}(\omega)\sqrt{(1-R_1)}\sqrt{(1-R_2)}E_{\text{etalon}}(\omega), \end{aligned} \tag{2.34}$$

where $\varphi(\omega)$ is the phase shift experienced by the electric field after one round trip. This phase shift includes the phase accumulated during propagation and also the dispersive effects of the reflective coatings. The term $\varphi(\omega)$ can be written as:

$$\varphi(\omega) = 2l\frac{\omega}{c} + \varphi_d(\omega), \tag{2.35}$$

where $\varphi_d(\omega)$ is the dispersion due to the medium and the dielectric coatings. Equation (2.34) can be written as:

$$\begin{aligned} E_{\text{etalon}}(\omega) &= E_{\text{in}}(\omega)\frac{\sqrt{(1-R_1)}}{1-\sqrt{R_1R_2}e^{i\varphi(\omega)}}, \\ E_{\text{transmitted-etalon}}(\omega) &= E_{\text{in}}(\omega)\frac{\sqrt{(1-R_1)}\sqrt{(1-R_2)}}{1-\sqrt{R_1R_2}e^{i\varphi(\omega)}}. \end{aligned} \tag{2.36}$$

Hence, the intensities of the electric field in the etalon ($I_{\text{etalon}}(\omega)$ and of the electric field transmitted through the etalon $I_{\text{transmitted-etalon}}(\omega)$ are given by:

$$\begin{aligned} I_{\text{etalon}}(\omega) &= I_{\text{in}}(\omega)\frac{(1-R_1)}{(1-\sqrt{R_1R_2})^2 + 4\sqrt{R_1R_2}\sin^2\varphi(\omega)/2}, \\ I_{\text{transmitted-etalon}}(\omega) &= I_{\text{in}}(\omega)\frac{(1-R_1)(1-R2)}{(1-\sqrt{R_1R_2})^2 + 4\sqrt{R_1R_2}\sin^2\varphi(\omega)/2}. \end{aligned} \tag{2.37}$$

From equation (2.37), we note that when $\varphi(\omega) = 2m\pi$ (where m is a positive integer), $I_{\text{transmitted-etalon}}(\omega)$ reaches a maximum, and when $\varphi(\omega) = (2m+1)\pi$, $I_{\text{transmitted-etalon}}(\omega)$ reaches a minimum. Hence, the Fabry Pérot cavity acts as spectral filter. The two maxima of $I_{\text{transmitted-etalon}}(\omega)$ are separated by a frequency spacing $\delta\omega_{\text{fsr}} = 2l/c$, which is called the free spectral range. The frequency interval ω_{FWHM}, which corresponding to an FWHM of a peak of $I_{transmitted-etalon}(\omega)$ is given by:

$$\delta\omega_{\text{FWHM}} = 4\sin^{-1}\left(\frac{1-\sqrt{R_1R_2}}{2\sqrt{\sqrt{R_1R_2}}}\right)\frac{c}{l} \approx \left(\frac{1-\sqrt{R_1R_2}}{\sqrt{\sqrt{R_1R_2}}}\right)\frac{2c}{l}. \tag{2.38}$$

The ratio of the frequency interval $\delta\omega_{\text{fsr}}$ and $\delta\omega_{\text{FWHM}}$ is called Finesse $\mathscr{F}$, and is given by:

$$\mathscr{F} = \frac{\delta\omega_c}{\delta\omega_{\text{FWHM}}} = \frac{\pi R_1 R_2{}^{1/4}}{1-\sqrt{R_1R_2}}. \tag{2.39}$$

2.3.2 Enhancement cavities

An enhancement cavity is a resonator in which the electric field can be enhanced by several orders of magnitude by using the temporal and spatial confinement of EM radiation. A typical high average power frequency comb laser, such as the one described in this dissertation in section 4.2, delivers ultrashort pulses with μJ pulse energies and several tens of Watts of output power. With these parameters, it is not possible to achieve the intensities necessary to generate high-order harmonics for VUV production. Hence, an enhancement cavity is a critical tool to increase the intensities of ultrashort pulses. An introduction of the applications of enhancement cavities in the context of this dissertation is discussed in section 4.4. The derivation of the properties of an enhancement cavity in the remainder of this section closely follows Ref.[55]. In order to understand its properties, let us consider an enhancement cavity as shown in Figure 2.5.

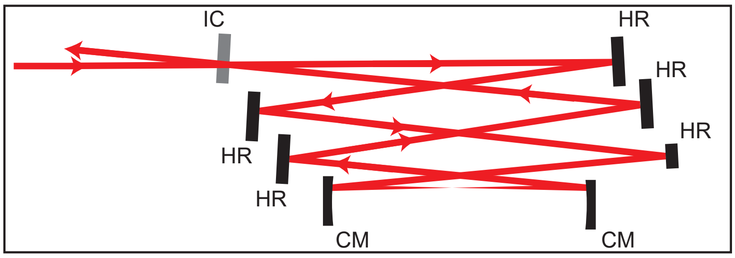

Figure 2.5: A schematic of an enhancement cavity built with 8 mirrors. HR: high reflection mirror with low losses, CM: curved mirror, IC: input coupler.

Consider R_i as the reflectivity of the input coupler, and T_i as the transmittivity of the input coupler. And let R_m be the effective reflectivity of the remaining optics in the cavity. The electric field in the enhancement cavity $E_{\text{ec-cavity}}(\omega)$, and the reflected electric field at the input coupler $E_{\text{ec-ref}}$ can be written as:

$$\begin{aligned} E_{\text{ec-cavity}}(\omega) &= \sqrt{\alpha}E_{\text{in}}(\omega)\sqrt{T_i}\left[1+\sqrt{R_iR_m}e^{i\varphi_{\text{ec}}(\omega)}+(\sqrt{R_iR_m})^2e^{2i\varphi_{\text{ec}}(\omega)}+(\sqrt{R_iR_m})^3e^{3i\varphi_{\text{ec}}(\omega)}+...\right],\\ E_{\text{ec-ref}}(\omega) &= -\sqrt{\alpha}E_{\text{in}}\sqrt{R_i}+\sqrt{\alpha}E_{\text{in}}(\omega)T_i\left[\sqrt{R_iR_m}e^{i\varphi_{\text{ec}}(\omega)}+(\sqrt{R_iR_m})^2e^{2i\varphi_{\text{ec}}(\omega)}+...\right], \end{aligned} \tag{2.40}$$

where $\varphi_{\text{ec}}(\omega)$ is the phase shift of the the electric field after propagating one round trip in the cavity. In order to take into account the fact that the spatial profile of the input laser beam and the cavity are not always perfectly aligned, we introduce a parameter α

in the equation (2.40). The value of α varies between 0 and 1, where $\alpha = 1$ corresponds to the case where the transverse profile of the input laser beam is perfectly matched to the cavity eigenmode. The expressions for the electric fields $E_{\text{ec-cavity}}$ and $E_{\text{ec-ref}}$ can be rewritten as:

$$\begin{aligned} E_{\text{ec-cavity}}(\omega) &= \sqrt{\alpha} E_{\text{in}}(\omega) \frac{\sqrt{T_i}}{1 - \sqrt{R_i R_m} e^{i\varphi_{\text{ec}}(\omega)}}, \\ E_{\text{ec-ref}}(\omega) &= \sqrt{\alpha} E_{\text{in}}(\omega) \frac{\sqrt{R_m} T_i e^{i\varphi(\omega)} - \sqrt{R_i}}{1 - \sqrt{R_i R_m} T_i e^{i\varphi_{\text{ec}}(\omega)}}. \end{aligned} \tag{2.41}$$

The corresponding intensities of the electric fields $I_{\text{ec-cavity}}$ and $I_{\text{ec-ref}}$ can be written as:

$$\begin{aligned} I_{\text{ec-cavity}}(\omega) &= \alpha I_{\text{in}}(\omega) \frac{T_i}{(1 - \sqrt{R_i R_m})^2 + 4\sqrt{R_i R_m} \sin^2 \varphi_{\text{ec}}(\omega)/2}, \\ I_{\text{ec-ref}}(\omega) &= \alpha I_{\text{in}}(\omega) \frac{(\sqrt{R_i} - \sqrt{R_m})^2 + 4\sqrt{R_i R_m} \sin^2 \varphi_{\text{ec}}(\omega)/2}{(1 - \sqrt{R_i R_m})^2 + 4\sqrt{R_i R_m} \sin^2 \varphi_{\text{ec}}(\omega)/2}, \end{aligned} \tag{2.42}$$

where the phase shift $\varphi_{\text{ec}}(\omega)$ is given by:

$$\varphi_{\text{ec}}(\omega) = \frac{\omega}{c} L + \varphi_d(\omega), \tag{2.43}$$

where L is the round-trip length of the enhancement cavity and φ_d is the phase shift due to dispersion in the cavity. Similar to the Fabry Pérot cavity, the intensity of the electric field in the enhancement cavity $I_{\text{ec-cavity}}$ reaches maximum when $\varphi_{\text{ec}}(\omega) = 2m\pi$, and reaches minimum when $\varphi_{\text{ec}}(\omega) = (2m+1)\pi$. Therefore, the enhancement cavity provides enhancement for certain spectral components within the enhancement cavity that satisfy $\varphi_{\text{ec}}(\omega) = 2m\pi$. The free spectral range $\delta\omega_{\text{ec-fsr}}$ of an enhancement cavity can be written as:

$$\delta\omega_{\text{ec-fsr}} = \frac{2\pi c}{L}. \tag{2.44}$$

Hence, by choosing the length of the enhancement cavity such that $\delta\omega_{\text{ec-fsr}} = 2\pi f_{\text{rep}}$, we can ensure that all comb lines of a frequency comb laser are enhanced within the enhancement cavity. It should be noted that the dispersion inside the cavity can prevent the enhancement of all comb modes simultaneously as the phase term defined in equation (2.43) becomes frequency dependent. The expression for finesse of an enhancement cavity is given by:

$$\mathscr{F}_{\text{ec}} = \frac{\pi (R_i R_m)^{1/4}}{1 - \sqrt{R_i R_m}} \tag{2.45}$$

In this dissertation, the enhancement cavity built later in section 4.4 consists of an input coupler with a reflectivity of 98.5083 % and seven highly reflectivity mirrors with a reflectivity of 99.9975 % at 1030 nm center wavelength. The theoretical finesse expected for this cavity in vacuum is 413.2. Since one of the primary uses of an enhancement cavity is to enhance the electric field of a given laser, it is much more useful to rewrite the Finesse of enhancement cavity ($\mathscr{F}_{\text{ec}}$) in terms of losses of optical elements. Let $\mathcal{L}_i$ and

$\mathcal{L}_{\text{cavity}}$ denote the losses in the input coupler and all other mirrors in the enhancement cavity. The expression for $\mathscr{F}_{\text{ec}}$ in terms of losses of optical elements can be written as:

$$\begin{aligned}
\mathscr{F}_{\text{ec}} &= \frac{\pi(R_i R_m)^{1/4}}{1-\sqrt{R_i R_m}}, \\
&= \frac{\pi\big((1-\mathcal{L}_i)(1-\mathcal{L}_{cavity})\big)^{1/4}}{1-\sqrt{(1-\mathcal{L}_i)(1-\mathcal{L}_{cavity})}}, \\
&\approx \frac{\pi}{\left|1-(1-\frac{1}{2}(\mathcal{L}_i+\mathcal{L}_{\text{cavity}}))\right|}, \\
&= \frac{2\pi}{\left|(\mathcal{L}_i+\mathcal{L}_{\text{cavity}})\right|}, \\
&= \frac{2\pi}{|\mathcal{L}|},
\end{aligned} \tag{2.46}$$

where $\mathcal{L} = \mathcal{L}_i + \mathcal{L}_{\text{cavity}}$ represents the total loss due to all optical elements in the enhancement cavity. In order to measure the Finesse ($\mathscr{F}_{\text{ec}}$) of the enhancement cavity, an easy approach is to rapidly sweep a cavity mirror away from the resonance (the sweeping would have to be performed much faster than the life time of the cavity). In this case, the intensity of the electric field in the cavity decays exponentially over time and the decay constant can be used to calculate $\mathscr{F}_{\text{ec}}$. Let us assume that an energy of $\mathscr{E}(t)$ is stored in the enhancement cavity when a particular mode is in resonance and then the cavity is swept away from resonance. The energy loss during a round trip would be $\mathcal{L}\mathscr{E}(t)$. Thus, the energy loss per unit time would be $\mathcal{L}\mathscr{E}(t)c/L$. Therefore, the expression of energy in the enhancement cavity as a function time can be written as:

$$\begin{aligned}
\frac{\partial \mathscr{E}(t)}{\partial t} &= -\frac{1}{\tau}\mathscr{E}(t), \\
&= -\mathcal{L}\frac{c}{L}\mathscr{E}(t), \\
&= -\frac{2\pi}{\mathscr{F}_{\text{ec}}}\frac{c}{L}\mathscr{E}(t), \\
&= -\frac{\delta\omega_{\text{ec-fsr}}}{\mathscr{F}_{\text{ec}}}\mathscr{E}(t),
\end{aligned} \tag{2.47}$$

where τ is time constant of decay. The expression for τ in terms of loss of intensity per round trip $\mathcal{L}$ and $\omega_{\text{ec-fsr}}$ can be written as:

$$\tau = \frac{2\pi}{\mathcal{L}\omega_{\text{ec-fsr}}}. \tag{2.48}$$

Hence, the finesse of the enhancement cavity $\mathscr{F}_{\text{ec}}$ can be written as:

$$\mathscr{F}_{\text{ec}} = \frac{2\pi\tau c}{L}. \tag{2.49}$$

In contrast to a Fabry Pérot cavity, the enhancement cavity allows the confinement of the electric field in the transverse dimensions. This leads to transverse modes. In this dissertation, the enhancement cavity is based on spherical and planer optics. Therefore, under paraxial approximation, the transverse modes supported by the enhancement cavity are the Hermite-Gaussian modes, which can be written as[85]:

$$\widetilde{E}_{m,n}(x,y,z,\omega) = \widetilde{E}(\omega)U_l(x,z,\omega)U_m(x,z,\omega)e^{-ikz}, \tag{2.50}$$

where $U_m(x,z,\omega)$ is given by:

$$U_m(x,z,\omega) = \left(\frac{\sqrt{2/\pi}}{2^m m! w_0}\right)^{1/2}\left(\frac{q(0)}{q(z)}\right)^{1/2}\left(-\frac{q^*(z)}{q(z)}\right)^{m/2} H_m\left(\frac{\sqrt{2}x}{w(z)}\right)e^{-\frac{kx^2}{2q(z)}}, \tag{2.51}$$

where $q(z)$ is the q parameter of the beam within the cavity, $w(z)$ is the beam waist, H_m is the Hermite polynomial of order m, and l, m are integers. The parameters $q(z)$ and $w(z)$ can be obtained by solving equation (2.32). We note that the ray matrix is different in the two orthogonal axes of the transverse plane of the cavity shown in Figure 2.5. This is due the different angles of incidence in the two orthogonal axes, x, y, in the transverse plane. Therefore, the waist, the radii and the Gouy phase of the beam differ along the orthogonal axes of the transverse plane. Furthermore, the constants A and D would have to satisfy the constraint $|A+D| \leq 2$. Therefore, by using this condition, we can find the range of values for the separation of focusing mirrors for which we can observe a stable operation point. This range of values for the separation of focusing mirrors is known as the stability range of the cavity.

In order to understand the change in beam waist in an enhancement cavity, let us consider an enhancement cavity at 1030 nm center wavelength (as developed within the framework of this dissertation and discussed in section 4.4), and consisting of a planar input coupler mirror, 5 plane mirrors and 2 focusing mirrors with radii of curvature 150 mm and 200 mm. Let us consider that the input laser coupled into the enhancement cavity has a repetition rate of 65.3 MHz, which corresponds to an enhancement cavity length of 4.591 meters. Let use choose the incidence angle on the focusing mirrors to be 3 degrees. It is necessary to choose a small incidence angle at each of the focusing mirrors as astigmatism and other aberrations will arise at larger incidence angles leading to a larger effective beam waist at the focus. Figure 2.6 shows the waist and radii of the laser beam for this enhancement cavity, that is calculated using the ray matrix formalism.

Based on the Figure 2.6, we note that it is beneficial to choose a stability point closer to the edge of the stability range of the enhancement cavity, as this allows us to achieve a higher peak intensity, which is necessary for HHG. However, we should also note that, in this region, it also much more difficult to mode-match the laser beam to the cavity due to different beam waists along the two orthogonal axes, x, y, of the transverse plane. During our experiment in section 4.4, we choose the separation of the focusing mirrors close to the stability edge.

Using the ray matrix formalism and equation (2.50), the phase accumulated within one round trip through the cavity for a Hermite-Gaussian mode $\widetilde{E}_{m,n}(x,y,z,\omega)$ can be expressed as[35]:

$$\begin{aligned}\varphi_{m,n} = &-kL + (m+\frac{1}{2})\mathrm{sgn}(B_{\mathrm{tangential}})\cos^{-1}\left(\frac{A_{\mathrm{tangential}}+D_{\mathrm{tangential}}}{2}\right)\\ &+ (n+\frac{1}{2})\mathrm{sgn}(B_{\mathrm{sagittal}})\cos^{-1}\left(\frac{A_{\mathrm{sagittal}}+D_{\mathrm{sagittal}}}{2}\right),\end{aligned} \tag{2.52}$$

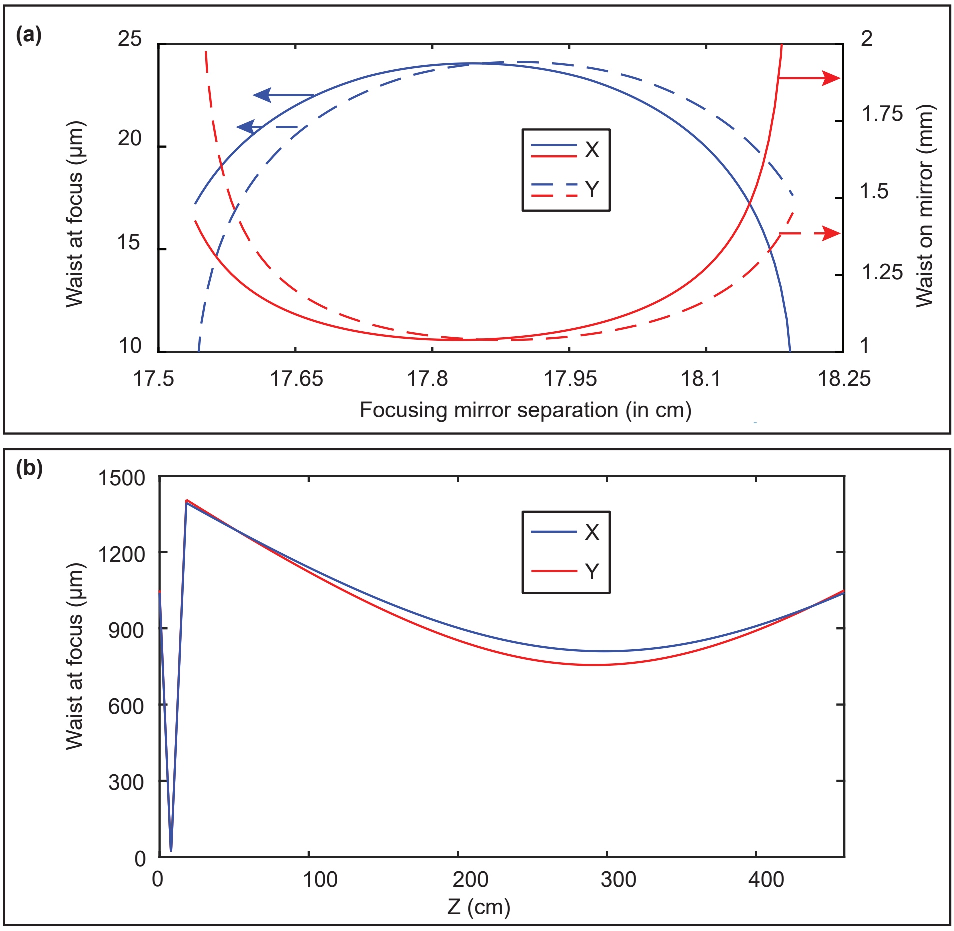

Figure 2.6: (a) The beam waist at the focus and at the 150 mm curved mirror in the enhancement cavity as a function of separation between the focusing mirrors. (b) The beam waist in the enhancement cavity as a function of position in the cavity, with a fixed separation of 17.6 cm between the focusing mirrors. The starting point of reference is the 150 mm focusing mirror.

where $A_{\text{tangential(/sagittal)}}$, $B_{\text{tangential(/sagittal)}}$ and $D_{\text{tangential(/sagittal)}}$ are the ray matrix coefficients for the tangential (/sagittal) axis of the cavity. From equation (2.52), we find that the phase shift for Hermite-Gaussian modes of different orders is different, reflecting the impact of different Gouy phase shifts on different modes. Consequently, the cavity resonance conditions depend on the mode order, i.e. different modes are resonant with different cavity lengths. Therefore, the length of the cavity acts as a mode filter, allowing only certain modes to be coupled into the cavity.

It should be noted that additional spatial phase shifts can occur when the cavity is operated with an ultrashort pulse of high intensity. For example, the intracavity plasma or thermal deformation of the mirror can contribute to additional phase shifts.

2.3.3 Multi-pass cells

An MPC is an optical cavity that is able to confine transverse eigenmodes of EM radiation for a select number of round trips. The first seminal papers on MPC patterns were written by D. Herriott, H. Kogelnik, R. Kompfner, and Harry J. Schulte[86,87]. In the following decades, MPCs have become a standard tool for increasing the length of the interaction path between laser and samples in absorption spectroscopy[88,89]. In recent years, the interest in MPCs has gained immense momentum in the field of spectral broadening[90,91,92]. In this dissertation, we use MPCs for post-compression discussed in sections 3.1, 3.2, and for serrodyne-frequency-shifting discussed in section 4.3.

The design of the MPCs used in this dissertation is based on the commonly used Herriot configuration with two focusing mirrors. In addition, noble gases or fused silica plates are also used to provide the nonlinearity required for spectral broadening and frequency-shifting. The laser beam is mode-matched to an eigenmode of the MPC with a telescope. The beam is then coupled to the MPC via a rectangular pick-off mirror. After the target number of round trips, the laser beam is out-coupled with the same pick-off optic. However, in MPC-2 of section 3.1.2, a small mirror is installed to out-couple the beam after a selected number of round trips in order to limit the losses for the propagating broad-band pulse. This is discussed in detail in section 3.1.2

Since all experiments in this dissertation relate to a laser beam with Gaussian spatial beam profile, we limit our discussion to the calculation of Gaussian eigenmode of an MPC. For simplicity, we also assume that the refractive index of the medium between the two focusing mirrors is uniform. This means that the eignmode calculated in this section only applies to a gas-filled MPC. In this section we do not derive the eignmode of an MPC with a bulk-based medium, as it is tedious to derive analytically. The derivation in this section follows A.-L. Viotti et al.[71] closely. The ray matrix for the MPC, which supports N round trips, can be written as:

$$M = \left[\begin{bmatrix}1 & L/2\\ 0 & 1\end{bmatrix}\begin{bmatrix}1 & 0\\ -1/R & 1\end{bmatrix}\begin{bmatrix}1 & L/2\\ 0 & 1\end{bmatrix}\right]^{2N}, \tag{2.53}$$

where L is the distance between two MPC mirrors, and R is the radii of curvature of the mirrors. By writing $C = L/R$, the ray transfer matrix can be rewritten as:

$$M = \begin{bmatrix}1-C & RC(1-C/2)\\ -2/R & 1-C\end{bmatrix}^{N}. \tag{2.54}$$

For a pulse mode-matched to the eigenmode of an MPC, the q parameter should remain the same after each round trip. We can thus simplify the ray matrix in equation (2.54) with $N = 1$. Therefore, the q parameter can be written as:

$$\begin{bmatrix}q\\ 1\end{bmatrix} = \begin{bmatrix}1-C & RC(1-C/2)\\ -2/R & 1-C\end{bmatrix}\begin{bmatrix}q\\ 1\end{bmatrix}. \tag{2.55}$$

By solving equation (2.55), we find that $q = -\frac{R}{2}\sqrt{C(C-2)}$. From the q parameter, the beam waist and intensity of the laser beam in the MPC can be written as[71]:

$$\begin{aligned} w(z) &= w_0\left(1 + \frac{z^2}{(\frac{R}{2}\sqrt{C(2-C)})^2}\right)^{\frac{1}{2}}, \\ I(z) &= \frac{2P}{\pi w^2(z)} = \frac{4P}{R\lambda\sqrt{C(2-C)} + \frac{4\lambda z^2\sqrt{C(2-C)}}{RC(2-C)}}, \end{aligned} \tag{2.56}$$

where $z = 0$ denotes the center of the MPC, and P is the peak power of the ultrashort laser pulse. An in-depth description of an MPC based on Herriot configurations can be found in Ref.[71].

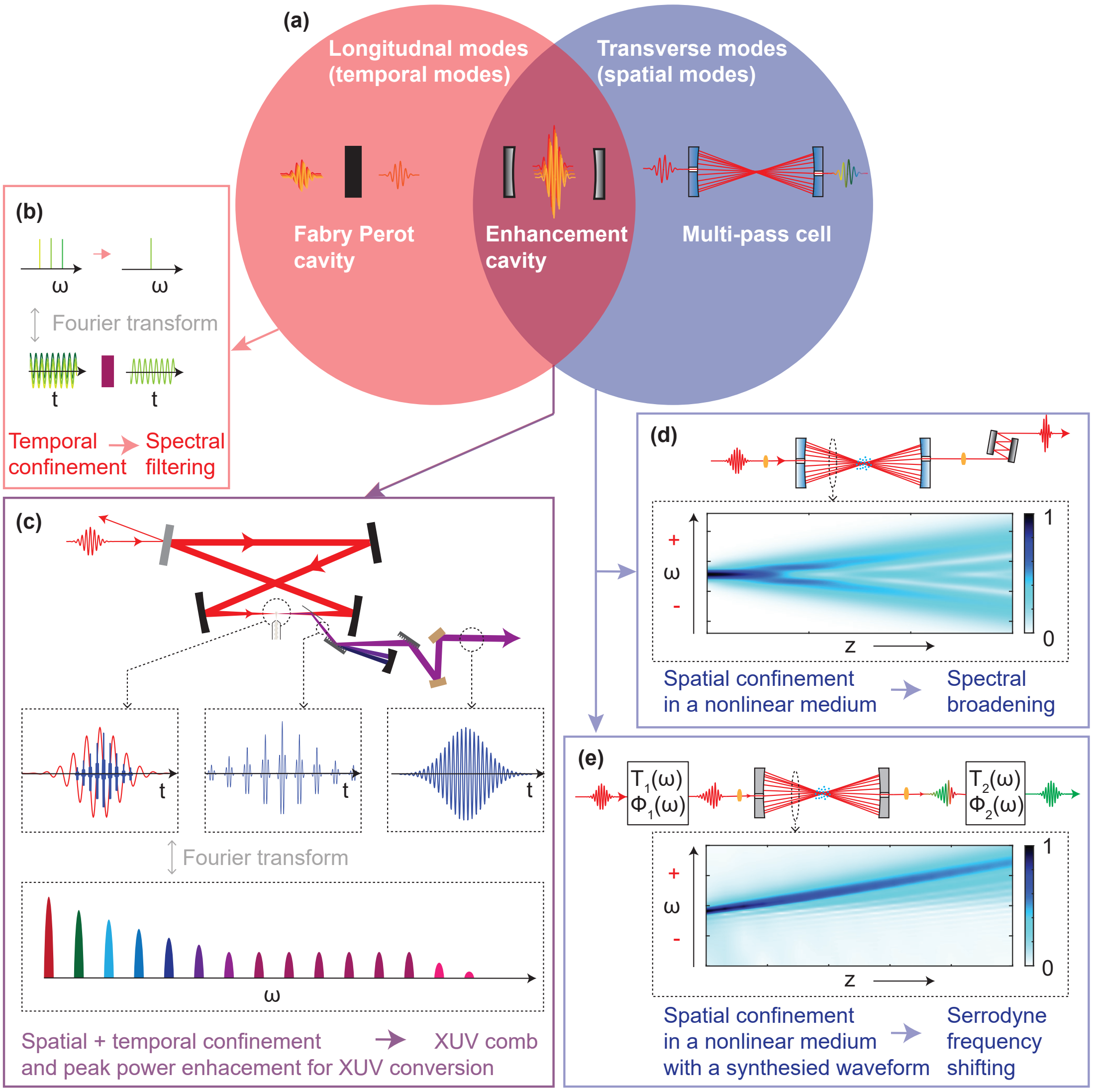

Figure 2.7: (a) An illustration showing a Venn diagram of optical cavities with longitudinal and transverse optical modes. This figure also shows a few applications of (b) a Fabry Pérot cavity, (c) an Enhancement cavity, (d) and (e) an MPC enabled by the temporal / spatial confinement of optical fields.

Unlike a Fabry Pérot cavity and an enhancement cavity, an MPC does not provide spectral filtering or enhancement of the spectral components within the cavity. This is because an MPC does not support longitudinal modes. However, the existence of spatial modes provides a quasi-guiding property for pulses passing the MPC. This property is useful to prevent the Kerr-induced beam collapse and at the same time useful to accumulate large B-integrals. Hence, MPCs are ideal for post-compression. Section 2.4 discusses the nonlinear properties of an MPCs, which are useful for spectral broadening. Another advantage of the MPCs is that they enable flexible dispersion control. Dispersion management is possible by using selective dispersion coatings for dielectric mirrors and by inserting dispersive optical elements into the MPC. In this dissertation, we use the advantage of dispersion management to perform serrodyne-frequency-shifting, as discussed in section 4.3. An overview of the various features of the Fabry Perot cavity, Enhancement cavity and MPC are shown in Figure 2.7.

2.4 Nonlinear multi-pass cells

Similar to most pulse post-compression schemes available today, spectral broadening in an MPC is performed using SPM in a bulk material (the commonly used material is fused silica) or in a gas medium. Followed by spectral broadening, the spectral phase is removed using DCMs to obtain the high intensity ultrashort pulse close to its FL, as depicted in Figure 2.3.

The two important aspects that we need to take into account when designing an MPC for nonlinear applications are the nonlinear phase accumulated in MPC and the intensity of the pulse on the optics. The nonlinear phase accumulated in an MPC is limited by the critical self-focusing of the pulse, which could lead to filamentation. The B-integral quantifies the nonlinear phase that accumulates in an MPC. On the otherhand, the intensity of pulse on the optics is typically limited by the laser-induced damage threshold (LIDT) of the MPC mirrors (quantified usually by the fluence). In this section, we discuss the limits on B-integral and fluence that we consider when designing an MPC. Both parameters depend on the MPC configuration. In this dissertation, we restrict ourselves to Herriot-type MPCs based on two concave mirrors facing each other. The derivations presented in this section follow closely Ref.[71].

2.4.1 Limitations on fluence

From the ray matrix in equation (2.55), we find that in an MPC, the mirror distance L must satisfy $0 \leq L \leq 2R$ in order to fulfill the stability condition of an optical cavity. In an MPC-based on Herriot type configuration, several periodic patterns are possible within this range of values for L. If the laser beam enters and exits the MPC at the same position after N round trips, the angle advance per round trip ξ can be written as:

$$\xi = 2\pi k/N, \quad \text{where } k = 1, 2, ..., N-1. \tag{2.57}$$

The integer k can be used to identify the distance between mirrors L for a given R and N as:

$$\frac{L}{R} = 1 - \cos(\pi k/N) \tag{2.58}$$

By using equation (2.56), the expressions for beam waist (w_m) and fluence (F_m) on the concave mirror can be written as[73]:

$$w_m = \frac{R\lambda}{2\pi}\sqrt{\frac{C}{2-C}} = \frac{R\lambda}{2\pi}\tan\left(\pi k/2N\right) \tag{2.59}$$

$$F_m = \frac{2E}{\pi w_m^2} = \frac{2E}{R\lambda}\sqrt{\frac{2-C}{C}} = \frac{2E}{R\lambda}\frac{1}{\tan \pi k/2N} \tag{2.60}$$

Where E is pulse energy and λ is the center wavelength of the pulse. For an MPC with mirrors of a given radii R and number of round trips N, the lowest fluence occurs for the case of $k = N - 1$. For large values of N, we find that $k/N \approx 1$. In this case, the beam waist and the fluence on the mirror are given by the following expressions:

$$\begin{aligned} w_m &= 2R\lambda N/(\pi^2) \\ F_m &= \pi E/R\lambda N \end{aligned} \tag{2.61}$$

In addition, for bulk based MPC, we have to consider the fluence on the AR coating of the bulk material, which is typically placed at the focus position in the center of the MPC. While the fluence at the focus is typically higher than at the dielectric mirror, we have to note that bulk-based MPCs are used only in the context of laser systems with low pulse energy. For the high average power frequency comb laser system used in this dissertation, the pulse energy is $\approx$ 1.2 μJ. Hence, the fluence on the AR coating is ≤ 10 mJ/cm^2, which is much below the fluence specified by the manufacturer.

We note that as the length of MPC L gets closer to the stability edge ($2R$), we can accommodate more round trips, and the beam waist at focus of MPC becomes smaller. This would increase the B-integral per round trip. The B-integral can be reduced by adjusting the nonlinear medium in the MPC (by reducing the gas pressure in MPC).

2.4.2 Limitations on B-integral

The nonlinearity that the pulse experiences in an MPC can be quantified by the B-integral. There are several ways to define a B-integral for a pulse propagating through a nonlinear medium. In this dissertation, we define the B-integral as the on-axis nonlinear phase accumulated by the pulse. This can be written as:

$$\mathrm{B}_{\text{integral}} = \Sigma_0^N \frac{2\pi}{\lambda} \int n_2(z) I_{\text{peak}}(z) dz, \tag{2.62}$$

where n_2 is the nonlinear refractive index of the medium, I_{peak} is peak intensity of pulse, and N is the number of round trips. In this discussion, the effects of dispersion and losses in the MPC are ignored while calculating the B-integral, as most experiments in this dissertation use low loss dielectric coating, and the pulse duration remains nearly constant during propagation in an MPC. For a MPC filled uniformly with a gas, the expression for the B-integral per round trip can be written as:

$$\begin{aligned} \mathrm{B}_{\text{round-trip}} &= 2\frac{2\pi}{\lambda} \int_{-L/2}^{L/2} n_2(z) I_{\text{peak}}(z) dz \\ &= 8\pi^2 \frac{n2P}{\lambda^2 z_R} \int_0^{L/2} (1 + (\frac{z}{z_R})^2)^{-1} dz \\ &= 8\pi^2 \frac{n_2 P}{\lambda^2} \frac{k}{N} \end{aligned} \tag{2.63}$$

Where P is the peak power of the pulse. In order to avoid filamentation, it is important to maintain the peak power below the critical power $P_{\text{critical}} \approx \lambda^2/(2\pi n_0 n_2)$ to prevent self focusing of the beam[56]. By substituting the peak power of pulse with the critical power, we can compute the maximum B-integral which can be obtained per round trip[71]:

$$\mathrm{B}_{\text{round-trip}} \leq 2\frac{2\pi k}{N} \quad \approx 4\pi \tag{2.64}$$

In the literature, the reported B-integral for MPCs which use bulk material as nonlinear medium is much lower ($B_{\text{round-trip}} < 2\pi/5$) than for gas based MPCs[93,94]. However, M. Seidel et al.[95] have shown that an MPC with multiple Kerr plates could support $B_{\text{round-trip}} \approx 1.6\pi$.

CHAPTER 3

POST-COMPRESSION OF HIGH POWER LASERS USING MULTI-PASS CELLS

In this chapter, we will focus on the post-compression of ultrashort lasers with high peak power and high average power. In the context of this dissertation, these works were carried out to gain familiarity with a key method for this dissertation: optical multi-pass cells. At the same time, this work enabled addressing a challenging topic: few-cycle pulse generation. This chapter is organized as follows: First, in section 3.1, we address the challenge of post-compressing a picosecond laser to few optical cycles, as discussed in section 1.5. Afterwards, in section 3.2, we discuss the post-compression of a high average power ultrashort laser, which involves the development of MPC based post-compression for a pulse with μJ-class pulse energy. The high average power ultrashort laser, which is post-compressed here in section 3.2, is the same laser used for the development of the VUV frequency comb discussed in chapter 4.

3.1 Post-compression of picosecond pulse to few cycles

High power few cycles ultrashort lasers find applications in attosecond physics[96], light-wave electronics[97] and particle acceleration[98]. Both pulse energy and average power are important factors for such lasers. This is because high pulse energies are needed to reach Gigawatt to Terrawatt peak powers required to drive nonlinear phenomena, such as multiphoton ionization, HHG, wakefield acceleration, etc,. On the other hand, high repetition rates are attractive for measuring coincidence events in experiments, such as ionization events in reaction microscopes[99,100], photoelectron angular distribution of dissociating molecules[101], and they can be generally beneficial for experiments carried out using pump-probe schemes[102]. In a typical pump-probe experiment, the measurement must be repeated several times- especially for events with a low probability - to achieve a high signal to noise ratio. In addition, it is important to repeat the same experiment with different delays between pump and probe pulses. Furthermore, high repetition rates are required for the generation of frequency combs. In the beginning of this section, we present a brief review of the methods available to generate few cycle pulses with a high pulse energy and a high average power. Our discussion closely follows the reviews of post-compression techniques discussed by A.L.Viotti et al.[71], and T Nagy et al.[103]. Afterwards, we discuss the motivation to use an MPC as a key element in this dissertation and present the works carried out to generate few-cycle laser pulses.

The first pulse compression that has achieved high peak power was reported by C. Rolland and P. B. Corkum. In this work, pulses were compressed by free space propagation in a bulk medium to sub-20 fs with a pulse energy of few tens of μJ [104,105]. In recent years, this method has been improved to generate an ultrashort pulse with a pulse duration of 13 fs and a pulse energy of 3.25 J [106]. However, the beam quality was poor, and the pulse duration from pulse to pulse varies strongly between 6.4 and 29 fs. It should be noted that simulation works have been reported showing that this method, together with the thin film compression technique, can enable post-compression of Joule-class lasers with a Petawatt peak power [107].

A. H. Kung proposed an alternative idea for post-compression by using multiple Kerr plates to broaden the spectrum. In this method, the nonlinearity of a series of thin plates, together with periodic foci, is used to acquire a large B-integral [108,109]. Although this method can generate broadband few cycle pulses, it has shortcomings in energy scalability. In addition, spatial inhomogeneties were observed in the post-compressed pulse [110].

Another method that has been investigated to generate few cycle pulses is filamentation. Filamentation is a self-guided propagation in a medium due to the interaction between dispersion, diffraction, self phase modulation and ionization [111]. With a Ti:Sapphire laser, C. P. Hauri et al. have post-compressed a pulse to 5.7 fs with a pulse energy of 0.38 mJ [112]. This method is better suited for pulses at longer wavelengths. With filamentation, pulses with a pulse energy of 2.1 mJ were post-compressed to 11.8 fs at a center wavelength of 1.8 μm [113]. In addition, at 3.9 μm, a pulse with 100 fs FWHM and a pulse energy of 15 mJ were post-compressed to 31.5 fs with a pulse energy of 13 mJ. This corresponds to a peak power of 0.3 TW [114]. While filamentation has provided a simple way to generate few cycle pulses, the pulses obtained show significant variations in the temporal pulse profile along different positions along the transverse plane [115].

A very important and in-depth explored method for post-compression is based on optical fibers used as guiding medium. In 1996, the post-compression of pulses with high peak power in a gas-filled capillary fiber, also known as hollow core fibers (HCF), was first reported [116]. In a HCF, a pulse is propagated at grazing incidence reflection. Although an HCF can support multiple eigenmodes due to its large core area, it is possible to couple the ultrashort pulse into a selected eigenmode of the HCF. In addition, it has been demonstrated experimentally that the pulse can be confined to the selected eigenmode without mode mixing [117]. However, HCFs are relatively lossy at lengths > 1 m. A. L. Cavalieri et al. post-compressed a $\sim$1 mJ pulse of 23 fs to 0.5 mJ, 3.8 fs [118]. The introduction of stretched flexible hollow core fibers (SF-HCF), which have thinner walls than HCF, has reduced losses at lengths > 1 m [119]. In addition, several schemes have been investigated to improve post-compression performance in HCFs by employing advanced schemes employing pressure gradients [120,121,122,123], or a molecular gas [124,125]. Recently, in a SF-HCF of 8.2 m length, a 50 fs ultrashort pulse with 14 mJ pulse energy was post-compressed to 3.8 fs with an output pulse energy of 6.1 mJ. This ultrashort pulse has a peak power of 1.2 TW [126], thus approaching a parameter regime suitable for laser wakefield acceleration. It should be noted that while HCF, SF-HCF and other variants based on HCF technology offer a way to produce high-power, few-cycle ultrashort pulses, there are still several problems with this approach. The experimental setup required for HCF drastically scales to large dimensions for multi-mJ ultrashort pulses that require high compression rations. Below, we line out important energy scaling limits for MPCs and HCFs. The derivations presented here follow A.L.Viotti et al. [71] closely.

3.1.1 Scaling limits of setup for HCF and MPC

For HCFs and variants of HCF, the main factors determining the length of the setup for post-compression are the damage threshold of the employed optics and ionization or damage threshold of the non-linear medium. The laser induced damage threshold (LIDT) is the limit at which a medium or optic is damaged by a laser. We can derive the length of HCF and MPC required for a given ultrafast pulse by calculating the fluence and B-integral required for post-compression. Since the objective is to generate high-power few cycle ultrashort pulses, we will limit this discussion to gas filled MPCs.
The overall length of a HCF setup can be written as:

$$L_{\text{HCF}} = L_{\text{free}} + L_{\text{fiber}} + L_{\text{free}} \tag{3.1}$$

Where L_{free} is the distance from the last free space optic to the HCF and L_{fiber} is the length of the HCF used for post-compression. If we consider a beam waist w_0 at the input of the HCF, the spot area on the focusing optic A_f can be written as:

$$A_f = \pi w_f^2 = \pi \left(\frac{L_{\text{free}}\lambda}{\pi w_0}\right)^2 \tag{3.2}$$

$$= \frac{L_{\text{free}}^2 \lambda^2}{A_0}, \tag{3.3}$$

where w_f is the beam waist at the focusing optic and A_0 is the area of the focal spot at the HCF. The intensity on the focusing mirror I_{ft} can thus be written as:

$$I_{ft} = \frac{2P}{A_f} = \frac{2A_0 P}{L_{\text{free}}^2 \lambda^2} = \frac{4P^2}{L_{\text{free}}^2 \lambda^2 I_{0t}}, \tag{3.4}$$

where P is the peak power of the ultrashort laser and I_{0t} is the intensity threshold for the smallest focus on the HCF. We must note that I_{0t} specifies an intensity threshold at which we observe spectral broadening due to ionization of gas in HCF. Hence, L_{free} can be written as:

$$L_{\text{free}} = \frac{2P}{\lambda\sqrt{I_{0t} I_{ft}}}. \tag{3.5}$$

The length of the HCF need for a targeted B-integral can be expressed according to Nagy et al.[127] as:

$$L_{\text{fiber}} = \frac{BP}{I_{0t}\lambda}. \tag{3.6}$$

Hence the total setup length for HCF can be written as:

$$L_{\text{HCF}} = \frac{BP}{I_{0t}\lambda} + \frac{4P}{\lambda\sqrt{I_{0t} I_{ft}}}. \tag{3.7}$$

In an MPC, the pulse energy is limited by the LIDT of the MPC mirrors and the peak intensity in the medium that is used to provide nonlinearity. As reported by A.L.Viotti et al.[71], for an intensity at the mirrors I_{ft}, and an intensity at focus I_{0t}, the total setup length for post-compression using an MPC is given by:

$$L_{\text{MPC}} = \frac{4P}{I_{0t}\lambda}\sqrt{\frac{I_{0t} - I_{ft}}{I_{ft}}} \approx \frac{4P}{\lambda\sqrt{I_{0t}I_{ft}}}. \tag{3.8}$$

In the above equation, the approximation $I_{0t} \geq I_{ft}$ was used. Combining equations (3.7) and (3.8), the ratio of minimum lengths L_{HCF} and L_{MPC} can be written as:

$$\eta = \frac{L_{\text{HCF}}}{L_{\text{MPC}}} \approx 1 + \frac{B}{4}\sqrt{\frac{I_{ft}}{I_{0t}}}, \tag{3.9}$$

Therefore, an MPC provides a convenient solution for the post-compressing of a high-power ultrashort laser with large broadening factors, as a large B-integral can be acquired with a smaller setup length. Furthermore, due to the high reflectivity provided by state-of-the-art mirror coating technology, MPCs typically have higher transmission efficiency than HCFs / SF-HCFs. In addition, unlike an HCF / SF-HCF, the coupling efficiency of an ultrashort pulse into an MPC with an appropriate telescope design for mode matching can be nearly 100 %. Finally, an MPC enables fine dispersion control. This is because at every mirror bounce, a custom dispersion coating can be applied. These advantages make MPCs an attractive and valuable approach for post-compressing high-power ultrashort lasers to few optical cycles.

3.1.2 Experimental setup

The following experiment is based on using two cascaded noble gas-filled MPCs. The schematic of the experimental setup is shown in Figure 3.1. The laser is based on a Yb Innoslab laser amplifier which emits pulses with a pulse duration of 1.2 ps (FWHM) at a center of wavelength 1030 nm . The M^2 parameter, which indicates the beam quality of the laser, is 1.1 $\times$ 1.2. The pulses are released in bursts, with a burst repetition rate of 10 Hz. Within each burst, pulse trains are present at 100 kHz repetition rate[128]. The pulse energy of the pulse is 2 mJ and hence, the in-burst average power of this laser is 200 W.

The pulses are coupled to the first MPC, which consists of two dielectric concave mirrors. The mirrors have 1 m radius of curvature, 100 mm diameter, and provide a group delay dispersion (GDD) $\leq$ 10 fs^2 at wavelengths in the range from 980 nm to 1080 nm as shown in Figure A.1 (b) in Appendix A. During the experiment, the MPC mirrors are exposed to a fluence exceeding 30 mJ/cm^2 at a pulse energy of 2 mJ. The mirrors are placed in a vacuum chamber filled with krypton gas at 0.9 bar. The laser beam is mode-matched to the MPC eigenmode with a mode-matching telescope and then the in- and out-coupling of the pulses is achieved by a 6 mm thick anti-reflection-coated fused silica window followed by a rectangular pick-off mirror placed in front of one of the MPC mirrors. A photograph of a similar MPC configuration showing the pick-off mirror is shown in Appendix B. The same pick-off mirror is also used to couple the beam out after 44 passes through the MPC. After out-coupling, a telescope is used to collimate the beam. DCMs are used to remove the residual phase after the first MPC. They employ dielectric mirror coatings and are designed to provide a near uniform GDD of $\sim$-195 fs^2 in the wavelength range from 980 to 1080 nm. After the first post-compression stage, an attenuator based on a broadband thin film polarizer and half wave plate (HWP) is used to enable control of the pulse energy sent into the second MPC. Optionally, a pick-off mirror can be inserted to send the compressed pulses for temporal characterization.

For further post-compression to few cycles, the compressed pulses from the first post-compression stage are then mode-matched to a second MPC with a telescope built with 2 inch dielectric mirrors (as lenses could cause nonlinear effects that can change the characteristics of the ultrashort pulse). The second MPC consists of two silver mirrors with added dielectric multilayer coatings, with a 1 m radius of curvature and a diameter of 75 mm. The dielectric multi-layer coating provides an enhanced reflectivity. The enhanced silver mirrors provide a GDD $\leq$10 fs^2 in a wavelength range of 700 and 1300 nm, as shown in Figure A.1 (b) in Appendix A. The mirrors of the second MPC are also placed in a vacuum chamber, but filled with krypton gas at a pressure of 1 bar. The pulses enter the second MPC chamber through a 6 mm thick anti-reflection coated window made of UV fused silica, and are coupled out through a 3 mm thick uncoated window made of UV fused silica. To reduce fluence and B-integral in the in-coupling window, the converging input beam is propagated about 2 m through the vacuum chamber, before in-coupling into the MPC. Separate mirrors are used for in-coupling and out-coupling. The beam is out-coupled after 12 passes. After the out-coupling, the beam is collimated, and the pulse energy is attenuated with an uncoated wedge to avoid nonlinear propagation effects in the air. The pulses are then compressed with dispersion-matched DCM pairs designed to compensate the dispersion of fused silica. After post-compression, the temporal duration of the pulses is characterized by using the dispersion-scan (D-scan) technique.

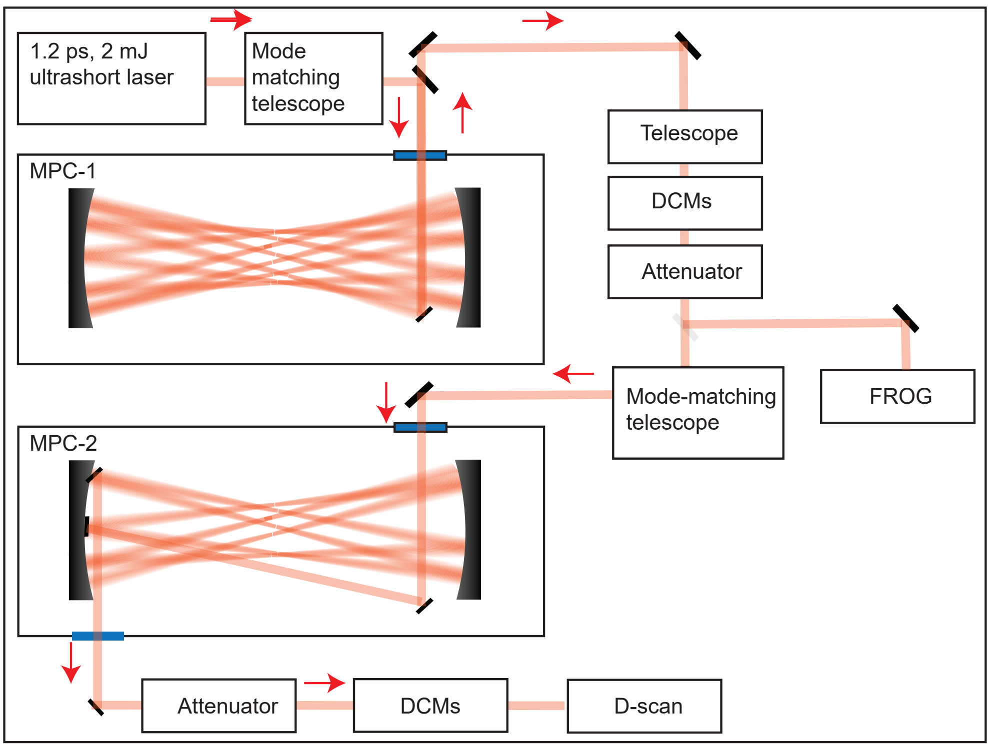

Figure 3.1: Schematic of the experimental setup showing an ultrashort laser coupled to two cascaded gas-filled MPCs used for spectral broadening (length $\leq$ 2 m), followed by DCM compressors used for compression.

3.1.3 Results

Figure 3.2 summarizes the results of spectral broadening and post-compression with the first MPC. The Fourier-limited pulse duration of the spectrally broadened pulse after the first MPC is 30 fs. The DCMs used to remove the phase after the first MPC are optimized to compress the pulse with a total GDD of $\approx$-6200 fs^2 in 32 bounces. The temporal profile of the input Gaussian pulse (shown as grey line) and the corresponding retrieval of the temporal intensity profile of the reconstructed pulse obtained via frequency resolved optical gating (FROG) characterization are shown in the panel on the right side of Figure 3.2 (a). Figure 3.2 (b) shows the measured trace (left side) and the retrieved trace (right side). The FROG characterization shows that the ultrashort pulse is post-compressed to 32 fs, which corresponds to a compression factor of 37.5. The beam profiles of the pulse at the focus and as a collimated beam are shown in Figure 3.2 (c), indicating a good beam quality. The transmission efficiency of the first MPC is 85 %, and the pulse energy after compression from the first MPC is 1.6 mJ, which corresponds to a total transmission efficiency of 80 %.

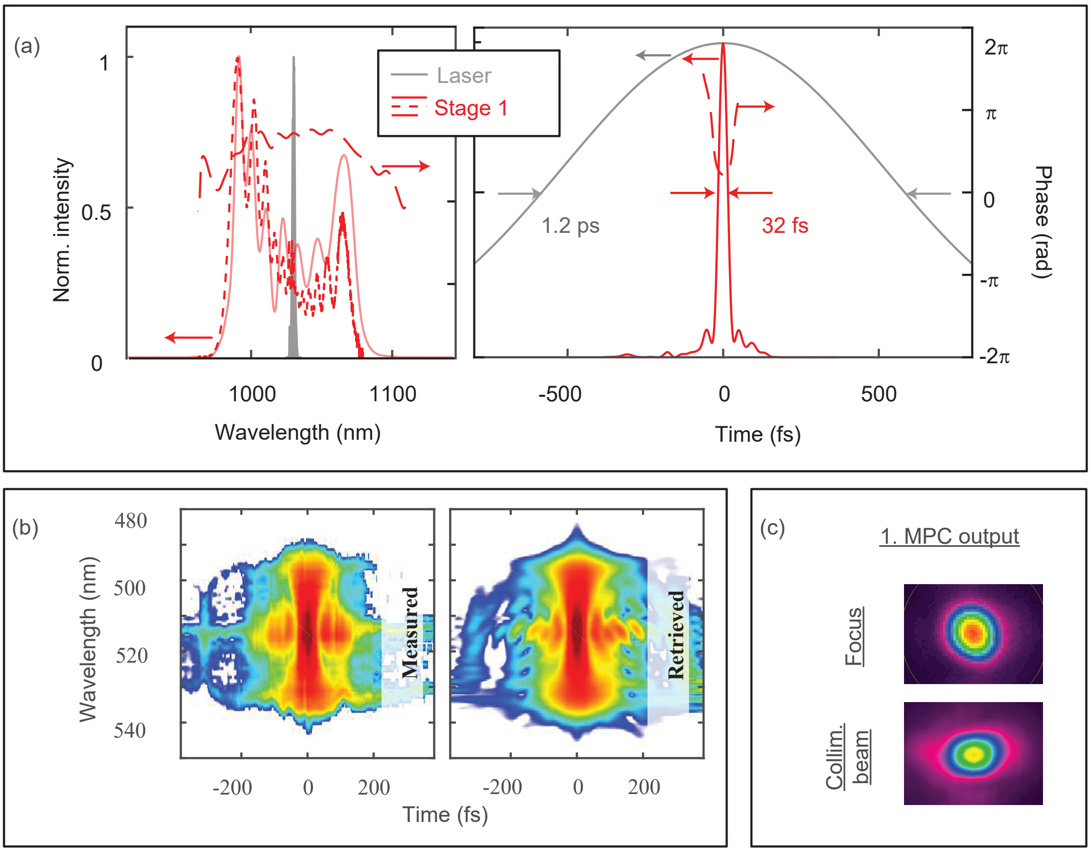

Figure 3.2: a) Reconstructed spectral and temporal intensity and phase profiles together with the corresponding spectra, measured after the first MPC (dotted) and at the laser output (gray line / area). (b) Corresponding FROG traces (logarithmic scale). (c) Beam profiles near the output of the first MPC at the focus and when the beam is collimated. This figure is reprinted from Ref.[129]

When the pulses with a pulse duration of 32 fs (FWHM) are coupled to the second MPC, the enhanced silver mirrors are on the onset of damage when the pulse energy exceeds 0.8 mJ. This corresponds to a fluence of 12 mJ/cm^2 assuming linear mode-matching. We observed mirror damage at higher pulse energies which could likely be attributed to an increased fluence caused by Kerr-lensing inside the MPC. Therefore, during the experiment, we limit the pulse energy at the input of the second MPC to 0.8 mJ. The pulse energy after the second MPC is 0.37 mJ, which corresponds to a transmission efficiency of 46%. The primary reason for the lower transmission efficiency is the limited reflectivity of the enhanced silver mirrors used in the second MPC. After the second MPC, the pulse energy was attenuated and the pulse is compressed using DCMs, which compensate ≈-1900 fs^2 at 1030 nm center wavelength. Figure 3.3 summarizes the results of the post-compression with the second MPC. The temporal intensity profile retrieved from the D-scan, as shown in Figure 3.3 (a), indicates that the pulse is post-compressed to 13 fs.

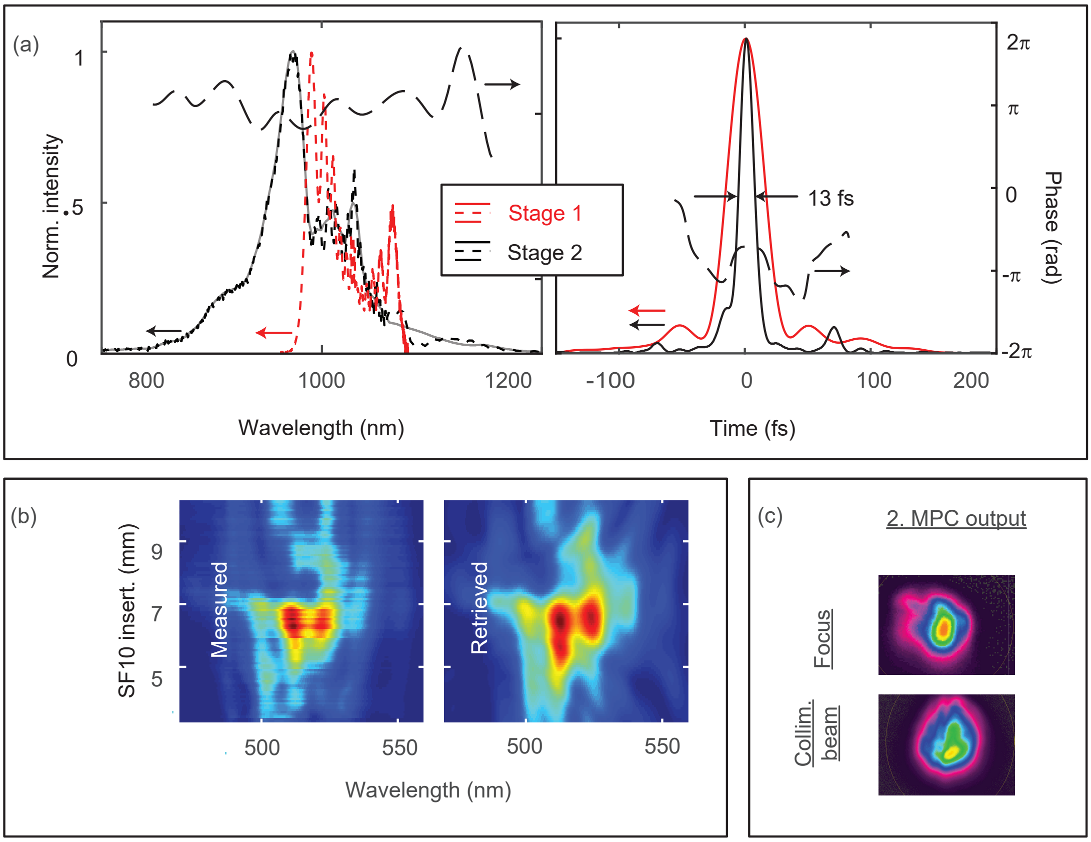

Figure 3.3: (a) Reconstructed spectral and temporal intensity and phase profiles, together with the corresponding spectra measured after the second MPC (black) and after the first MPC (red). (b) Corresponding D-scan traces (logarithmic color scale). (c) Beam profiles near the output of the second MPC at the focus and when the beam is collimated. This figure is reprinted from Ref.[129]

The above results show that the pulse is post-compressed by a factor of 92, corresponding to a compression factor of ≈ 37.5 in the first stage and ≈ 2.5 in the second stage by means of a 2 m long setup. This is a record compression factor for post-compression at high peak power to the best of our knowledge. However, during this experiment we notice some limitations. They are discussed below in section 3.1.4.

3.1.4 Limitations of the post-compression setup

In the here reported experiment, the output was limited to 0.37 mJ, mainly due to a low damage threshold of enhanced silver mirrors in the second MPC. Furthermore, the reflectivity of the enhanced silver mirrors is limited to values between 97.5 and 98.5 %, as shown in Figure A.1 in Appendix A. This causes severe limitations of the throughput of the MPC. Also, as enhanced silver mirrors are used for in-coupling and out-coupling at the second MPC, the overall throughput of the second post-compression stage is further reduced.

Moreover, the Krypton gas used in the second MPC contributes a dispersion of $\approx$ 800 fs^2. Based on the D-scan results obtained during the experiment and the GDD applied for compression using DCMs, we estimate that the pulse was temporally broadened from 32 fs to $\approx$ 200 fs in the second MPC. This large temporal broadening effectively leads to ineffective use of the propagation length in the second MPC for acquiring B-integral.

Finally, the enhanced silver mirrors absorb the non-reflected light, which leads to thermal effects. These thermal effects are likely responsible for a degradation of the beam quality. This effect is clearly observed at the output beam profiles of the second MPC as shown in Figure 3.3 (c).

3.2 Post-compression of a high average power frequency comb laser

Similar post-compression methods as developed in the experiment discussed in section 3.1.2 are then applied to post-compress the frequency comb laser discussed in section 4.2. Again, an MPC is used but this time adapted to a very different parameter range. This laser is post-compressed to increase the peak power and enable efficient generation of XUV. The high average power frequency comb laser used in this experiment emits pulses of 205 fs (FWHM), with a pulse energy of $\approx$ 1.16 μJ at a repetition rate of 65.3 MHz.

In order to post-compress these low energy pulses, we develop a very compact MPC consisting of two concave mirrors with 100 mm radii of curvature, and a diameter of 50 mm. The dielectric coating on these mirrors is designed to ensure that the GDD provided at each reflection compensates the dispersion acquired within 10.5 mm fused material placed inside the MPC for spectral broadening. Five anti-reflection (AR) coated fused silica windows are used with a total thickness matching 10.35 mm: 1 plate placed at the focus has a thickness of 6.35 mm, two windows with a thickness of 1 mm are placed on both sides at about 1 cm distance from the focus, and two UV fused silica windows with a thickness of 1 mm are placed on both sides at about 2 cm distance from the focus. In this configuration, the pulse experiences a near net zero GDD per pass through the MPC. The MPC accommodates 32 round trips. The distance between the MPC mirrors is 187 mm. Figure 3.4(a) shows the schematic for the experimental setup. After spectral broadening in the MPC, the pulses are compressed using DCMs which provide a nearly uniform GDD of $\approx$ -195 fs^2 at wavelengths in the range from 980 nm to 1080 nm.

The MPC throughput is 82 %. For compression, a total GDD of $\approx$ -1170 fs^2 is accumulated in 6 DCM reflections. The post-compressed ultrashort pulse is characterized using FROG. Figure 3.4 summarizes the results of post-compression of the frequency comb laser. The retrieved temporal intensity profile obtained from the FROG characterization, as shown in Figure 3.4 (b), reveals compression to a pulse duration of 36 fs

(FWHM). The pulse energy of the pulse after compression via DCMs is ≈0.83 μJ, which corresponds to a total transmission efficiency of 71 %. The beam profiles at the MPC output, as shown in Figure 3.4 (d), indicate a good beam quality.

In this experiment, we have effectively post-compressed an ultrashort laser with a pulse duration of 205 fs, an average power of 76 W and an average pulse energy of 1.16 μJ to a pulse duration of 36 fs, an average power of 54 W and a pulse energy of 0.83 μJ. We have thereby addressed a challenging parameter regime for MPCs operating at only 1 μJ-level pulse energy.

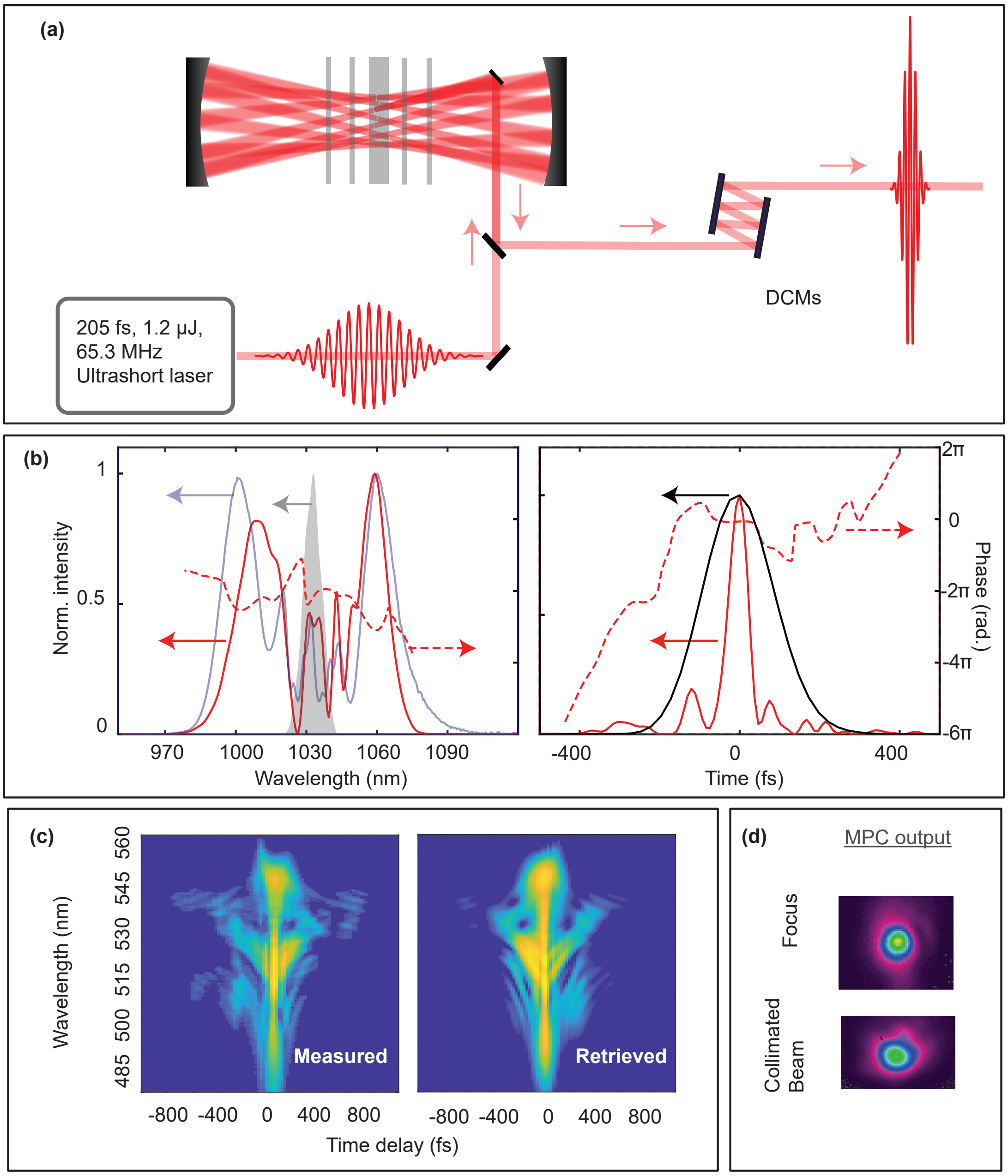

Figure 3.4: (a) Schematic of the experimental setup: a bulk MPC followed by a DCM compressor for spectral broadening and compression. (b) Reconstructed spectral and temporal intensity (red) and phase (dashed red) profiles together with the measured spectra after compression (blue) and the laser output coupled into the MPC (gray area / black line). (c) Corresponding FROG traces (logarithmic scale). (d) Beam profiles near the MPC output when the beam is focused and when the beam is collimated.

CHAPTER 4

TOWARDS THE GENERATION OF A WAVELENGTH TUNABLE VUV FREQUENCY COMB

In this chapter, we address key challenges towards a tunable VUV frequency comb, which can be used to generate VUV radiation for spectroscopy of the ^{229}Th isomer, as discussed in section 1.5 of this dissertation. The low energy nuclear transition of ^{229}Th is of particular interest because it could pave the way for the construction of a high-precision nuclear clock. Due to its conceptual advantages, a nuclear optical clock may surpass even the best atomic clocks of today. This desired improvement in clock stability is due to the fact that the atomic nucleus is smaller in size than the atomic shell, leading to improved immunity against external influences[33,130]. Furthermore, there are other potential applications, such as the study of fundamental physics and quantum electrodynamics[32].

In order to find the low energy nuclear transition of ^{229}Th, it would be ideal to have a tunable laser, whose wavelength can be tuned in the wavelength range from 146.6 nm to 152.8 nm[32]. Furthermore, the natural linewidth of low energy nuclear transition is expected to be in the order of one mHz[33]. In a neutral ^{229}Th, the linewidth increases to a few kHz, which is caused by the so-called internal conversion decay process. The linewidth increase due to internal conversion can be mitigated by probing ^{229}Th^{q+} ions instead[131]. When building a nuclear clock, this is in fact the preferred option as a much higher clock stability can be achieved[132]. Therefore, a narrow linewidth laser is required for excitation of the low energy nuclear transition in ^{229}Th^{q+} ions. Moreover, considering the small cross-section of the nuclear transition[130], a high average power, wavelength-tunable VUV laser is required. We note that measurements reported towards the end of this dissertation indicate that the nuclear transition is in the range of 148.71$\pm$0.47 nm[133]. However, since this information is only available towards the end of this dissertation, the tunable wavelength laser built during this dissertation has targeted the larger wavelength range of 149.7$\pm$3.1 nm[32].

This chapter is organized as follows: First, in section 4.1, we briefly discuss possible approaches for the development of a tunable VUV comb source. Later, in section 4.2, we describe the high average power frequency comb laser, which is used for establishing a new wavelength tuning concept and the development of a passive enhancement cavity for VUV frequency comb generation, discussed in sections 4.3 and 4.4, respectively. Finally, we describe a second promising path to building a record high average power VUV frequency comb laser in section 4.5.

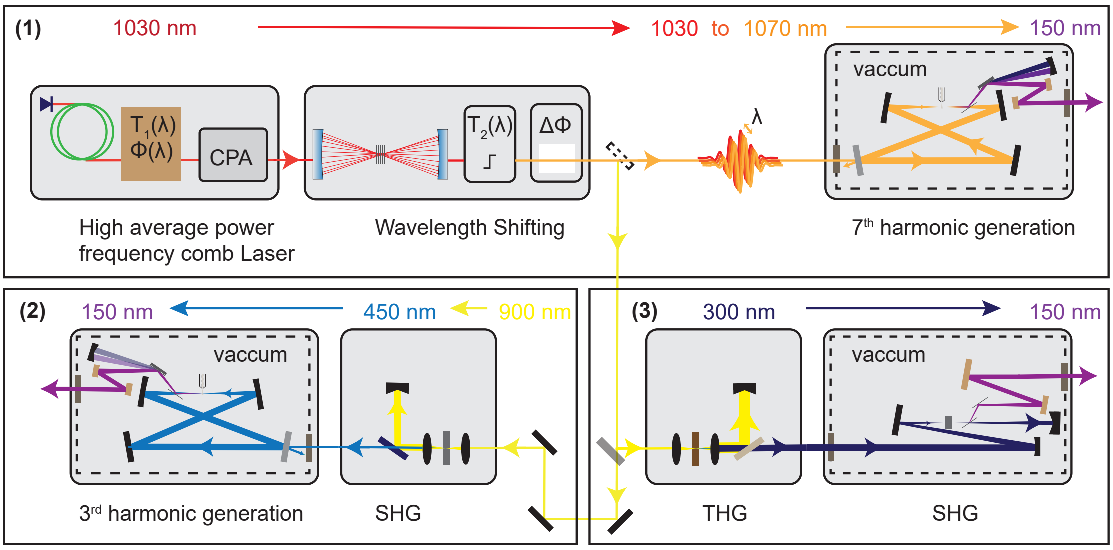

Figure 4.1: Schematic illustrating different approaches for VUV frequency comb generation utilizing: (1) the 7th harmonic of an IR driver laser, generated inside an enhancement cavity, (2) the third harmonic of a tunable short wavelength driver laser at about 450 nm, obtained via SHG of a wavelength-tuned Yb laser, (3) The second harmonic (generated in a KBBF crystal) of a 300 nm laser obtained via THG of a wavelength-shifted Yb laser.

4.1 Approaches to the development of VUV laser sources

There are a few possible ways to develop a frequency comb laser that could enable us to find the low energy nuclear transition of ^{229}Th and ^{229}Th^{q+} ions with a high precision. We here briefly line out three selected routes:

1. VUV comb generation utilizing the 7th harmonic of an IR laser: We can develop a tunable driver laser from 1030 nm to 1070 nm and then convert this laser via 7th harmonic generation into the VUV: The disadvantage of this method is that there is a very low conversion efficiency of the IR laser to the 7th harmonic[65]. However, the experimental setup is significantly simpler than the alternative options described below.

2. VUV comb generation utilizing the third harmonic of a tunable short wavelength laser at about 450 nm: We can prospectively develop a frequency comb laser at a wavelength of about 900 nm and convert this laser via second harmonic generation to 450 nm in a crystal, followed by third harmonic generation in a gas to reach wavelengths around 150 nm. Since the second and third harmonic generation have a high efficiency, this method is promising to generate a high average power VUV laser. A key challenge with this approach is the development of a high-power comb at 900 nm wavelength. A possible route could be extreme wavelength tuning of an Ytterbium laser as discussed in section 6.1.2.

3. A third practical approach is second harmonic generation in a KBBF crystal of an extremely wavelength-tuned and frequency tripled Yb laser. While harmonic conversion to reach 150 nm has been demonstrated using KBBF crystals, these crystals are difficult to handle and the demonstrated efficiency is low[134,135,136,137].

In this dissertation, we focus on approach 1 and line out first steps towards testing approach 2 in order to develop a VUV source for spectroscopy of the low energy nuclear transition of ^{229}Th. An illustration of the three approaches is shown in Figure 4.1.

4.2 Driving Laser

This section describes the high-power frequency comb laser used for development of the wavelength-tuning method and the VUV conversion system. A schematic of the high-power frequency comb driving laser is shown in Figure 4.2 (a). The laser consists of an Yb oscillator based on a nonlinear amplifying loop mirror (NALM)[138]. It delivers ultrashort pulses with a pulse duration of 150 fs and a repetition rate of 65.3 MHz. A 165 m polarization maintaining fiber stretches the ultrashort pulses to 120 ps. Subsequently, the pulses are amplified in a fiber amplifier from 2.6 mW to 300 mW. The stretched pulses are sent through a pulse shaper consisting of a programmable spatial light modulator (Waveshaper 1000A/SP by Finisar). The pulse shaper has an insertion loss of $\approx$ 5 dB and therefore the power level at the output of the pulse shaper is 82 mW. The pulses are then amplified to an average power of 5 W in a double-clad Yb-doped fiber. Later, the pulses are amplified to about a 100 W with an amplifier built using a rod-type fiber commercially available from NKT Photonics. Finally, the pulses are compressed using a grating compressor. The pulses are compressed to 205 fs and the laser has an average output power of 76 W. A detailed description of the laser can be found in a recent paper by S.Salman et al[139]. The retrieval of the compressed output pulses using FROG is shown in Figure 4.2 (b). The beam profiles of the laser at the focus and when collimated are shown in Figure 4.2 (c).

4.3 Serrodyne-frequency-shifting of the high-power driving laser

In this section, we discuss a new method for tuning the wavelength of a high-power frequency comb laser using serrodyne-frequency-shifting, introduced in section 2.2.3.

In this dissertation, we need to shift the frequency of the 76 Watt frequency comb laser by $\approx$ 12 THz in order to cover the uncertainty range of the low energy nuclear transition of ^{229}Th[32], considering frequency conversion via 7th harmonic generation. The method used in this dissertation for the serrodyne-frequency-shift of the high-power laser can be described in three basic steps:

1. An incoming laser pulse, which may or may not have a chirp, can be shaped in both phase and amplitude by using a pulse shaper. This pulse shaper can be based on a programmable spatial light modulator (at low power, prior to amplification) or on a high-power compatible shaper (typically with fixed parameters) such as a set of dispersive mirrors.

2. In the second step, the laser pulse is amplified via chirped pulse amplification and then compressed. Pulse shaping in step 1 needs to be done in such a way that a temporal pulse shape approaching a saw-tooth emerges after compression.

3. In the third and final step, the pulse is sent into a dispersion-engineered MPC, in which self-phase modulation leads to a linear phase change in time, equivalent to a frequency shift. Finally, with a spectral filter, the spectrally shifted pulse is separated from the undesirable spectrum.

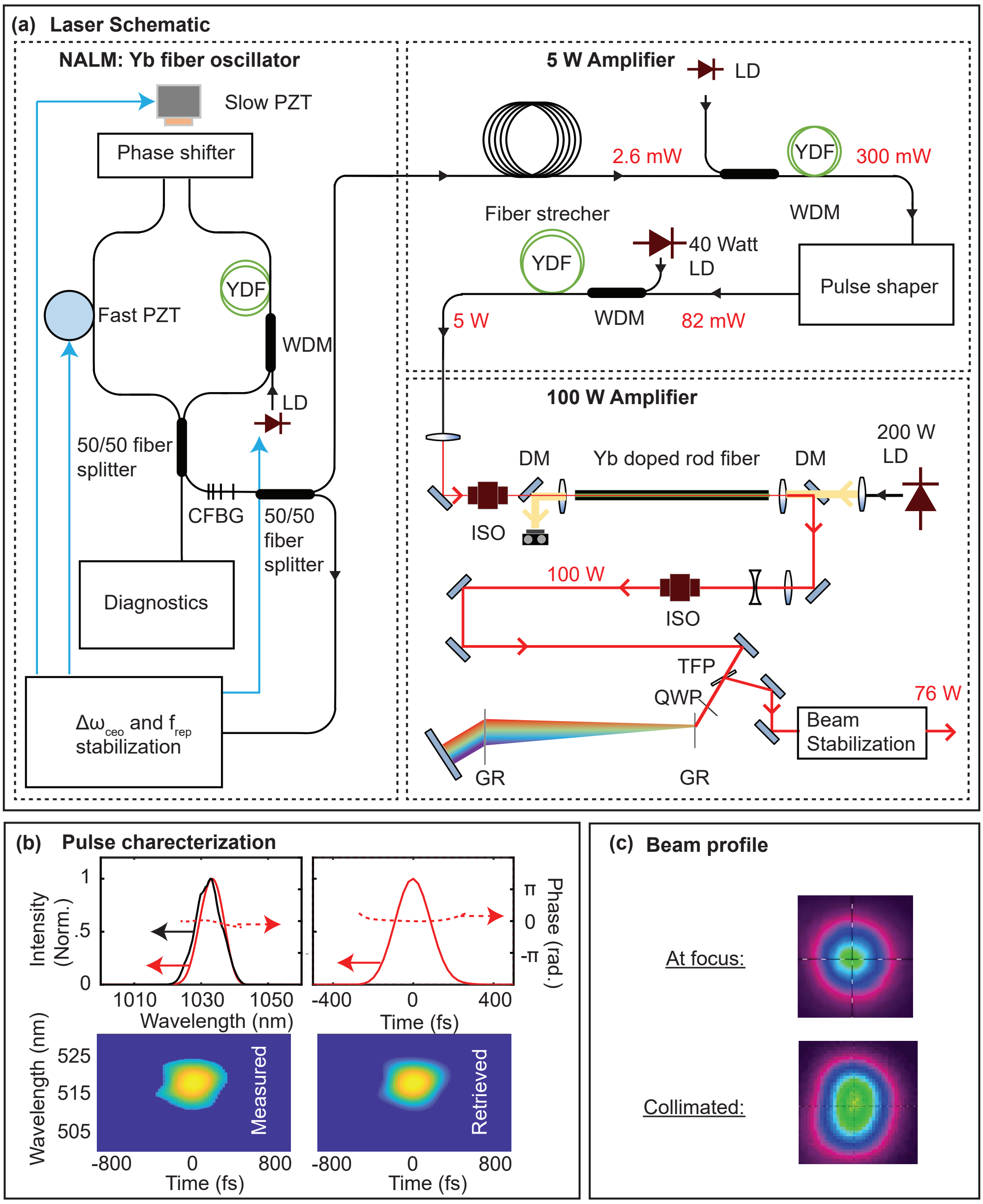

Figure 4.2: (a) Schematic of the frequency comb driving laser: PZT, piezo-electric-transducer. CFBG, chirped fiber Bragg grating. LD, laser diode. WDM, wavelength division multiplexer. YDF, ytterbium-doped fiber. WDM, wavelength division multiplexer. ISO, optical isolator. DM, dichroic mirror. TFP, thin film polarizer. GR, Grating. QWP, quarter wave plate. (b) The measured spectrum at the laser output (black), the reconstructed spectrum and temporal intensity (red), the reconstructed phase (red dashed), and the corresponding FROG traces (logarithmic color scale). (c) Beam profiles near the output of the laser: at the focus (top) and when collimated (bottom).

4.3.1 Phase applied by the pulse shaper

It should be noted that the pulse spectrum typically changes due to gain narrowing and SPM during the amplification process. If there are new spectral components that are generated outside the bandwidth of the initial spectra, this can cause a problem for serrodyne shifting, as the phase of the new frequency components cannot easily be shaped. Figure 4.3 (a) shows the laser spectrum after the pulse shaper (black) and after the 100 W amplifier (blue). These are also shown on a logarithmic scale in Figure 4.3 (b). As shown in Figure 4.3 (a), the pulse does not acquire new spectral components outside the initial bandwidth during amplification. We also perform several measurements for different dispersion parameters used by the pulse shaper, while leaving the amplitude unshaped, to verify that this does not affect the laser spectrum. We note that the spectrum at the output of the pulse shaper does not change for different dispersion parameters. The results of the dispersion scan are shown in Appendix C.

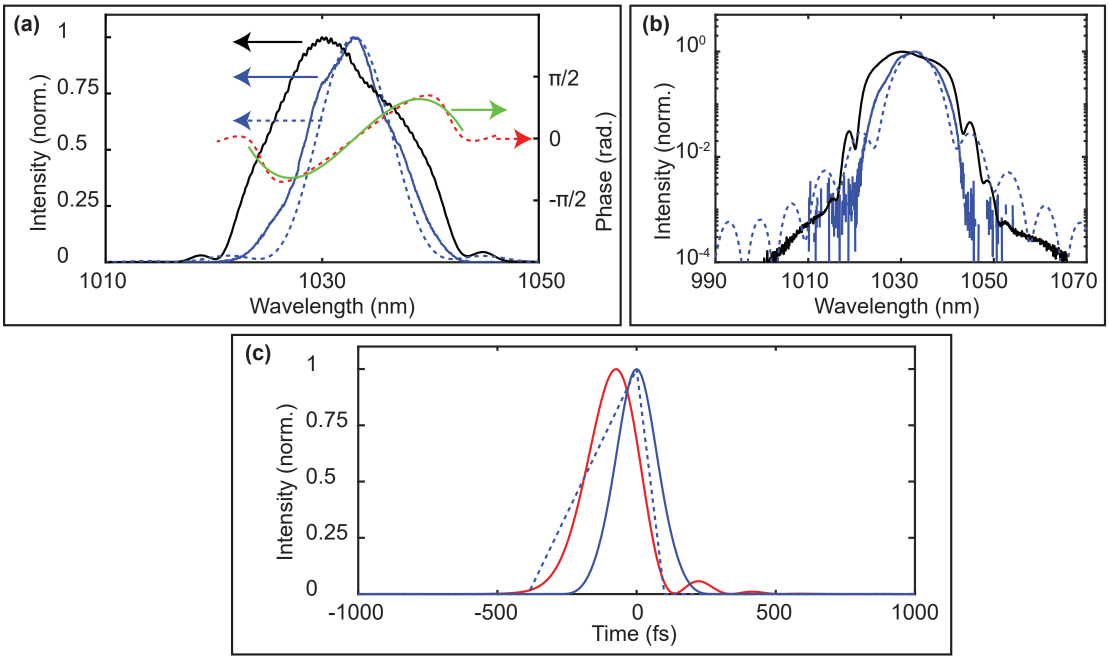

Figure 4.3: (a) Spectral intensity at the output of the pulse shaper (black), after amplification (blue) and spectral intensity of an ideal sawtooth-like triangular pulse with 250 fs FWHM (dashed blue), phase of the ideal sawtooth pulse (dashed red) and a Taylor expansion fitted to the phase of an ideal sawtooth-like triangular pulse pulse (green). (b) Spectral intensities in log-scale corresponding to the data shown in (a). (c) Temporal intensities of Fourier limited pulse calculated using the spectrum after amplification of the laser (blue), pulse with the spectrum at laser output considering the Taylor expanded phase (red) and an ideal sawtooth-like triangular pulse (dashed blue).

For an efficient shift neglecting bandwidth limitations, the ideal pulse shape is a sawtooth-like triangular pulse in the temporal domain. The spectrum (dashed blue line) and phase (dashed red) corresponding to a sawtooth-like triangular pulse with a pulse duration of 250 fs (FWHM) in the spectral domain are shown in Figure 4.3 (a). The sawtooth-like triangular pulse spectrum (dashed blue) is also shown in logarithmic scale in Figure 4.3 (b). In this experiment, we limit ourselves to only phase shaping. The main reason why we did not shape the amplitude of the pulse is that, in contrast to phase shaping, amplitude shaping influences the amplification process and can even lead to amplifier damage. Furthermore, the spectrum corresponding to a perfect sawtooth-like triangular pulse requires spectral components outside the bandwidth of the laser pulse, as shown in Figure 4.3 (b). We can solve this problem by selecting a pulse with a longer temporal duration. However, this complicates the design of the MPC need for serrodyne frequency shifting due to the reduction of peak intensity of the pulse. The phase of a sawtooth-like triangular pulse can be approximated by using a Taylor expansion until the third order dispersion (TOD). Figure 4.3 (a) shows the closest fit (green). The temporal profile of the pulse with the spectrum of the laser and the considered phase obtained via the Taylor expansion is shown in red in Figure 4.3 (c). The shaped pulse reveals a clearly asymmetric shape, deviating, however, from the ideal pulse shape.

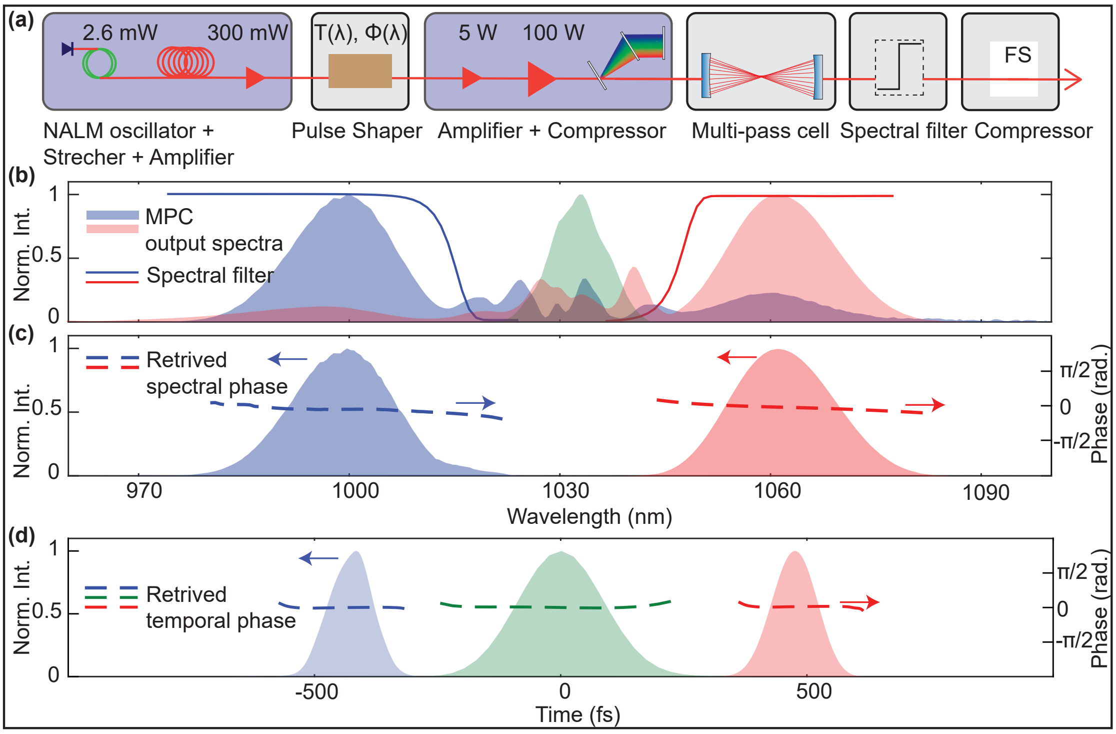

Figure 4.4: Setup and spectral-shifting results. (a) Schematic of the experimental setup, including the high-power frequency comb laser (blue boxes) complemented by pulse shaper, MPC, spectral filter and fused-silica glass compressor (FS) for wavelength-tuning (gray boxes). (b) Measured spectrum at the MPC input (green) as well as at the output shifted to 999 nm (blue) and to 1062 nm (red), along with the transmission of the spectral filters (solid lines). (c) Corresponding measured spectra and retrieved phases of the output pulses after spectral filtering and compression. (d) Corresponding temporal intensity profiles and phases derived from FROG measurements, which are displayed together with the reconstructed MPC input laser pulse (green). This figure is reprinted from Ref. [140]

4.3.2 Spectral shifting

The schematic of the experimental setup for spectral shifting the high-power laser is shown in Figure 4.4 (a). The laser is coupled with a mode-matching telescope into the MPC. The MPC used in this setup is the same as the MPC used in section 3.2. At the MPC output, the laser beam is collimated and sent for spectral filtering. The spectral filtering is performed with a dielectric edge pass filter, using a double reflection or transmission geometry depending on the selected wavelength range. By tuning the angle of the spectral filter, we can select the location of the spectral cut. Following the spectral filter, the pulses are sent to a compressor. Contrary to SPM-based spectral broadening of Gaussian pulses in an MPC, the serrodyne-shifted pulses exhibit a positively chirped pulse at the MPC output. We therefore compress the spectrally shifted pulses with fused silica.

Figure 4.4 (b) shows the input spectrum of the laser sent into the MPC, as well as the corresponding output spectra after the MPC for optimized pulse shaper settings, which yield spectral shifts to 999 nm and 1062 nm. Figure 4.4 (c) shows the corresponding filtered spectra obtained using spectrally tunable dichroic mirrors. After spectral filtering, we reach 66.7 % (41.5 W) and 63 % (39.2 W) of the optical power transmitted through the MPC, which is centered at 1062 nm and 999 nm, respectively. The spectrally-shifted pulses, after undergoing spectral filtering, can be compressed to durations of 106 fs (1062 nm) and 92 fs (999 nm) by passing them through 119 mm and 100 nm of fused silica, respectively. Figure 4.4 (d) displays the temporal reconstruction from FROG measurements of the laser output pulses at 1030 nm, as well as the spectrally shifted and compressed pulses, revealing excellent temporal pulse quality.

It should be noted that the temporal pulse shape after the MPC is similar to the input pulse shape. The dispersion-compensating MPC design ensures this. The pulse profile changes to a Gaussian shape after the spectral filter and compressor.

In addition, we verify the spatial beam quality after spectral shifting. With an input beam quality parameter $M^2 = 1.2 \times 1.4$, we obtain output beam parameters of $M^2 = 1.2 \times 1.3$ at 1062 nm and 1.3×1.6 at 999 nm.

4.3.3 Efficiency limitations of the serrodyne-frequency-shift

An important factor that determines the extent of the spectral shift for the serrodyne-frequency-shifting method developed in this dissertation is the dispersion management in the MPC to maintain the temporal pulse shape while it accumulates a linear phase in the temporal domain due to SPM. In the MPC, the dispersion acquired within the 10.35 mm fused silica plates used as nonlinear medium is compensated by the dispersion provided with the help of the dielectric coating of the MPC mirrors. Hence, while propagating in the MPC, the pulse experiences a near net zero dispersion per round trip.

Another reason which may cause a change of the temporal pulse profile during propagation within the MPC is a loss of spectral components of the pulse. In this dissertation, the MPC mirrors support pulses with a spectrum in the wavelength range from 980 nm to 1080 nm. As shown in Figure 4.4 (b), we note that the MPC output spectra, which correspond to spectral shifts at 999 nm and 1062 nm, extend to the edges of the MPC mirror bandwidth, limiting the wavelength-tuning range in our experiment. However, today's state-of-the-art dielectric coatings allow for a broadband design with a bandwidth of a few hundred nm. In section 6.2.2, we show an example simulation in which the center wavelength of a laser can be tuned by 50 THz (in the previous subsection, we have experimentally demonstrated a spectral shift of 17.8 THz). bringing wavelength-tuning of lasers far beyond the gain bandwidth of the state-of-the-art laser amplifiers into reach.

Another important factor that influences the pulse shape is the B-integral that is acquired by the pulse between the pulse shaper and the MPC. To understand the importance of this effect, we first test a laser configuration where the components of the 5 W amplifier section are rearranged by taking 90 m polarization maintaining stretcher fiber

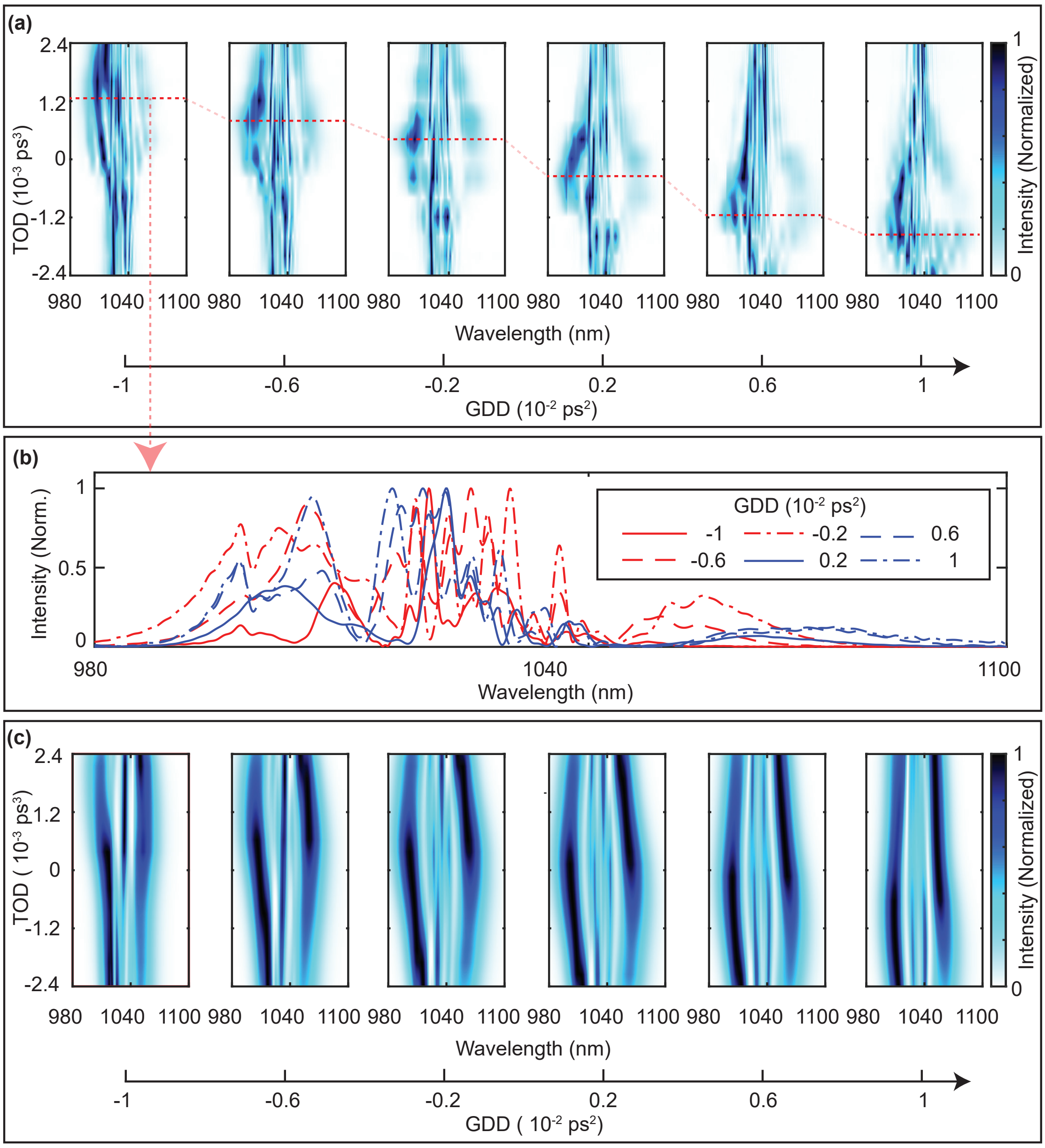

Figure 4.5: (a) The output spectrum of the MPC observed when the GDD applied by the pulse shaper is tuned in the range from -1 $\times$ 10^{-2} ps^2 to 1 $\times$ 10^{-2} ps^2 and the TOD applied by the pulse shaper is tuned in the range from -2.4 $\times$ 10^{-3} ps^3 to 2.4 $\times$ 10^{-3} ps^3. (b) The corresponding spectra at the MPC output for the GDD and TOD applied by the pulse shaper indicated by the dashed red lines in (a). (c) The simulated spectrum at the output of the MPC when the GDD and TOD values are applied to a Fourier-limited pulse at the output of laser.

from the fiber stretcher and placing it after the pulse shaper. A table showing the B-integral values for the configuration used in section 4.3.2 and the configuration with a larger B-integral as discussed above are shown in table 4.1. The B-integral is calculated using the RP fiber power software[141]. We note that the largest contribution to the B-integral accumulated between the pulse shaper and the MPC in the 2nd configuration is due to the propagation of pulse in the 90 m polarization maintaining strecher fiber.

Configuration :	(1)	(2)
Component	B-integral (rad.)	B-integral (rad.)
90 m stretcher fiber	-	5.98
Yb doped active fiber for 5 W amplification	2.13	2.11
100 W amplifier	0.67	0.6
Total	2.8	8.69

Table 4.1: B-integral accumulated by the pulse during propagation between the pulse shaper and the laser output in the laser configurations used in (1) section 4.3.2 and (2) section 4.3.3.

The influence of the B-integral between pulse shaper and MPC can be revealed via pulse shaper dispersion scans. In order to perform a dispersion scan, we scan the TOD of the pulse shaper in the range from $-2.4 \times 10^{-3}\,\mathrm{ps}^3$ to $2.4 \times 10^{-3}\,\mathrm{ps}^3$ at each GDD value applied by the pulse shaper in the range from $-1 \times 10^{-2}\,\mathrm{ps}^2$ to $1 \times 10^{-2}\,\mathrm{ps}^2$. The pulse shaper dispersion values displayed in Figure 4.5 (a) and (b) have a error margin of $\approx 10\,\%$. Figure 4.5 (a) shows the output spectrum of the MPC observed when we scan over the range of GDD and TOD values. From the two dimensional GDD and TOD grid scan, we select points where the maximum spectral shift is occurring and show them in Figure 4.5 (b). Figure 4.5 (a) and (b) show that the pulse gains several peaks at the center of the spectrum, which leads to a reduction in the efficiency of the serrodyne-frequency-shift. In addition, the 2-D GDD-TOD scan shows that the frequency shift predominantly visible towards the shorter wavelengths. Figure 4.5 (c) shows corresponding simulation results when the same GDD and TOD values are applied to a Fourier-limited pulse from the laser output. By comparing Figure 4.5 (a) and (c), and taking into account, that the experimental results where obtained using configuration (2) while the simulation does not consider any B-integral, we note that the B-integral acquired by the laser pulse in the path between the pulse shaper and the MPC can significantly influence the pulse shape, thereby reducing the efficiency of the serrodyne-frequency-shifting effect to a significant extent. It should be noted that while the reduction of the B-integral by rearranging the pulse shaper and stretcher fiber arrangement shows an improvement in wavelength-tuning, as shown in Figure 4.4, there is still a discrepancy between the experiment and our simulation, which can be likely explained by the remaining low B-integral. This problem, due to the B-integral between pulse shaper and the MPC, could perspectively be eliminated by designing a pulse shaper that can be used after the amplifier of the laser.

4.3.4 Temporal contrast

An advantage of serrodyne-frequency-shifting is that the wavelength-tuned pulses do not necessarily have spectral components in common with the input laser spectrum. In the temporal domain, this implies that any pre- or post-pulse present in the input laser can be removed by serrodyne-frequency-shifting, as the nonlinear process causing the

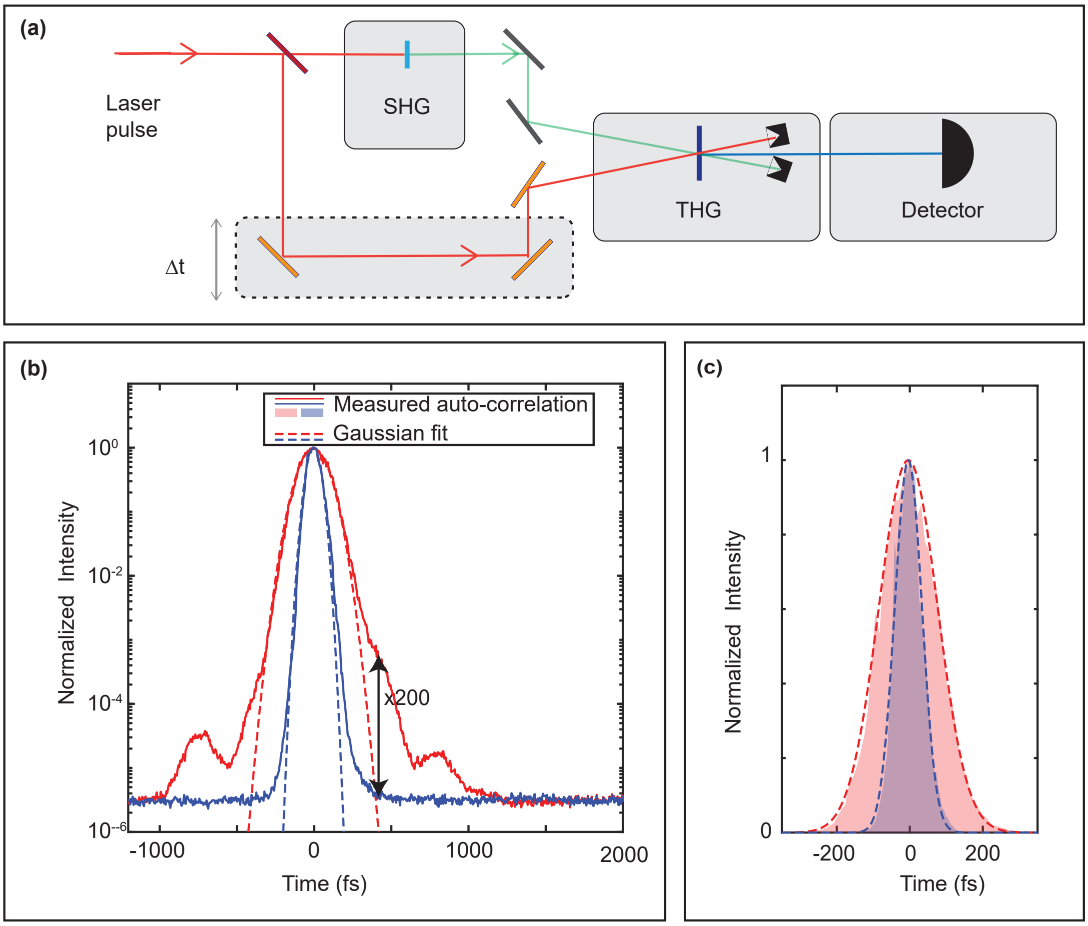

Figure 4.6: (a) Schematic of the third-order auto-correlator. (b) Measured auto-correlation signals (solid lines) and corresponding Gaussian fits (dashed lines) for laser output at 1033 nm (red) and spectrally shifted and filtered pulse at 1062 nm (blue) on a logarithmic scale. (c) The auto-correlation signals in (b) are shown on a linear scale. This figure is reprinted from Ref.[140]

spectral-shift does not influence the weak pre/post pulses. We can thus improve the temporal contrast of the laser. With motivation from the benefits of improving temporal contrast in applications such as electron or ion acceleration[142,143] or nonlinear spectroscopy[144], and encouraged by the high-quality temporal FROG retrievals shown in Figure 4.4(d), we build a third-order auto-correlator to carry out high-dynamic range temporal pulse characterization.

Figure 4.6 (a) shows the setup diagram for the third-order auto-correlator. Firstly, infrared laser pulses with a pulse energy of about 0.5 μJ are divided into two arms of an interferometer. In the first arm, a second harmonic signal is generated using a type I beta barium borate (BBO) crystal that is 50 μm thick. The second harmonic pulses are then combined non-collinearly with the second interferometer arm and focused into a type-II BBO crystal that is 50 μm thick to generate a third harmonic signal. A motorized delay stage is used to adjust the temporal delay between the fundamental and the second harmonic beam. The third harmonic signal is then detected with a biased UV-enhanced silicon photodiode.

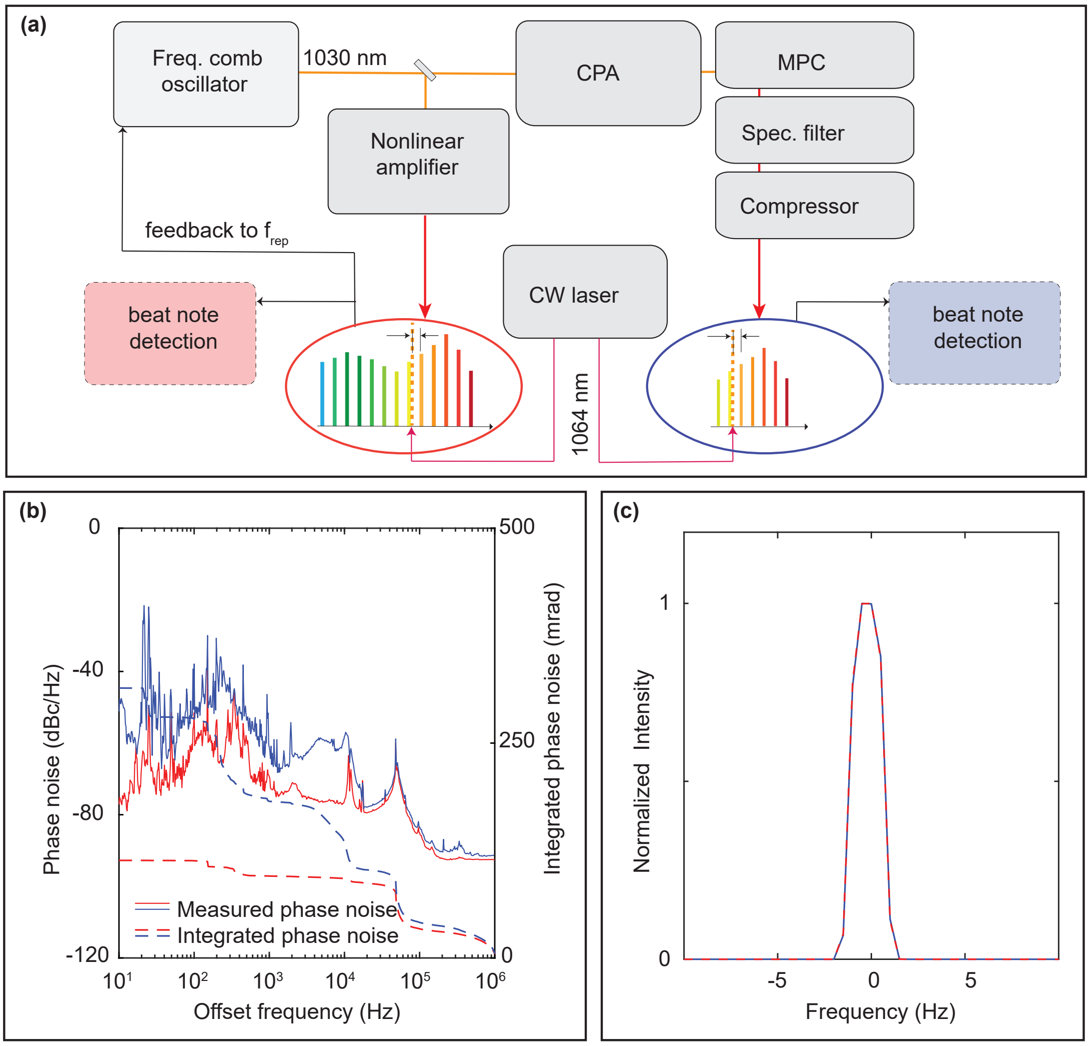

Figure 4.7: (a) Schematic of the beat note phase noise measurement. (b) Measured in-loop phase noise (red solid line), and beat note phase noise of the spectrally shifted laser with the CW laser (blue solid line) displayed together with the integrated phase noise (dashed lines). (c) The beat notes of the NALM oscillator with the CW laser (red), and the spectrally shifted laser with the CW laser (blue dashed). This figure is reprinted from Ref. [140]

Figure 4.6 (b) shows the intensity cross correlation between an input pulse and its second harmonic for an input center wavelength at 1033 nm (red) and the intensity cross correlation between a wavelength-shifted and spectrally filtered pulse at 1062 nm and its second harmonic (blue) on a logarithmic scale. We note that the temporal pedestals are reduced by a factor of atleast 200, the measurement being limited by the dynamic range of our detector. Figure 4.6 (b) also shows a Gaussian curve fitted to the intensity cross correlation of the input pulse at 1033 nm (dashed red) and of the wavelength-shifted and spectrally filtered pulse at 1062 nm (dashed blue). The results in Figure 4.6 (b) are shown on a linear intensity scale in Figure 4.6 (c). These results clearly show that, unlike typical post-compressed pulses with temporal pre- and post-pulses [145], the frequency-shifted pulses have a nearly perfect Gaussian shape over a large dynamic range.

4.3.5 Coherence

A important factor we need to consider for spectroscopy is the coherence of the frequency comb laser after serrodyne-frequency-shifting. We thus examine the coherence characteristics of the spectrally shifted high-power laser. Figure 4.7 (a) shows the schematic of the setup used to measure coherence. First, a part of the output NALM oscillator of the laser is nonlinearly amplified and used to lock to a stable continuous wave reference laser choosing a lock-offset frequency between the two lasers of 20 MHz. The CW laser has a linewidth around a few kHz and a wavelength of 1064 nm. The CW laser is also used to produce a heterodyne beat note with the frequency-shifted output after the MPC, which is centered at 1062 nm.

Figure. 4.7 (b) displays the measured in-loop phase noise of the laser locked to the CW reference laser and the phase-noise of the beat note of the wavelength-tuned laser with the CW laser. Figure. 4.7 (c) shows the corresponding beat notes, indicating Hz-level linewidth support. We find that the integrated phase noise (10 Hz to 1 MHz) of the laser and spectrally shifted output amount to 113.5 mrad and 314.1 mrad, respectively, corresponding to about 99 % and 90 % of the power contained in the carrier[146]. This result demonstrates excellent coherence properties of our method and sets an upper limit for possible coherence degradation due to the frequency-shifting process. Furthermore, a low output phase noise of the shifted output implies a low input amplitude noise due to amplitude-phase noise coupling caused by the nonlinearity of the MPC.

4.4 Enhancement cavity

As discussed at the introduction of chapter 4, an important requirement to take into account when building a VUV laser for spectroscopy of the low energy nuclear transition in ^{229}Th is that the natural linewidth of this transition is in the order of a few mHz and has a very low probability of excitation due to its long lifetime (in the order of 10^3 s). Even if the ^{229}Th atom is doped in a crystal, this linewidth is expected to broaden to only a few tens of kHz. Therefore, it is important that we produce a VUV laser with high power per comb line. The power per comb line of a laser is proportional to the repetition rate of the laser f_{rep}. Therefore, in this dissertation, we choose a high repetition rate laser (f_{rep} = 65.3 MHz) as a driving laser for VUV generation. Due to the high repetition rate of the laser, however, the laser pulse energy is the order of a μJ. Hence, to achieve the peak power in the order of 10^{14} W/cm^2 necessary for HHG, we rely on a passive optical resonator called enhancement cavity, which can provide the necessary enhancement. The generation of a VUV frequency comb laser with a high repetition rate laser in an enhancement cavity was first reported nearly in parallel by R. J. Jones et al.[147] and C. Gohle et al.[148] in 2005. In this section, we describe the experimental setup built for the development of a VUV frequency comb source using an enhancement cavity designed to support pulses with center wavelengths in the range from 1000 nm to 1070 nm, and then discuss our preliminary results.

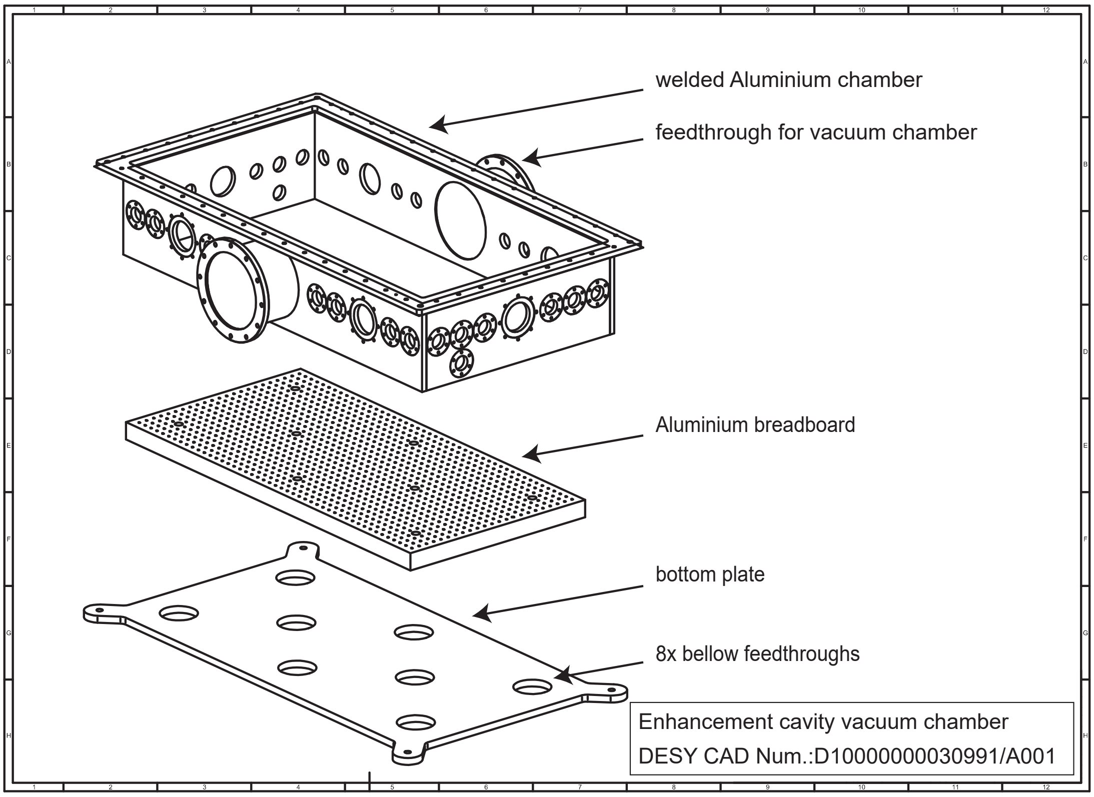

Figure 4.8: Schematic of the vacuum chamber used to build the enhancement cavity under high vacuum conditions. The many ports are used for ultrashort pulse diagnostics, as well as for production and monitoring of high vacuum conditions required for VUV generation. The eight holes in the base plate are used to isolate the optical breadboard from the vacuum chamber.

4.4.1 Vacuum chamber

When the cavity is operated at a high intra-cavity power of a few kW, the dispersive and nonlinear properties of air can disrupt the finesse and intensity at focus in the cavity. In addition, air can absorb laser radiation at 150 nm. Therefore, the enhancement cavity must be built in a vacuum chamber. The schematic of the vacuum chamber used for the cavity is shown in Figure 4.8, and the detailed CAD diagram showing the cross section of the vacuum chamber on an optical breadboard is shown in Figure 4.9 (a). During the experiment, a 7×10^{-7} mbar vacuum is achieved in the chamber with a scroll pump and a turbo molecular pump. The mechanical noise caused by the inherent vibrations of the vacuum pumps is not transmitted to the breadboard or optics, as they are mechanically de-coupled from the vacuum chamber, as shown in Figure 4.9 (b).

The presence of hydrocarbons in the vacuum chamber is a major concern. The reason is that hydrocarbons can disintegrate in the vacuum chamber when they interact with VUV or XUV radiation and attach to optics[55,59]. This leads to a degradation of the performance of the cavity when operated over long periods. In order to avoid this contamination and degradation of mirrors, we purge the vacuum chamber with ozone supplied at a very low pressure.

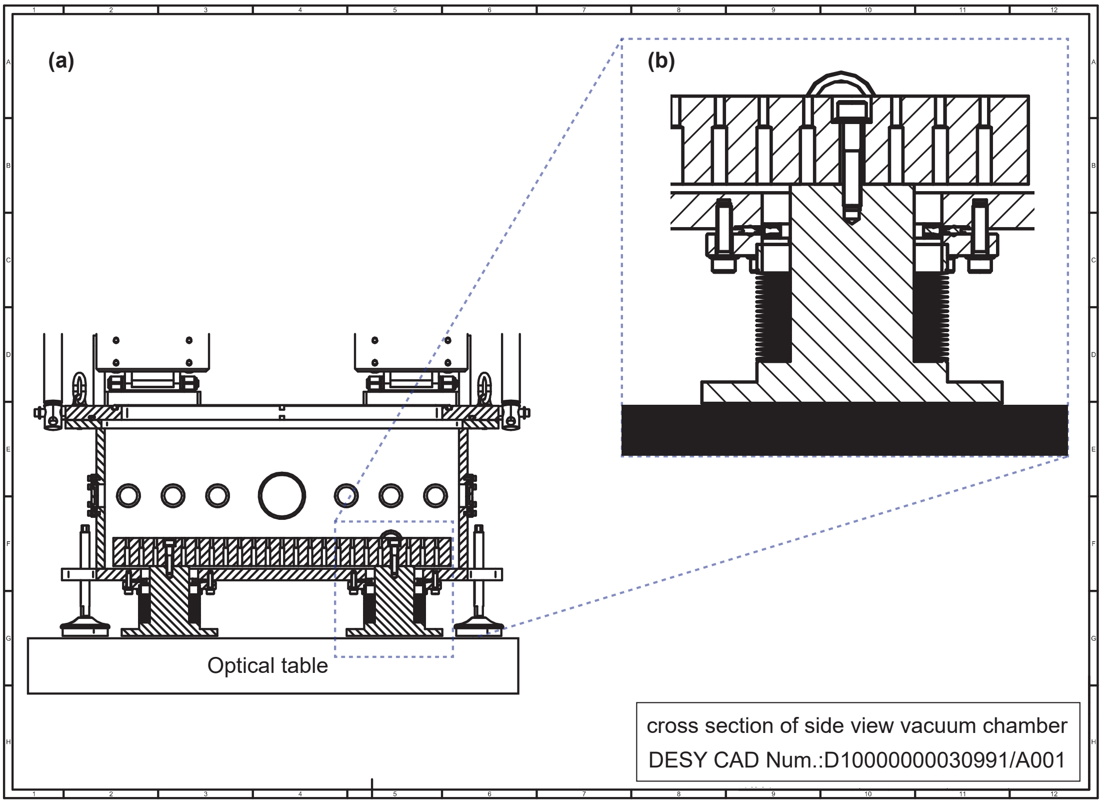

Figure 4.9: (a) Cross-section of the vacuum chamber. (b) The enlarged section shows that the optical breadboard is isolated with the help of bellows from the vacuum chamber and the base plate. The mechanical decoupling of the breadboard from the vacuum chamber is important for stable cavity locking mitigating mechanical noise transfer from the vacuum pumps.

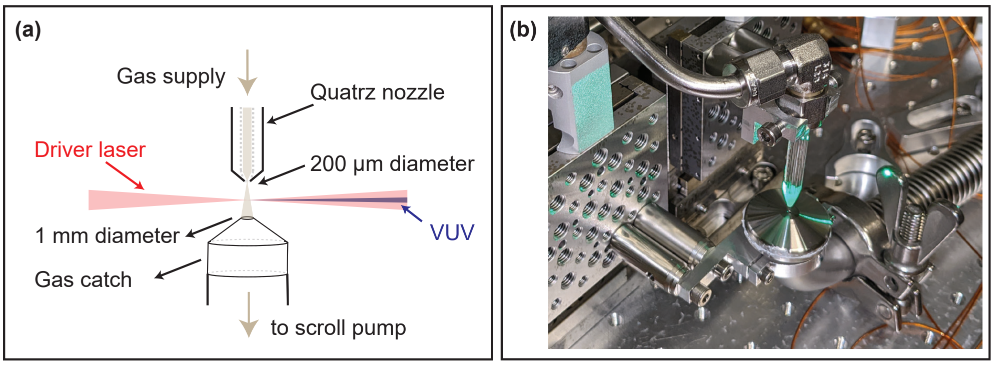

Figure 4.10: (a) Schematic of the quartz nozzle and the gas catch as used in the cavity. (b) Photograph of the gas jet assembly in the cavity.

4.4.2 Gas jet

At the center of the cavity, a quartz capillary with 6 mm outer diameter and 2 mm inner diameter, which tapers to a nozzle with 200 μm orifice diameter, is used to inject Krypton gas. The pressure is 12 bar at the capillary's input. As a result, the pressure in the vacuum chamber increases. To improve the chamber pressure, a gas catch (connected to a vacuum pump) is installed below the quartz nozzle, as shown in Figure 4.10. The position of the nozzle and the gas catch are independently controlled with the help of two 3-axis translation stages.

4.4.3 Laser-cavity stabilization

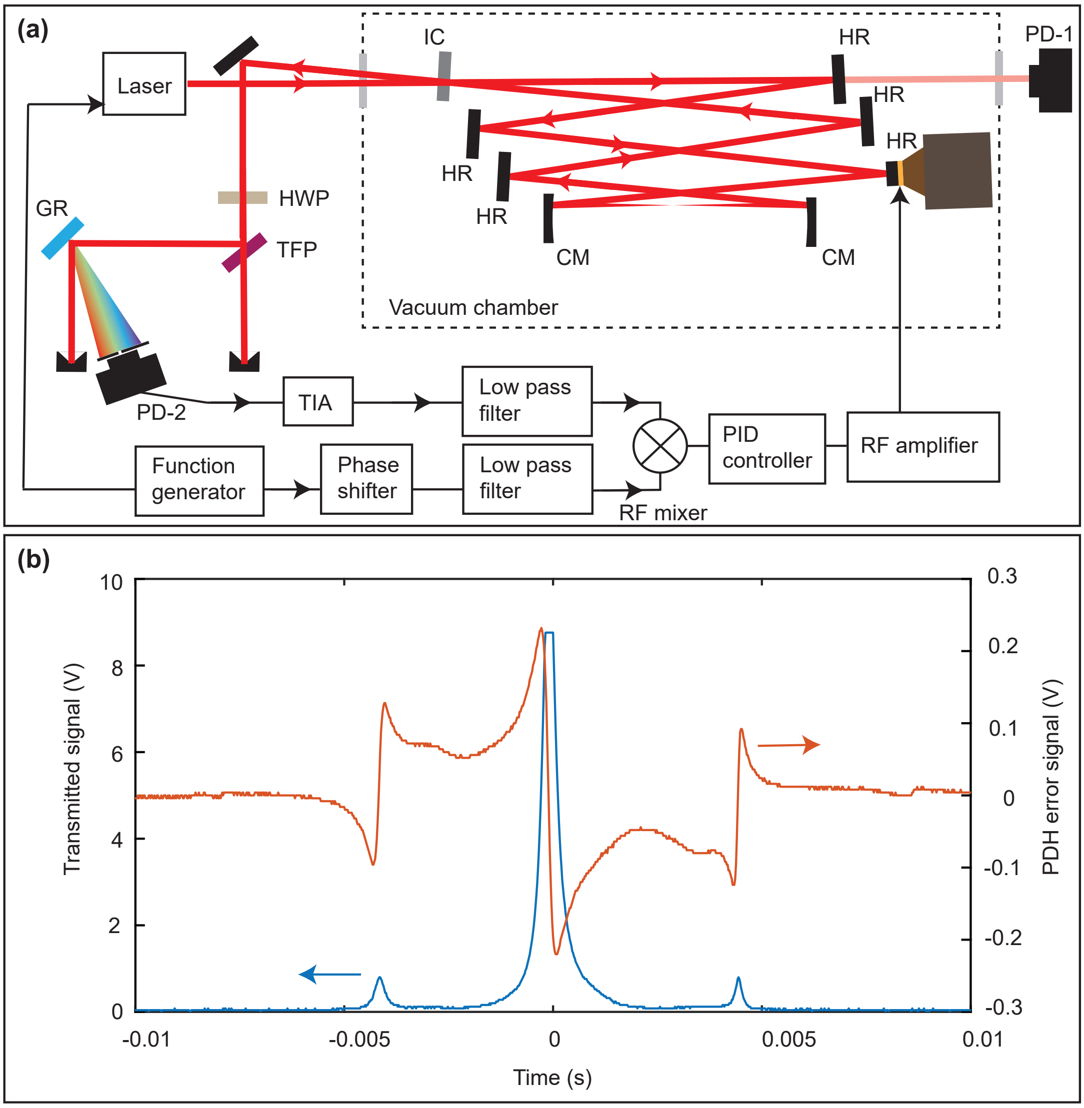

Figure 4.11: (a) Schematic of the setup used to lock the cavity to the laser: PZT, piezo-electric-transducer. PID, proportional–integral–derivative controller. PD, photodiode. HR, high reflectivity mirror. CM, curved mirror. IC, input coupler. TIA, trans-impedance amplifier. TFP, thin film polarizer. GR, grating. HWP, half wave plate. (b) Pound-Drever-Hall error signal (red) and the transmission signal of the cavity (blue), while the length of the cavity is scanned over a cavity resonance.

The length of the enhancement cavity is stabilized to the laser by locking the cavity length to the laser repetition rate using the Pound-Drever-Hall (PDH) approach[149]. The schematic for the cavity stabilization scheme is illustrated in Figure 4.11 (a). In this method, we first generate sidebands at 900 kHz by driving a mechanical resonance in the peizoelectric transducer (PZT) of the NALM:Yb fiber oscillator. We chose 900 kHz because the PZT in the NALM: Yb fiber oscillator has a resonance at this particular frequency. The details of the frequency response of the PZT in the laser are discussed in Appendix D. After the high-power frequency comb laser is injected into the cavity, the reflected light is first attenuated to 1 W, and then angularly dispersed using the first-order reflection of a grating with 1000 lines / mm. With a slit, a very narrow frequency window is selected and detected on a silicon photodiode with a bandwidth of 150 MHz. The signal is then amplified with an trans-impedance-amplifier (TIA). The signal from the TIA is first filtered with a low pass filter at 1.9 MHz and mixed with a phase-shifted copy of the reference signal at 900 kHz, which is used for side band generation. After the mixer, we obtain a PDH error signal as shown in Figure 4.11 (b). The error signal is used to generate a discriminant with a PID controller. The signal from the PID controller is then fed into a high-voltage PZT driver (which supports a bandwidth of 100 kHz) to control a PZT, which is attached to a mirror in the enhancement cavity.

The resonance properties of the mirror attached to the PZT in the cavity play a crucial role for achieving a stable PDH lock. A detailed description of the mirror-assembly and the measured amplitude and phase noise of the mirror-assembly are described in Appendix E. The measurements show that the first resonance of this mirror-assembly occurs at 19 kHz.

4.4.4 Intensity determination at the cavity focus

The peak intensity in the enhancement cavity can be calculated when the beam waists at the focus and intra-cavity power are known.

In order to find the beam waist at the focus of the cavity, we use the fact that the cavity modes will only be in resonance when the total round trip phase is either zero, or an integer multiple of 2π. The mode spacing between two modes can be obtained by looking at the transmission signal that is measured when the cavity length is scanned by applying a voltage to the PZT in the cavity, as shown in Figure 4.12 (b). The data from the experiment show that the distance between the modes HG_{00} and HG_{01} is 2.91 ms. By using the fact that the distance between two successive HG_{00} modes in an enhancement cavity is λ (1.03 μm), we conclude that the distance between HG_{00} and HG_{01} is 0.408 μm. Based on the calculations using equation (2.52), we determine that this distance corresponds to a curved mirror separation of 17.6 mm, a beam waist of $\approx$ 20.5 μm along the tangential plane, and a beam waist of $\approx$ 18.1 μm along the sagittal plane.

To measure finesse of the cavity, we use the cavity ring down method. We first sweep the PZT in the NALM oscillator of the laser at a sweep frequency of 100 kHz and an amplitude of 10 V peak to peak. With the PZT in the laser, we can fill and remove the pulses from the enhancement cavity, which helps us generate a ring-down signal. At the same time, we also sweep the PZT in the cavity over the HG_{00} mode with the highest peak intensity, with a sweep frequency of 60 Hz and an amplitude of 60 Volts peak to peak, and observe the transmitted cavity signal on an InGaS photodiode with a 2 GHz bandwidth. Figure 4.13 (a) shows the transmitted cavity signal. Figure 4.13 (b) shows a zoomed view revealing individual pulses. In order to accurately discern the finesse from the data, we use an exponential fit to estimate the decay time of the cavity, as detailed in equation (2.47). Figure 4.13 (c) shows the exponential fit to the data as a

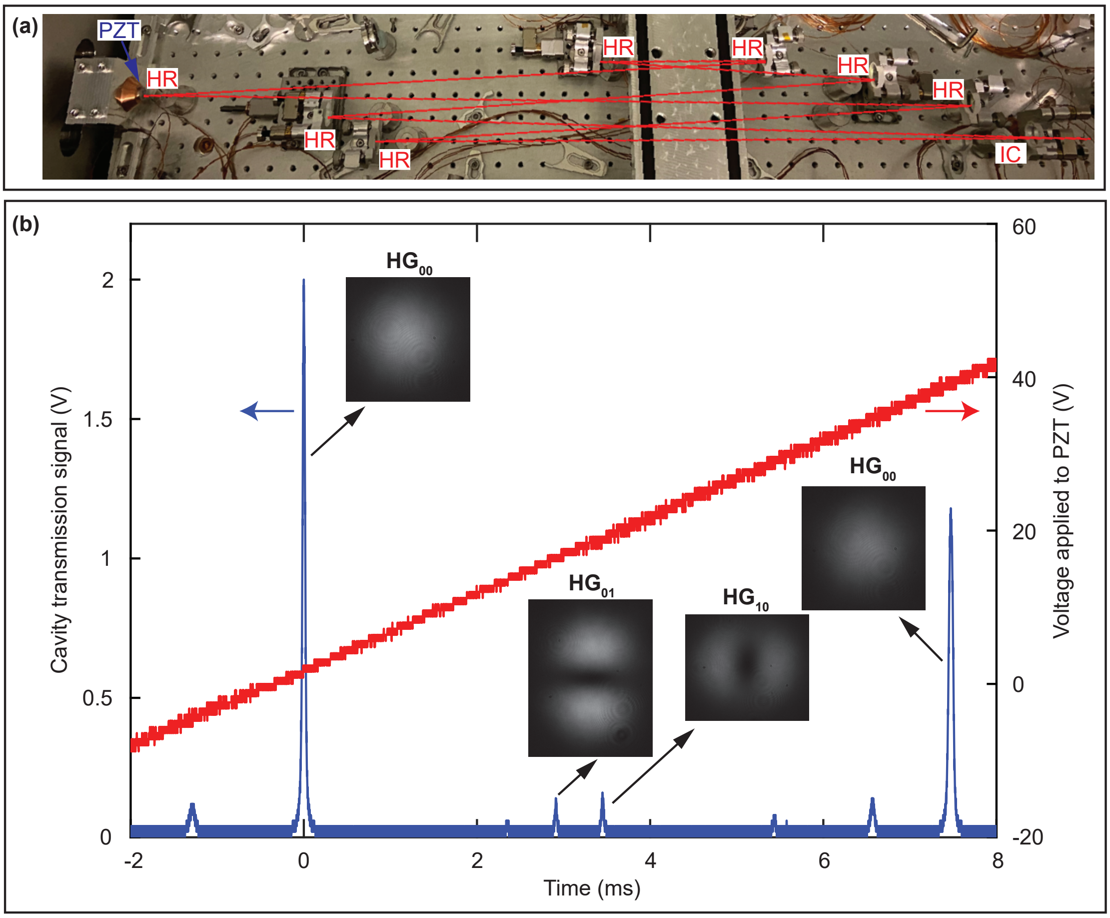

Figure 4.12: (a) Photograph of the cavity taken when the vacuum chamber is open; HR: high reflectivity mirror, IC: input coupler. (b) The transmitted signal (blue) from the cavity measured on a photodiode and the signal applied (red) to the PZT within the cavity. The HG_{00}, HG_{10}, HG_{01} modes observed with a CMOS camera are shown as insets.

red dashed line, revealing the decay time of the intra-cavity power as $\approx 1.03\,\mu$s. From the decay time, the finesse of cavity is calculated using equation (2.49), yielding $\mathcal{F}_{\text{ec}}$ = 422.

An alternative method of measuring finesse during the ring-down measurement is to measure the reflected signal from the cavity, as reported e.g. by C. Benko et al.[55]

Using the estimated beam waists at the focus and the estimated finesse from measured data shown in Figure 4.13, an estimate for the peak intensity at the focus of the cavity can be calculated as[35]:

$$I_{\text{focus}} = \frac{2P_{\text{avg}}T_i\mathcal{F}_{ec}^2}{\pi^3 w_{0-x}w_{0-y}\,\tau_{\text{FWHM}}\,f_{\text{rep.}}} \tag{4.1}$$

Where τ_{FWHM} is the pulse duration of the pulse inside the cavity, P_{avg} is average power of the laser coupled into the cavity. We assume that the pulse duration inside the cavity is the same as the pulse duration at cavity input. During the experiment the laser power sent into the cavity is 70 W. The intensity estimate we obtain from equation (4.1) is $2.42 \times 10^{14}\ \text{W/cm}^2$. However, this intensity estimate does not take into account the

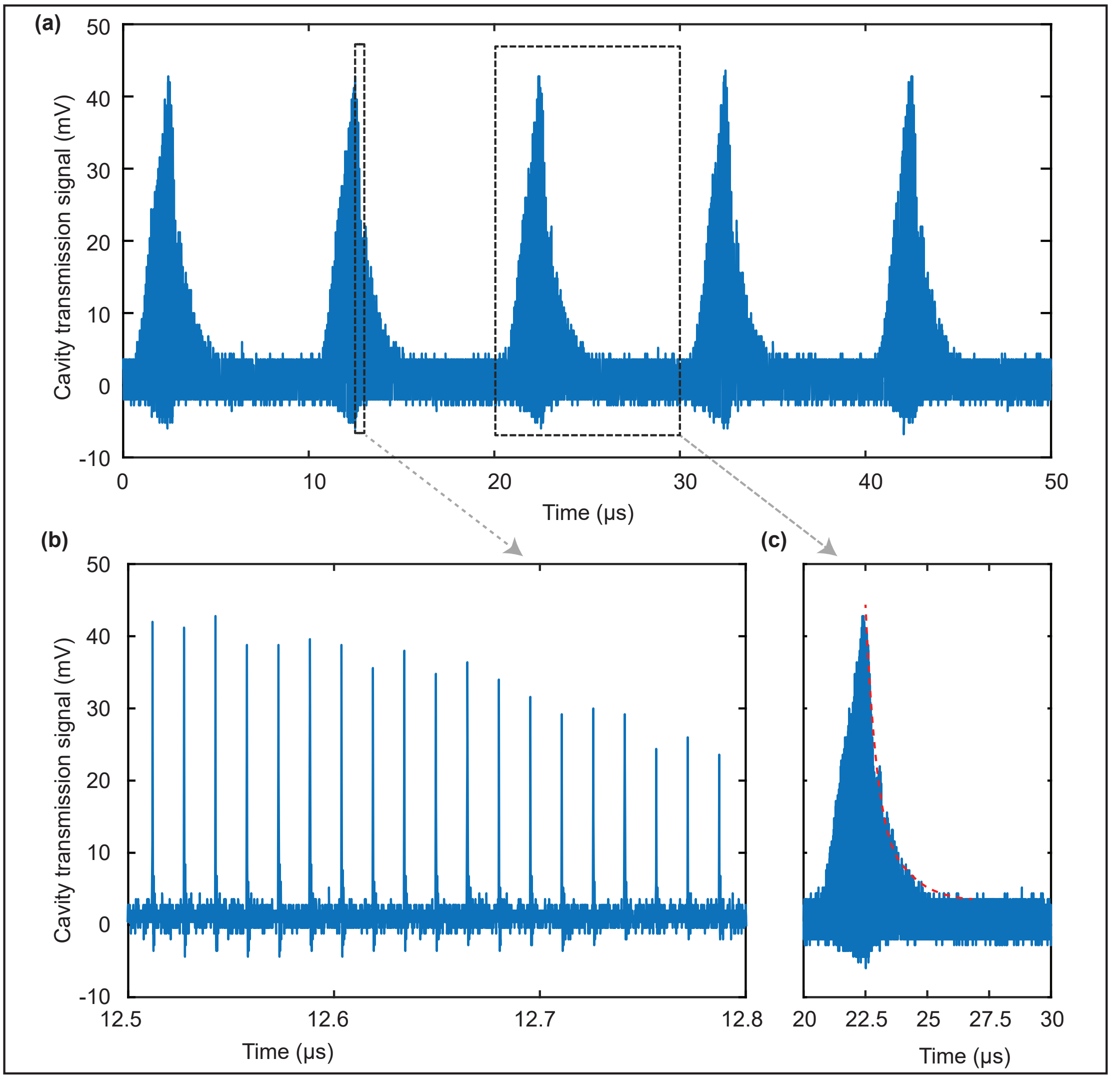

Figure 4.13: (a) Transmission signal of the cavity measured using the leakage beam from a cavity mirror. (b) Signals which correspond to individual pulses during the cavity ring-down measurement. (c) The curve (dashed red), which is fitted to extract the decay constant, is shown along with the measured signal (blue). This curve fit is used to determine the lifetime of the electric field in the cavity and thus the finesse of the cavity.

part of the input laser power that might not enter into the cavity because of inaccurate mode-matching. Hence, during this experiment, we also measure the intra-cavity power ($P_{\text{intra-cavity}}$) in the cavity by calibrating the transmitted optical signal from one of the cavity mirrors. The intra-cavity power measured is 12.42 kW. This corresponds to an enhancement of optical power by a factor of 177. Using this data, an accurate estimate of peak intensity at the focus of the cavity can be calculated as:

$$\begin{aligned} I_{\text{focus}} &= \frac{2P_{\text{intra-cavity}}}{\pi w_{0-x} w_{0-y}\ \tau_{\text{FWHM}}\ f_{\text{rep.}}} \\ &\approx 1.6 \times 10^{14}\,\frac{\text{W}}{\text{cm}^2} \end{aligned} \tag{4.2}$$

4.4.5 Plasma distortion

In order for an enhancement cavity to generate VUV radiation, a gas jet must be aligned with the focal point of the cavity. One simple way to check this is to check for the distortion of cavity mode due to generation of plasma in the cavity. In order to generate plasma, it is not necessary to enable the PDH lock. We use the PZT-actuated cavity mirror in order to sweep over the cavity resonance.

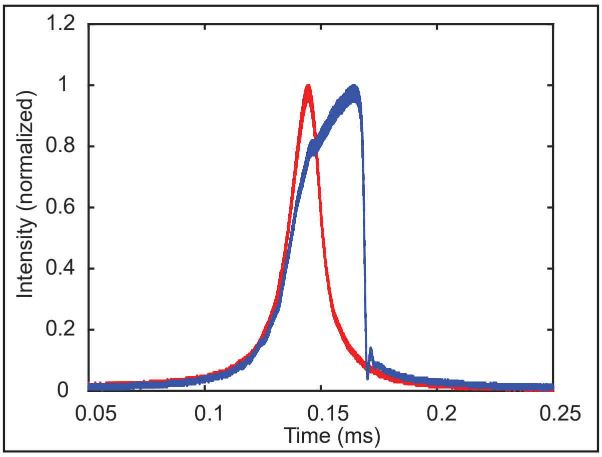

Figure 4.14: Signal of cavity mode in vacuum (red) and in the presence of a gas (blue). This signal is distorted due to the presence of the generated plasma

Krypton gas is injected into the focus of the cavity through a quartz nozzle with a nozzle diameter of 200 μm (as described in section 4.4.2). By looking at the signal of a transmitted beam at one of the cavity mirrors on a photodiode, we can observe if the cavity mode is distorted due to ionization. This allows us to determine when the gas has been ionized and then optimize the position of the gas jet so that it is in the right position with regard to the focal point of the optical beam. Figure 4.14 shows the signal of the detected cavity mode in vacuum and in the presence of the gas jet at the optimal position. We note that the signal is significantly distorted in the presence of plasma. The main reason this occurs is due to the dispersion and B-integral that builds up in the pulse, which is caused by the plasma in the cavity, causing a dynamic shift of the cavity resonance[150]. The observed strong cavity distortion indicates the generation of a highly ionized gas medium. In this condition, laser harmonic can be expected.

4.4.6 Out-coupling of VUV radiation from the cavity

In order to extract the VUV laser produced in the enhancement cavity, it is essential to consider a suitable out-coupling method. During this dissertation, as a first attempt, we choose to place a 100 μm thick plate of fused silica between the curved mirrors in the cavity behind the focus, which serves as a Brewster plate in the cavity. Since the Brewster plate is optimized for near zero Fresnel reflection for the input laser, the Fresnel reflection in the VUV amounts to a few percent. This is due to the different refractive index of fused silica in the VUV. Figure 4.15 (a) shows the calculated reflectivity of VUV radiation at the Brewster plate in the range from 30 nm to 230 nm. The data that we used to estimate the Fresnel reflection of fused silica is taken from R. Marcos et al.[151]

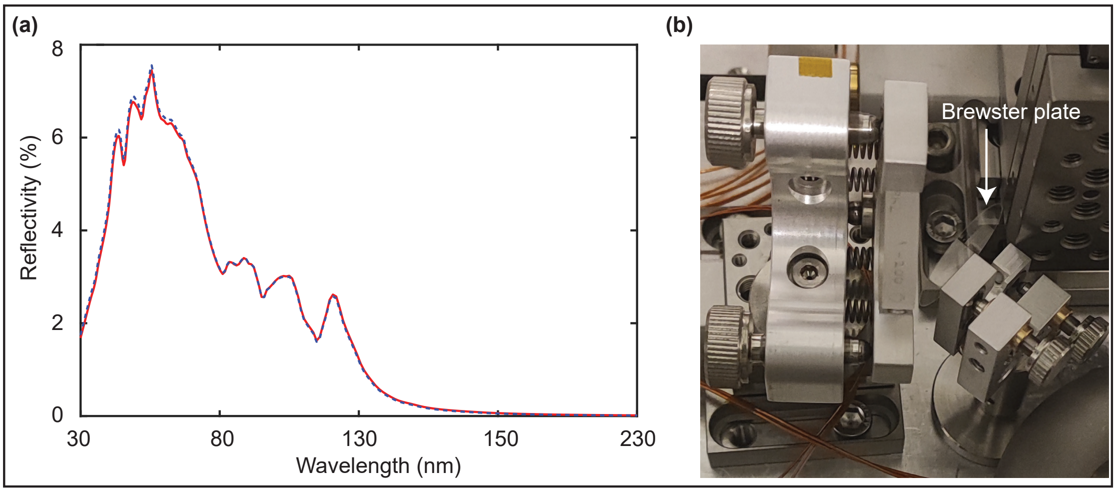

Figure 4.15: (a) The calculated reflectivity of the Brewster plate in the VUV when placed in an enhancement cavity optimized for a laser with center wavelengths at 1033 nm (red) and 516.5 nm (dashed blue). (b) Photograph of the Brewster plate in the enhancement cavity.

During the experiment, we observe that the diode used to monitor the power after the insertion of Brewster plates shows a value of $\approx$ 79 W for an input laser power of 1 W, which corresponds to a factor of 79 enhancement in the cavity. This is significantly lower than the enhancement factor of 177, measured in section 4.4.4. By measuring the loss of power at the Brewster plate, we find that $\approx$ 0.5 % of optical power is reflected every round trip. Upton optimising the position and angle of the Brewster plate, we were able to reduce this to 0.047 %. However, due to limited time, it was not possible to generate and out-couple VUV radiation.

4.5 A complementary path towards a high average power VUV frequency comb laser

To build an efficient, high-average power VUV source, we can exploit the dependence of the harmonic generation efficiency on the wavelength of the driver laser, as discussed in section 4.2. Figure 4.16 shows a simulation of the nonlinear dipole response of single target atom (Xe) for Gaussian pulses with pulse duration of 200 fs (FWHM) focused to a peak intensity of 10^{14} W/cm^2 with laser center wavelengths at 1030 nm (red) and 450 nm (blue). This simulation is performed using the *HHG-max* code developed by M. Hogner[152]. We note that the harmonic yield at wavelengths close to 150 nm (in the region of interest for the spectroscopy of the ^{229}Th nuclear transition) is more than 3 orders of magnitude higher for the driving laser with a center wavelength at 450 nm, compared with the harmonic yield for the driving laser with a center wavelength at 1030 nm. In order to build a high power driving laser at 450 nm, the wavelength of the 1030 nm laser discussed in section 4.2 can prospectively be wavelength shifted to 900 nm, and then by using second harmonic generation, converted to 450 nm. In addition, operation of an enhancement cavity at 450 nm for third harmonic generation needs to be demonstrated. We have started to explore this route by building a second enhancement cavity to test intra-cavity VUV conversion of a green laser.

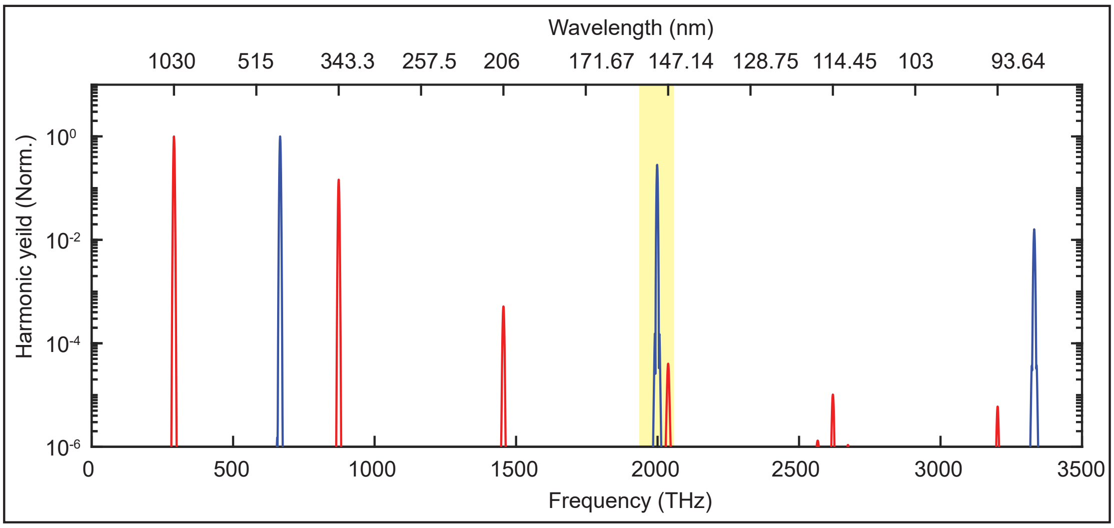

Figure 4.16: The nonlinear dipole response of a single target atom (Xe) when Gaussian pulses with a pulse duration of 200 fs (FWHM) and a center wavelengths at 1030 nm (red), 450 nm (blue) are focused to a peak intensity of 10^{14} W/cm^2. The window that corresponds to the spectral region of interest in the VUV for spectroscopy of the low energy nuclear transition of ^{229}Th is shown in yellow.

4.5.1 SHG and enhancement cavity at 515 nm

In order to explore the above mentioned route towards more efficient frequency conversion into the VUV, we first aim to generate the second harmonic of the IR high-power frequency comb laser discussed in section 4.2, and then build an enhancement cavity at 515 nm. Figure 4.17 (a) shows the schematic of the experimental setup including the SHG setup and the enhancement cavity at 515 nm. SHG is performed with an lithium triborate (LBO) crystal of 3.7 mm thickness (crystal orientation: θ = 90^o , φ = 13.8^o). The crystal was placed in a mount made of copper and stainless steel. In addition, a Peltier device, which acts as a thermoelectric cooler, is placed against the LBO crystal in the mount to stabilize the temperature, as variations in temperature cause fluctuations of the average power of the laser. We chose the beam waist at the center of the LBO crystal of the SHG setup to be relatively large ($\approx$ 70 μm) aiming at high spatial SHG beam quality because the generated laser must have a good overlap integral with a Gaussian mode to efficiently couple the laser into the cavity. The SHG setup delivers an SHG signal with an average power of 31 W, which corresponds to an efficiency of $\approx$ 40 %. The M^2 of the beam is 1.25 $\times$ 1.36. A photograph of the experimental setup for SHG, the photograph of the crystal mount during the SHG operation, and the spectrum obtained are shown in Figure 4.17 (c), (d) and (e), respectively.

The laser at 515 nm is then coupled into the enhancement cavity with an input coupler, 5 plane mirrors and 2 focusing mirrors with a radius of curvature of 150 mm and 200 mm. The input coupler has a transmission of 1.4 %. The specifications of the cavity mirrors are shown in Appendix F. During the initial experiment, we send an input power of $\approx$ 100 mW into the cavity. However, due to the high sensitivity of the silicon detectors at 515 nm, the scattered light on the cavity mirrors is clearly visible with the help of a CMOS camera in a mobile phone, as shown in Figure 4.17 (b).

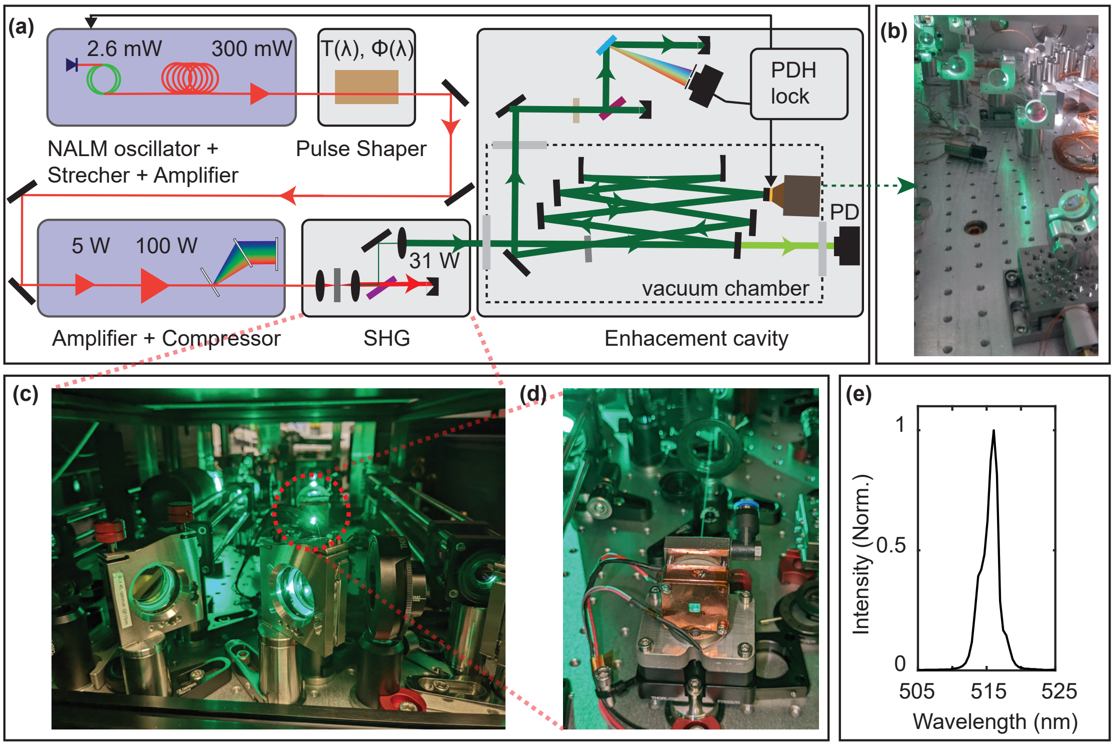

Figure 4.17: (a) Schematic of the experimental setup for SHG and the enhancement cavity at 515 nm. (b) Photograph of the enhancement cavity during operation. (c) Photograph of the SHG setup. (d) Photograph of the mounted SHG crystal during operation. (e) Spectrum of the laser at 515 nm at the input of the enhancement cavity.

4.5.2 Non-collinear cavity

In order to build a high average power VUV source with an enhancement cavity, it is important to consider an efficient out-coupling method. The Fresnel reflection at a fused silica Brewster plate is limited to 8 % (as shown in Figure 4.15 (a)), whereas other optical materials (such as sapphire) can provide a 10 to 15 % Fresnel reflection in the VUV [153]; thus, this value is still low. With the use of dielectric coated plates, an out-coupling efficiency of 75 % has been demonstrated [154]. Although this method is promising, it was observed that VUV radiation caused rapid degradation of the optics. In 2008, D. Yost et al. [155] developed a novel, nano-etched mirror that diffracts the VUV radiation from the cavity. However, this method has shown only 10 % efficiency to date. Using this method, it was observed that hydrocarbon contamination of the nano-etched groves has caused a degradation of the optics. It should be noted that most optical materials suitable for use in enhancement cavities (e.g. TiO_2, HfO_2, Nb_2O_5, Sapphire) are oxides, and oxygen has several transitions in the range from 50 nm to 170 nm, leading to the absorption of VUV radiation [156], which can cause effects such as thermal lensing. Therefore, a logical solution is to explore an option in which the VUV laser and the fundamental driving laser are naturally separated by a geometric angle and therefore do not require an optic to be placed in the optical beam in the cavity.

Promising developments that have shown VUV out-coupling from an enhancement cavity using geometrical methods are: VUV separation with pierced mirrors by I. Pupeza et al. in 2014 [157], and the use of tailored spatial modes of the driving laser by M. Hogner

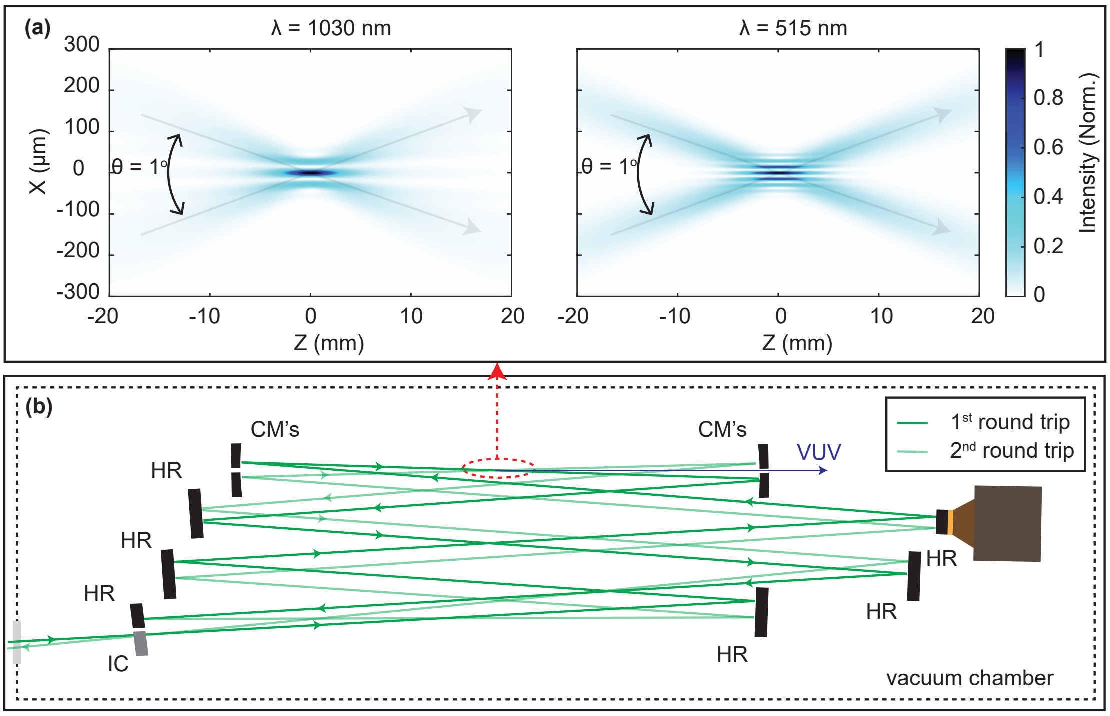

Figure 4.18: (a) Simulated interference patterns of two identical laser beams with wavelengths of 1030 nm (left) and 515 nm (right), focused to a beam waist of 40 μm. (b) Schematic of the non-collinear enhancement cavity with 8 mirrors.

et al. in 2019[158]. These methods can potentially out-couple $\approx$40 % of the XUV light for photon energies close to 100 eV[152,157]. However, the full potential of these methods has not yet been experimentally demonstrated. Recently, in 2020, C. Zhang et al.[159] built an enhancement cavity with a non-collinear geometry to show an out-coupling of 0.6 mW ($\approx$60 % efficiency) at 97 nm. In this particular work, two separate driving laser beams are crossed at the cavity focus, and the pulse energy that is found within the central fringes is then used for VUV conversion. Given the high efficiency of this method, we choose to switch the configuration of the enhancement cavity at 515 nm to a non-collinear geometry. However, building a non-collinear cavity with shorter wavelengths requires a smaller angle between the two laser beams interfering in the focus. Figure 4.18 (a) shows a calculated interference pattern for two identical laser beams when the center wavelengths of the laser is 1030 nm (left) and 515 nm (right), which are focused on a common focal point to a waist of 40 μm. As the divergence angle of the laser is proportional to the wavelength, shorter wavelength lasers need a smaller angle between the two laser beams to ensure that the central fringe contains the maximum energy distribution, and that there is nearly no contribution to HHG from the fringes on either side as this can affect the beam profile of the VUV laser. The schematic of the setup for the non-collinear enhancement cavity at 515 nm is shown in Figure 4.18 (b). To ensure that the two laser beams intersect at the focus, a pin hole with 100 μm diameter is placed at the focal point during alignment of the enhancement cavity. The position of the pin hole is precisely controlled with a 3-axis translation stage.

Envisioned efforts including enhancement tests at 515 nm and intra-cavity VUV generation are discussed in the outlook seciton 6.1.2.

CHAPTER 5

STUDY OF THE LOW ENERGY NUCLEAR TRANSITION IN ^{229}TH AT THE ESR ION STORAGE RING

In this chapter, we discuss an experiment aiming at reducing the energy uncertainty of the ^{229}Th nuclear transition through direct laser spectroscopy at the ESR ion storage ring located at GSI Darmstadt. This dissertation work included participation in an experimental campaign at GSI addressing this challenge.

Based on literature available at the time of this experiment (in the year 2022), we know that the low energy nuclear transition of ^{229}Th lies in the range from 146.6 nm to 152.8 nm[32]. This corresponds to an uncertainty range of 83 THz. Given that the lowest energy nuclear transition energy in a ^{229}Th atom has a natural linewidth in the order of a mHz[131], the ratio of natural linewidth to the uncertainty in the location of the nuclear transition is $\approx 10^{-17}$. The search for this transition can thus be compared to the task of locating an object on Earth, whose size is about the single grain of sand. It is therefore crucial to reduce the energy uncertainty of the ^{229}Th nuclear transition.

This chapter is organized as follows: In section 5.1, we discuss the lifetime of the low energy nuclear transition in ^{229}Th. In addition, we discuss the advantage of studying the transition in highly charged ^{229}Th^{89+} ions and the presence of a Doppler shift while photons interact with the ions in the ESR storage ring. In section 5.2, we then discuss the experimental setup at ESR ion storage ring. Later in section 5.3, the current status of this experiment is summarized.

5.1 Low energy nuclear transition in ^{229}Th

In a neutral ^{229}Th atom, the energy released upon de-excitation of the nucleus can be released via the emission of an electron. This process is called internal conversion and is the dominant decay channel in neutral ^{229}Th[130,160]. The presence of this dominant decay channel, together with the uncertainty of the nuclear transition energy, could be responsible for the inability to locate the transition via fluorescent light emission in previous experiments[161,162,163,164]. The ESR facility at GSI offers a route to reduce or eliminate the internal conversion decay channel by producing highly charged ions such as ^{229}Th^{90+} without electrons and ^{229}Th^{89+} with 1 electron[20]. In this section, we briefly discuss excitation and lifetime of the ^{229}Th^{90+} and ^{229}Th^{89+} ions in the context of the experiment conducted during the beamtime at the ESR ion storage ring.

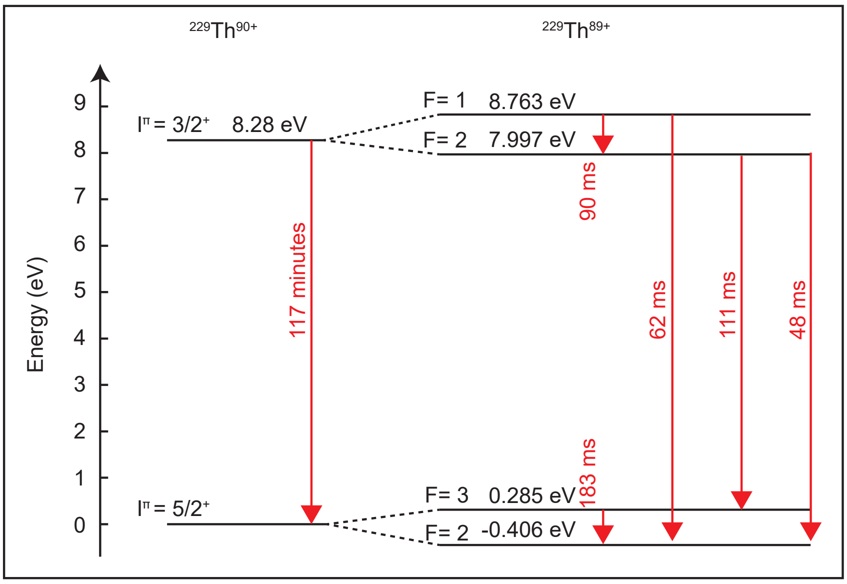

Figure 5.1: Energy level diagram of the nuclear transitions in bare ^{229}Th^{90+} ions (left) and in one electron ^{229}Th^{89+} (right). The presence of one electron introduces hyperfine splittings and nuclear level mixing which cause a splitting of the energy levels. These effects lead to the isomer decaying 5-6 orders of magnitude faster compared to the radiative decay of the neutral ^{229}Th isomer. This figure is produced using calculations from Ref.[165]

5.1.1 Low energy nuclear transition in the highly charged ^{229}Th^{90+} and ^{229}Th^{89+} ions

An advantage of the zero electron ^{229}Th^{90+} ion and the one electron electron ^{229}Th^{89+} ion is that the they can be described very precisely using the theory of quantum electrodynamics[166]. Figure 5.1 shows the energy level diagram of the low energy nuclear transition in the highly charged ^{229}Th^{90+} (left) and ^{229}Th^{89+} ions (right). This figure is based on the theoretical calculations by V. M. Shabaev et al.[165]. The Figure shows that the radiative life time of the ^{229}Th^{89+} ions is reduced to a few hundred milliseconds from $\sim$2 hours. Due to the faster transition rate, the probability for laser excitation and the fluorescence rate are also increased (by an order to 10^6). Therefore, ^{229}Th^{89+} ions are chosen during the beam-time to locate the low lying nuclear transition in ^{229}Th.

5.1.2 Relativistic longitudinal Doppler effect

To excite the nuclear transitions of the ^{229}Th^{89+} atom shown in Figure 5.1, we would need a laser with photon energies in the range from 8.4 eV to 9.2 eV. However, the ion beam is traveling at relativistic velocity in the ESR. When the ion beam interacts with the laser, we need to consider the relativistic longitudinal Doppler effect, which changes the effective photon energy in the reference frame of the ion. The formula for the relativistic longitudinal Doppler shift can be written as[167]:

$$E_{\text{effective}} = E_0 \frac{\sqrt{1+\frac{v}{c}}}{\sqrt{1-\frac{v}{c}}} \tag{5.1}$$

where E_0 is the initial photon energy, c is the velocity of light in vacuum, v is the velocity of the ion and $E_{\text{effective}}$ is the photon energy in the reference frame of the ion.

5.2 Experimental setup

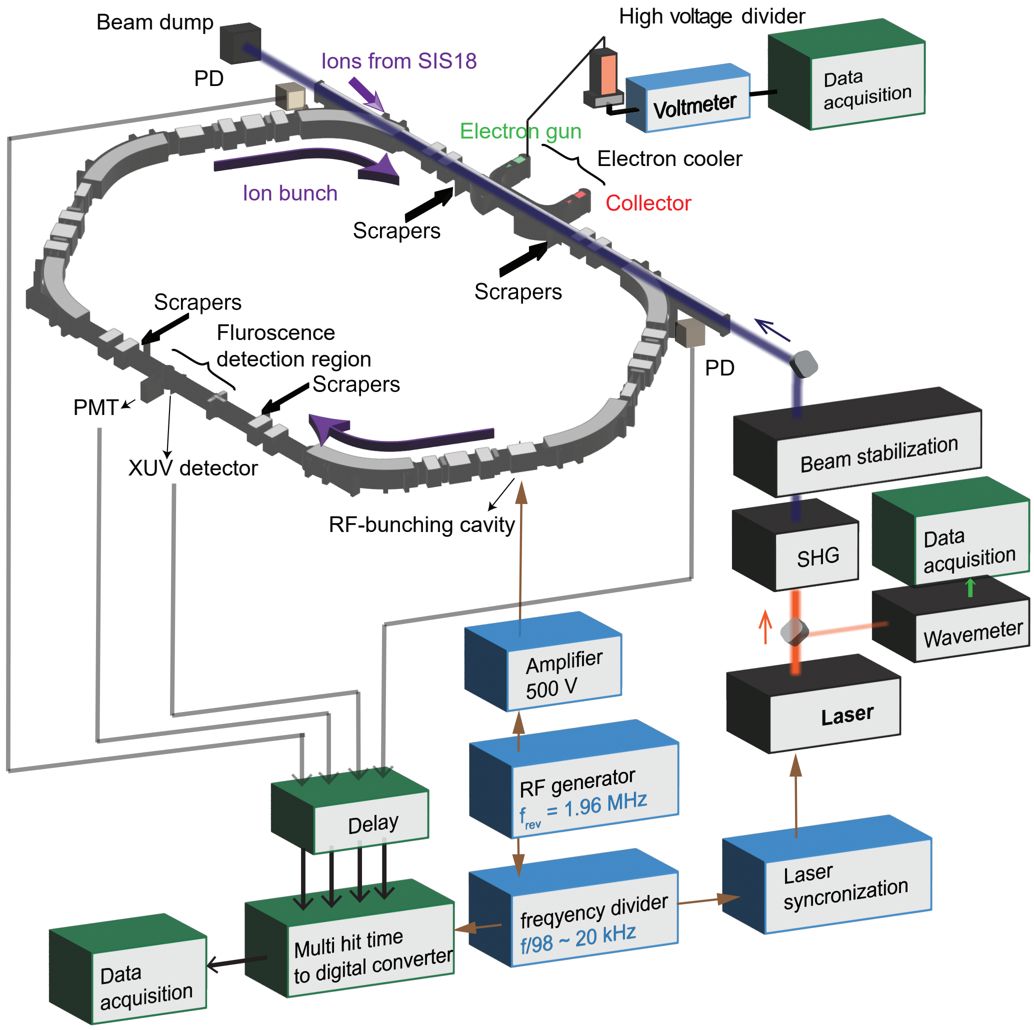

Figure 5.2: Schematic of the experimental setup, which shows the components of the ESR (grey), the electron cooler, the laser and the synchronization electronics: PD, photo-diode. PMT, photo-multiplier tube.

Figure 5.2 shows the schematic of the experimental setup. The ion beams from the heavy ion synchrotron SIS18[168] are injected into the ESR ion storage ring. Then, the $^{229}\text{Th}^{89+}$ ions are selected for storage in the ESR with the help of a Schottkey detector[169] and scrapers. During the beam time of this experiment, the ion count amounted to about 10^4 ions in the ring. The ions and the ultrashort laser pulses interact in the electron cooler while propagating in opposite directions. Later, when the nuclear isomer returns to the ground state, the emitted photons are measured using photo-multiplier tubes designed to detect XUV photons in the range from 6.9 eV (180 nm) to 11.27 eV

(110 nm). Additionally, a photomultiplier tube that can detect IR photons in the range from 0.7 eV (1.7 μm) to 0.9 eV (1.4 μm) is also installed.

The laser used in this experiment is based on a Nd:YAG pump laser, which emits pulses with a pulse energy of $\approx$ 1 J at a repetition rate of 30 Hz. Using SHG, the pulses are converted to 532 nm at a pulse energy of 559 mJ. These pulses are used as pump pulses for a Cobra double dye laser system by Sirah Lasertech, which generates pulses with tunable wavelength in the range from 620 nm to 650 nm. Then, using SHG, the laser is converted to a tunable laser with a wavelength ranging from 310 nm (4 eV) to 325 nm (3.81 eV), a pulse energy of 13.7 mJ and a pulse duration of 3 ns. The wavelength of the laser is measured using a wavemeter. This laser beam is pointing-stabilized with a pair of motorized mirrors and is coupled to the electron cooler of the ESR, where it interacts with the ion beam. It should be noted that the delay between ions and laser pulses is controlled with synchronization electronics. The wavelength of the laser is tuned in increments of 0.002 nm ($\sim$24 meV) during the experiment. In the dissertation by J. Ullmann[170], an in-depth description of the laser is provided.

During the beam-time, the velocity of the ions in the ESR is 70.4 % of the speed of light. Taking into account the relativistic longitudinal Doppler effect and equation (5.1), the photon energy of the ultrashort pulses in the ion frame of reference is tunable in the range from 9.14 eV to 9.55 eV. This range of photon energies spans the range required to excite the ($I^{\pi} = 5/2^{+}$, $F = 2$) $\rightarrow$ ($I^{\pi} = 3/2^{+}$, $F = 1$) transition, as shown in Figure 5.1.

If we consider the third harmonic of the wavelength-tunable frequency comb laser discussed in section 4.3 of this dissertation as the photon source for excitation of the nuclear transition in $^{229}Th^{89+}$ ions, the required velocity of the ions in the ESR can be calculated using equation (5.1), resulting in an ion velocity of 73.1% of the speed of light. While this laser could provide a much higher average power for ^{229}Th excitation, the full potential of a comb laser source can be better used for probing ^{229}Th ions in an ion trap, following better confinement of the isomeric energy.

5.3 Results

During the beam time of this experiment, we did not obtain a discernible signal that confirms the location of the ^{229}Th nuclear transition. The reason for this is the low ion count. This problem will be addressed in future experiments.

CHAPTER 6

SUMMARY AND OUTLOOK

6.1 Path towards locating the low energy nuclear transition of ^{229}Th

At the inception of this dissertation, the low energy nuclear transition of ^{229}Th was best constraint to a wavelength range of 149.7 ± 3.1 nm[32,33]. However recent measurements have reduced this energy uncertainly range to 148.71 ± 0.47 nm[133]. This simplifies the experimental requirements considerably. In order to use the wavelength-tunable laser and enhancement cavity built in section 2.3.2 of this dissertation for spectroscopy of ^{229}Th, several further development steps can be envisioned, as outlined in the following paragraphs.

6.1.1 Linewidth of the laser

The high power frequency comb laser used in this dissertation, has a linewidth in the order of a few kHz. The reason for this is that it is locked to a stable reference CW laser (based on a non-planar ring cavity geometry) with a linewidth of a few kHz. When this laser is used for VUV generation in an enhancement cavity, the linewidth of the resultant VUV laser increases by a factor of 49 (as the linewidth of the laser generated using HHG at the m^{th} harmonic is proportional to m^2[55,35]). While the linewidth of the wavelength-tunable laser developed in this dissertation is sufficient for spectroscopy of neutral ^{229}Th (as its linewidth is broadened due to internal conversion), in order to locate the low energy nuclear transition in ^{229}Th^{q+} ions where the linewidth broadening due to internal conversion is absent[131], we will require a tunable laser with a much reduced linewidth ideally in the mHz range. Therefore, in order to measure the natural linewidth of the low energy ^{229}Th nuclear transition, it is essential to reduce the linewidth of the high power frequency comb laser by choosing a different reference CW laser.

6.1.2 Possible route towards a Watt-class VUV frequency comb laser

In this dissertation, the 515 nm enhancement cavity is designed to support an intra-cavity power enhancement factor of 220. For an input laser power of 31 W at 515 nm (that was generated in section 4.5), this cavity can support a theoretical maximum intra-cavity power of 6.8 kW. Taking into account a third harmonic conversion efficiency of 10^{-4}[59,65], we estimate that the average power of a resultant 170 nm VUV laser generated could reach a maximum value of 0.68 W. By efficient out-coupling using a non-collinear cavity, this would enable us to reach a Watt-class laser in the VUV, which could in-turn significantly contribute to the progress of nonlinear spectroscopy in the VUV.

We note that a key problem on the horizon for the development of a high-power VUV laser with a shorter wavelength enhancement cavity (discussed in section 4.5) is the deterioration of cavity mirrors due to the presence of hydrocarbons when an optical power in the order of a few kW is circulating in the cavity. B. Bernhardt reported such an effect[59]. While ozone has been distributed in our vacuum chamber to prevent the degradation of the cavity mirrors, a verification of this approach is required through experimental data. Furthermore, the absorption of the generated VUV radiation due to presence of oxygen and ozone is a concern and should be investigated.

It should be noted that since the lifetime of the low energy nuclear transition of ^{229}Th is in the order of 1000 s, the probability of transition is very low. Therefore, it is necessary to build a high average power VUV laser, as discussed in section 4.5. Based on recent measurements[133], we note that the cascaded 6th harmonic (2nd harmonic in a crystal followed by the 3rd harmonic in a gas) of the laser with a center wavelength tunable in the range from 889.4 nm to 895.1 nm would be ideal to locate the nuclear transition of ^{229}Th. This wavelength range lies between the two most developed laser amplifier technologies: the Ti:Sapphire and Yb-based amplifiers. Using the serrodyne-frequency-shifting method described in section 4.3, and taking into account state of the art dielectric mirrors, the development of a tunable laser within this wavelength range seems within reach.

If we consider that the high-power frequency comb laser in section 4.2 is wavelength shifted to 892.1 nm with an efficiency of 30 %, and assume an SHG efficiency of 40 %, the average power of laser generated at 446.1 nm would be 9 W. If we also consider a THG in an enhancement cavity with an intra-cavity power enhancement by a factor of 150, and THG conversion efficiency of 10^{-4}, the average power generated at 148.7 nm would correspond to 130 mW. Such a laser would be ideal for spectroscopy of the low energy nuclear transition of neutral ^{229}Th and ^{229}Th^{q+} ions.

6.2 Scientific impact on laser research and development

In this dissertation, we have introduced two new scientific methods. These are: (1) the post-compression of picosecond pulses to a few optical cycles and (2) the tunability of the wavelength of a laser via serrodyne-frequency-shifting. Both methods introduce new perspective on the development of lasers. In this section, we briefly discuss the impact of these methods on laser research and development.

6.2.1 High peak power few cycle lasers

Within the framework of this dissertation, the main focus of the work shifted from the initial few-cycle compression efforts to developments closely related to the frequency comb system described in section 4. Meanwhile, following our initial few-cycle compression works, others have continued pushing the frontiers of MPC technology for few-cycle generation. We here summarize important advancements succeeding the previously described works reported by us in Ref.[129].

In 2020, our experiment[129] compressed a 200 W burst mode ultrashort laser from 1.2 ps to 13 fs. However, the thermal effects in the MPC of the second post compression stage have constraint the energy scalability, limited throughput, and degraded the beam quality in our experiments. Employing a further optimized setup design, Muller et al.[45] were able to circumvent some of the challenges arising in our experiment. Similar to our experimental setup, Muller et al. use a cascaded two-stage MPC-based post-compression scheme. However, they use enhanced silver mirrors on silicon substrates and efficiently mitigate the thermal effects of the MPC via water cooling. In the first compression stage, Müller et al. post-compressed a 388 W ultrashort laser with a pulse duration of 200 fs to 31 fs with a power efficiency of 95%. In the second stage, they reached 6.9 fs with a power efficiency of 82%.

Recently, Rajhans et al.[171] have post-compressed an ultrashort laser that delivers pulses with a duration of 1.2 ps, and a pulse energy of 8.6 mJ at a 1 kHz repletion rate to sub-50 fs with 95 % power efficiency. Afterwards, the pulses have been further compressed to 9.6 fs, with an MPC efficiency of 88% reaching a total compression efficiency 70 %[172]. In this experiment, dispersion-matched dielectric mirrors are used in the second MPC stage. The peak power of this post-compressed laser reaches 0.3 TW. In the near future, the involved colleagues aim to increase the repetition rate to 20 kHz, which would enable few cycle pulses with an output power exceeding 100 W.

6.2.2 Wavelength tunablity of high average/peak power lasers

The serrodyne frequency shifting method offers certain benefits when compared to well-established wavelength tuning methods such as OPCPA, red shift due to Raman scattering, etc. In contrast to an OPCPA[173], the serrodyne frequency shifting method does not have a phase-matching requirement, making it much more flexible for use in different spectral regions. Another advantage is the ability to adjust the wavelength of a laser without mechanical moving parts.

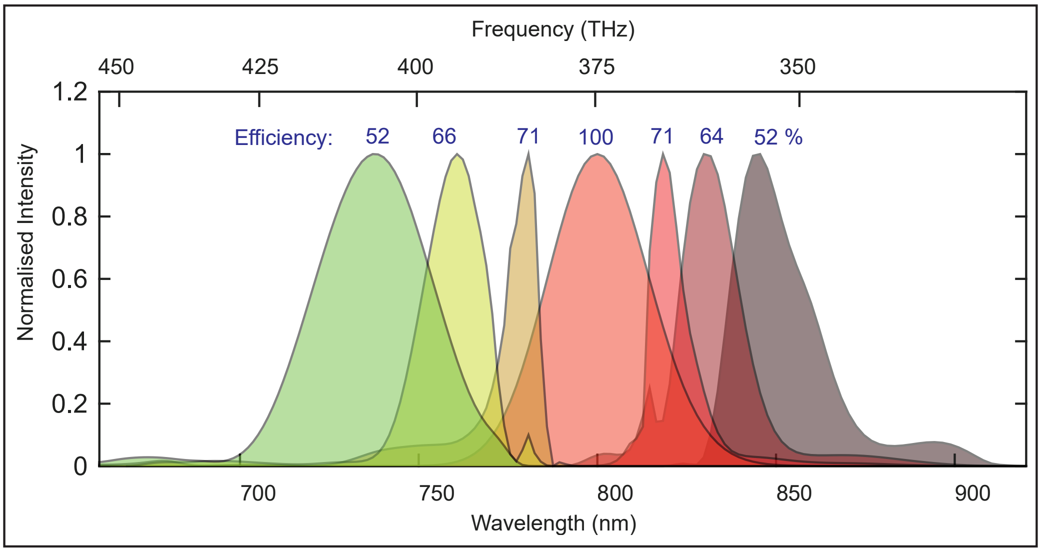

Figure 6.1: Simulation of wavelength shifting of a Fourier-limited input pulse (Gaussian spectrum) of 40 fs, as available from standard Ti:Sapphire laser systems. This figure is reproduced from Ref.[140]

The two main factors that limit the serrodyne-frequency-shifting method are the possible power limitations for shaping the input electric field with a programmable spatial light modulator array, and the limited bandwidth of the dielectric mirrors in the MPC.

The state-of-the-art programmable spatial light modulator arrays available today have limitations as they are not suitable for high-peak power and high-average power femtosecond lasers. In this dissertation, we solve the problem of pulse shaping a high average power femtosecond laser in section 4.2 by placing a programmable spatial light modulator array before the laser is amplified to a high average power. However, depending on how the input laser is designed and built, this may not always be possible. In such a scenario, an alternative solution for pulse shaping of a high pulse energy laser could be direct pulse-shaping with a phase mask[174] or by using a deformable mirror in the CPA compressor[175]. Second, the bandwidth of the dielectric mirrors available today can reach up to a few hundred nanometers. Figure 6.1 shows an example of the simulated wavelength shift of a 40 fs pulse from a Ti:Sapphire laser system (using dispersion-engineered mirrors with a bandwidth of $\approx$ 200 nm), exceeding the wavelength shifting range demonstrated experimentally in this dissertation. The specifications of the employed mirrors and the details of the simulation are discussed in Appendix G.

Since the challenge we are addressing in this dissertation is to develop a suitable laser for spectroscopy of the low energy nuclear transition of ^{229}Th, we have limited the design of the employed dielectric mirrors to accommodate a tuning range of 20 THz. However, it is foreseeable that further optimized dielectric mirrors will enable a much larger range.

APPENDIX A

SPECIFICATIONS OF MIRRORS USED IN THE MPC FOR PULSE POST-COMPRESSION TO FEW OPTICAL CYCLES

The reflectivity and GDD of the mirrors are key factors determining the spectral broadening in an MPC. Hence, the specifications of the mirrors used in the MPCs for ultrashort pulse post-compression, as discussed in section 3.1.2, are presented here.

Figure A.1 (a) shows the reflectivity data provided by the manufacturer for the mirrors in MPC 1 (blue) and MPC 2 (red). Figure A.1 (b) shows the corresponding GDD data.

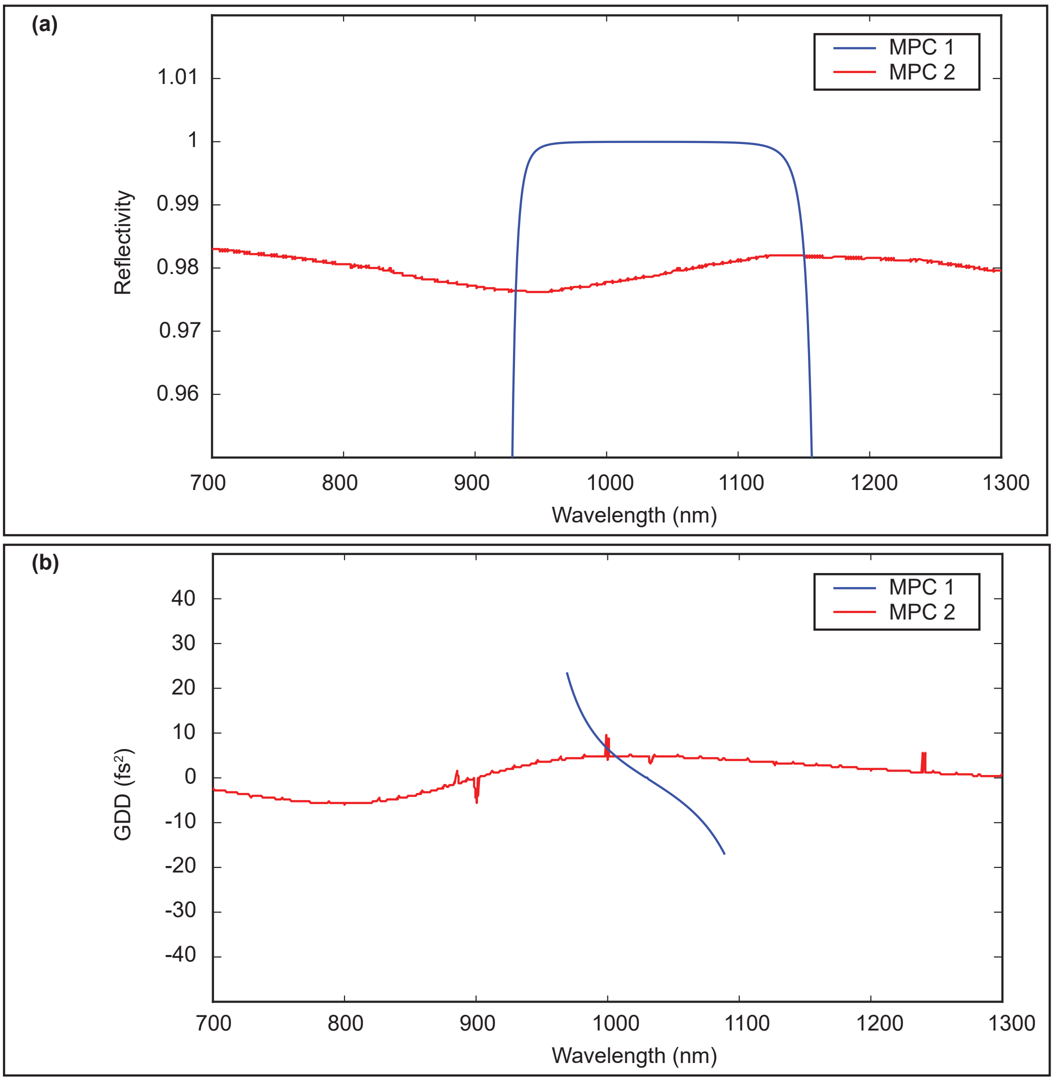

Figure A.1: (a) Reflectivity of the mirrors and (b) GDD of the mirrors used in MPC 1 (blue) and MPC 2 (red) in section 3.1.2.

APPENDIX B

IN-COUPLING OF THE LASER INTO AN MPC

Throughout this dissertation, the laser beam is in-coupled into an MPC using a rectangular pick-off mirror, that is glued to a stainless steel plate with an epoxy and then mounted on a mirror mount, as shown in a photograph in Figure B.1. The width of the pick-off mirror is ≈ 9 mm for the in-coupler in the MPC-1 discussed in section 3.1 and ≈ 4 mm for the in-coupler in the MPC discussed in section 3.2.

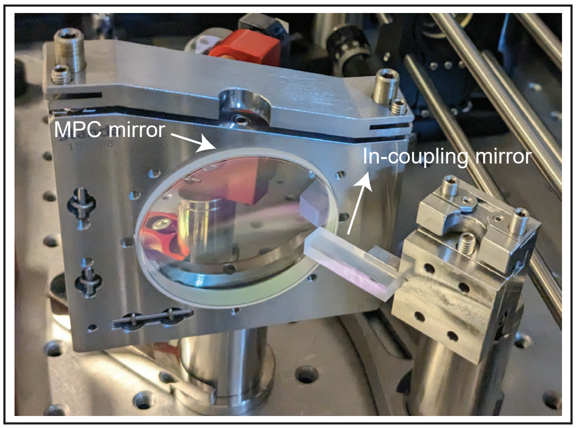

Figure B.1: Photograph showing the relative position of the in-coupling mirror and the MPC mirror in a typical MPC developed during this dissertation.

The main reason that the bulk MPC in sections 3.2 and 4.3 is not very efficient (82 %) is that during each round trip, the pulse experiences reflection losses at the air / dielectric medium interfaces of the 5 AR coated optics used to provide the nonlinear medium. In addition, AR-coated optics have a limited bandwidth and a lower damage threshold than uncoated optics. In order to solve this problem with the lower transmission efficiency of the MPC and also the associated problems with AR coated optics, we can use the fact that an MPC can support several distinct beam patterns, such as a line pattern (as shown in Figure B.2 (a)), or a circular Herriot pattern (as shown in Figure B.2 (b)) etc. The advantage of the line pattern is that all the beams are in the same geometric plane. This makes it possible to use an optic at a Brewster angle (to act as a nonlinear medium) and thus minimize the losses due to Frenel reflections. Although a line pattern in a bulk-based MPC can offer a high efficiency due to low Fresnel reflection losses at the Brewster plate, the number of spots that can be accommodated on mirrors with 2-inch diameter (without clipping the beam during out-coupling) is limited, which in turn limits the total B-integral that could be accumulated. In view of the time constraints, we choose a Herriot pattern with 32 round trips for the bulk-MPC in sections 3.2 and 4.3 to achieve a large spectral broadening factor and build a widely tunable-wavelength laser. However, if mirrors with larger transverse dimensions are available, it is more advantageous to switch to a line pattern MPC to achieve a higher transmission efficiency of the MPC. Figure B.2 (b) displays a photograph of an MPC with a Herriot pattern that supports 15 round trips. A photograph of an MPC consisting of 2 focusing mirrors with radii of curvature of 100 mm and a fused silica Brewster plate with a thickness of 6.35 mm is shown in Figure B.2 (c).

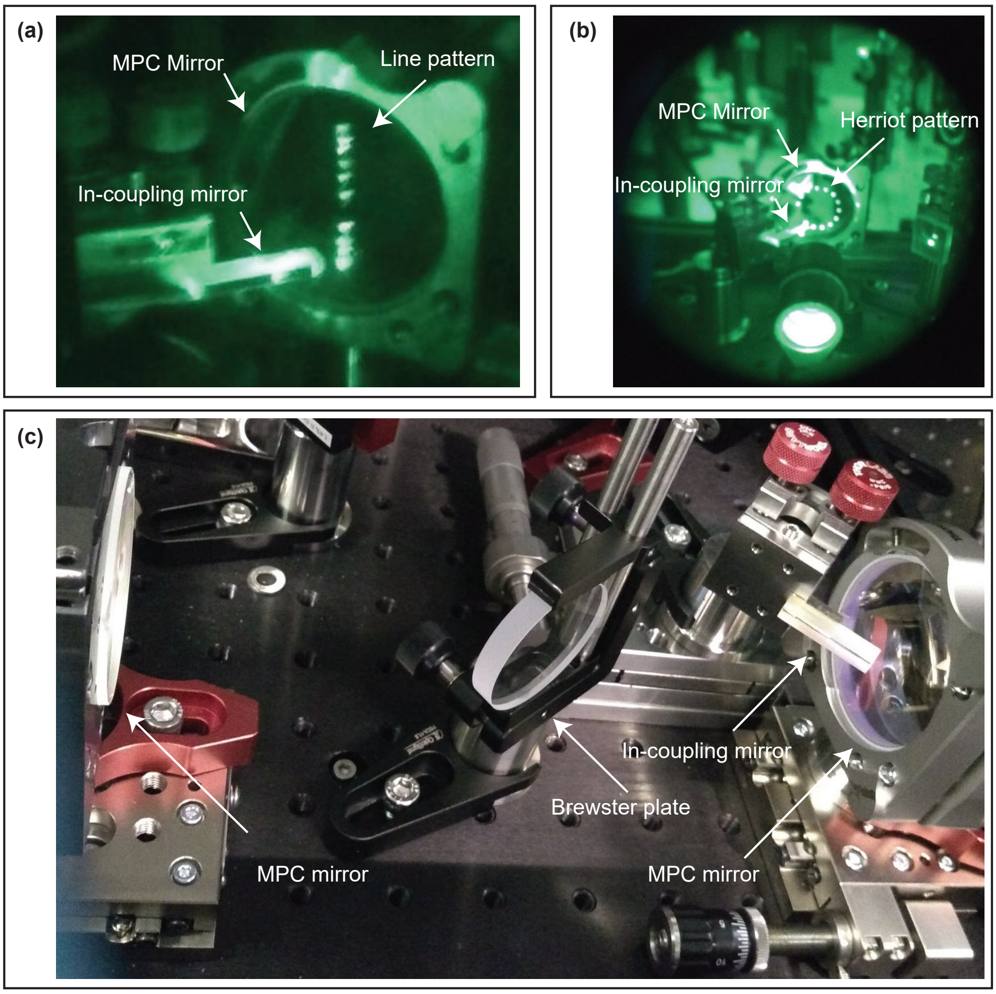

Figure B.2: Photographs of a nonlinear MPC with (a) a line pattern and (b) a circular Herriot pattern viewed through a handheld infrared viewer. (c) Photograph of a line pattern nonlinear-MPC setup containing a Brewster plate.

APPENDIX C

THE INFLUENCE OF PULSE SHAPER DISPERSION ON THE LASER SPECTRUM

To test the impact of phase shaping on the optical spectrum, we scan a range of GDD and TOD values and measure the spectrum directly after the pulse shaper, as shown in Figure C.1.

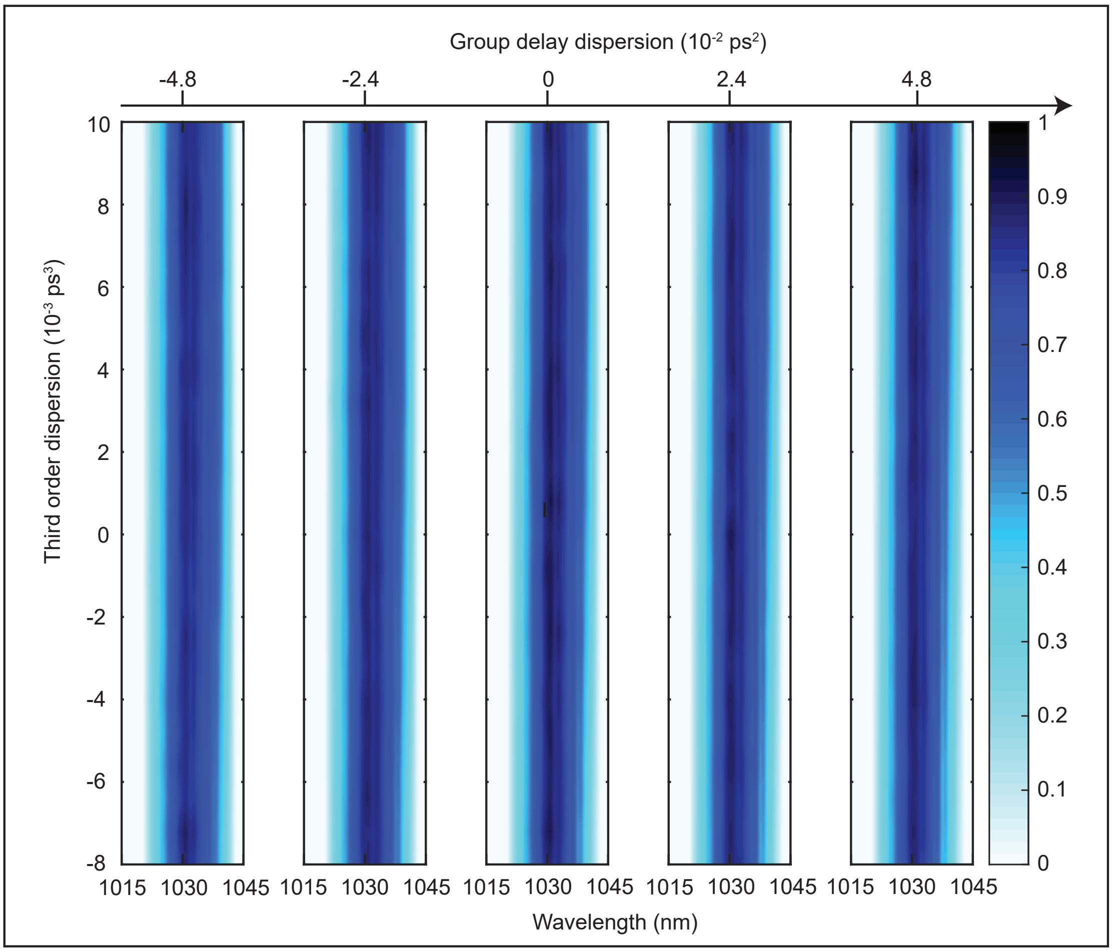

Figure C.1: The measured spectrum directly after the pulse shaper for a range of GDD and TOD values.

APPENDIX D

SIDE-BAND GENERATION FOR THE PDH LOCK

To choose a frequency for the generation of sidebands in the laser oscillator that are essential for a PDH locking scheme, we scan the resonances of the PZT in the NALM oscillator of the laser with a signal from a function generator with an amplitude of 10 V peak to peak, and observe the RF spectrum of the laser on a photodiode. Figure D.1 shows the RF spectrum when signals with a frequency of 900 kHz, 1.08 MHz and 3 MHz are applied. The amplitude of all signals is 10 V peak to peak. While performing the PDH lock in the enhancement cavity, we choose to generate sidebands at a frequency of 900 kHz, as the signal to noise ratio of the peak at 900 kHz is the largest.

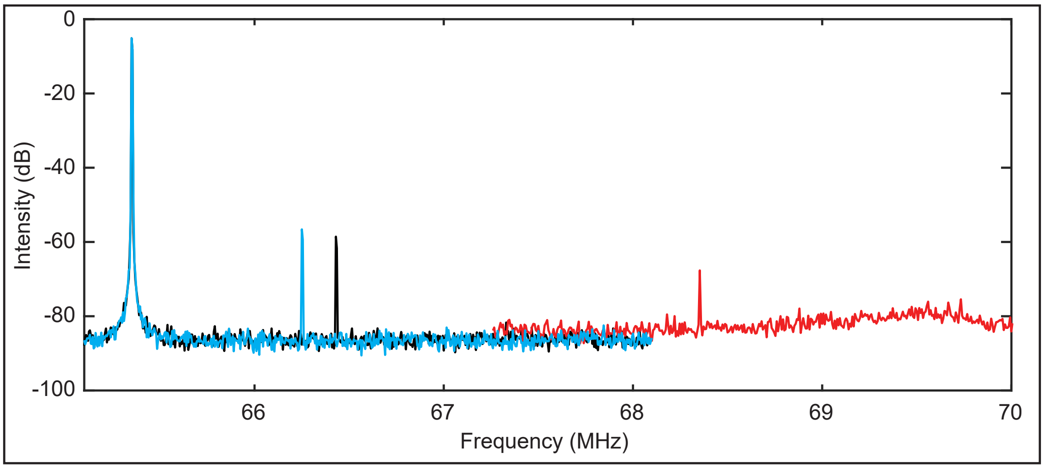

Figure D.1: The RF spectrum of the laser when the PZT in the laser oscillator is driven with a sine waveform at frequencies of 900 kHz (blue), 1.08 MHz (black) and 3 MHz (red). As seen in the RF spectrum, the sidebands are located at a 900 kHz (blue), 1.08 MHz (black), and 3 MHz (red) distance to the repetition rate frequency peak at 65.3 MHz.

APPENDIX E

CHARACTERISTICS OF THE PZT MOUNT OF THE ENHANCEMENT CAVITY

One of the most important elements of an optical enhancement cavity is the high reflectivity cavity mirror attached to a PZT, which is necessary to achieve a stable lock. A key factor that affects the stability of an optical lock is the bandwidth of the final mirror-assembly.[138] Therefore, we take special care when designing the mount for this particular mirror component. Figures E.1 (a) and b) show the CAD diagram of the bullet-shaped mount and its holder. The mount is made from Copper, and its inner part is filled with Lead in order to reduce or eliminate the resonances of the final mirror structure. As shown in Figure E.1 (c), the mount is assembled with the PZT and the cavity mirror glued together with a vacuum-compatible epoxy. The mount is glued to the holder with the same vacuum-compatible epoxy as shown in Figure E.1 (d). The complete mirror-assembly as it appears when placed in the cavity is shown in Figure E.1 (e).

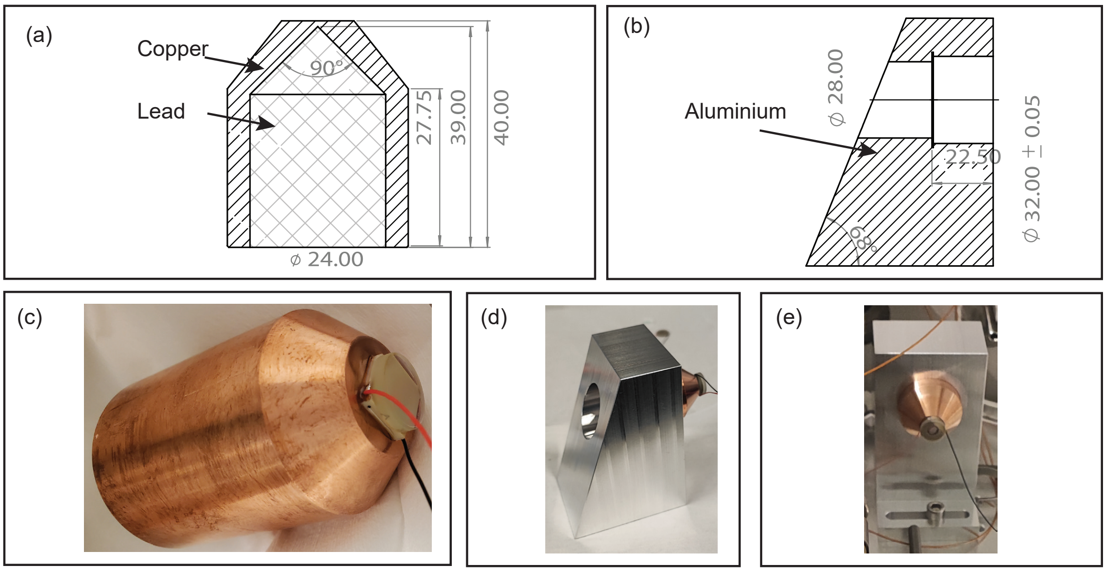

Figure E.1: (a) A schematic of the fast PZT mount. (b) A schematic of the mount holder. The units of all the dimensions specified in (a) and (b) are in mm. (c) Picture of the cavity mirror and the PZT glued to the mount with a vacuum-compatible epoxy. (d) The mount securely glued to the holder. (e) Picture of the complete mirror assembly, as it appears when placed in the cavity

We use a fiber interferometer to measure amplitude and phase noise of the assembled mirror. By conducting this analysis, we can develop a greater understanding of the frequency dependent resonance properties of the mirror-assembly. Figure E.2 (a) shows the schematic of the experimental setup. The interferometer is made with a 50/50 fiber splitter. Two of the arms of the interferometer are used to place the assembled mirror and a reference mirror on one side. One of the arms is used to couple in an external, stable CW laser at 1064 nm. We use an isolator with an attenuation of 35 dB to stop back propagation of the laser into the CW laser source. The fourth arm of the interferometer is used to detect the laser on a photodiode. The signal from the photodiode is sent to a vector analyzer. The vector analyzer emits signals of different frequencies, which are then sent to the PZT. It is important to consider that the signal from the photodiode is also used to stabilize the movement of the reference mirror to a single laser fringe. The signal from the photodiode is filtered using a programmable low pass filter set to a frequency cut off of 10 Hz. The filtered signal is then sent to a fast PZT in the mount of the reference mirror. This is done to prevent any fluctuations in the laboratory from affecting the results. Figure E.2 (b) shows the measured amplitude noise (top) and phase noise (bottom) of the mirror-assembly.

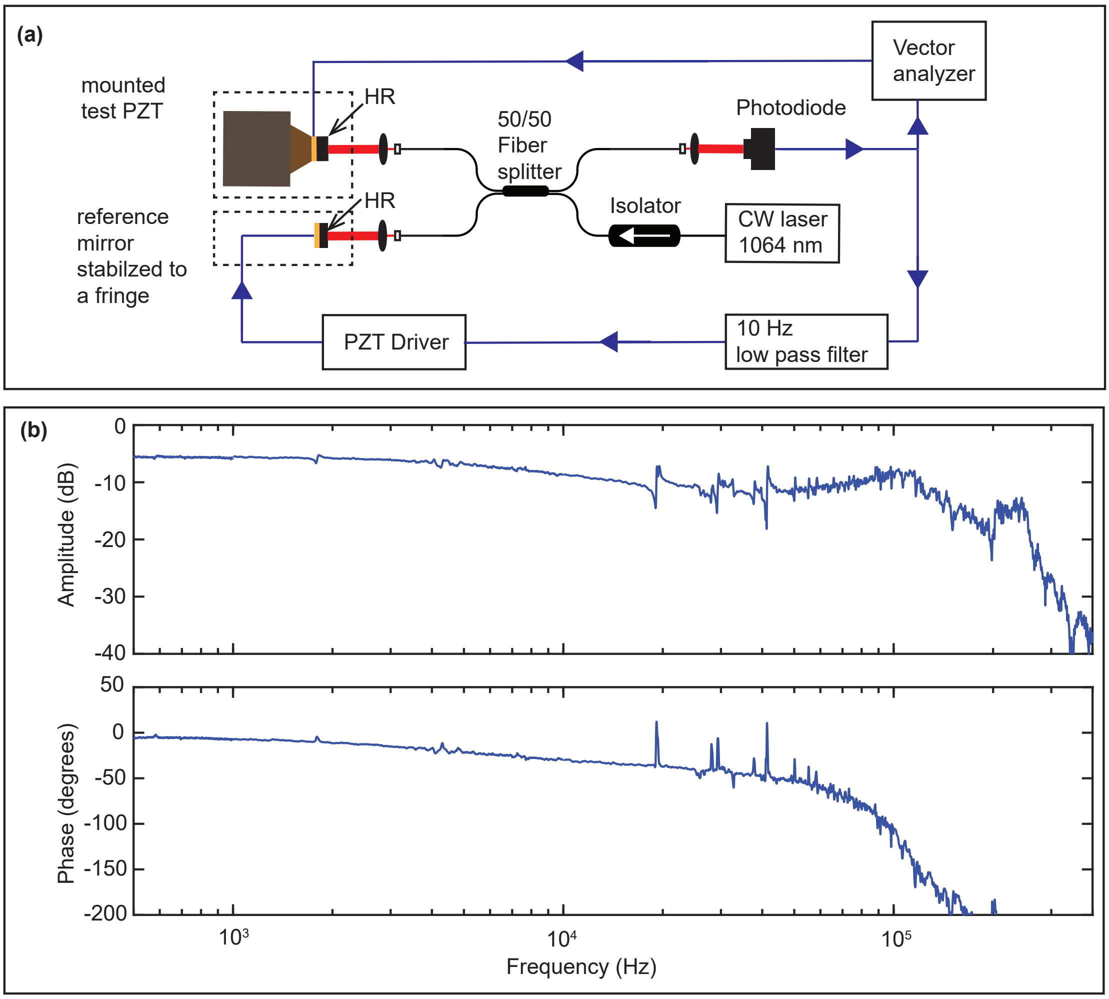

Figure E.2: (a) Schematic of the experiment setup, which measures the amplitude and phase noise of an assembled mirror. (b) The amplitude noise (top) and phase noise (bottom) of the mirror-assembly.

APPENDIX F

CHARACTERISTICS OF THE MIRRORS USED IN THE ENHANCEMENT CAVITIES AT 1030 NM AND 515 NM

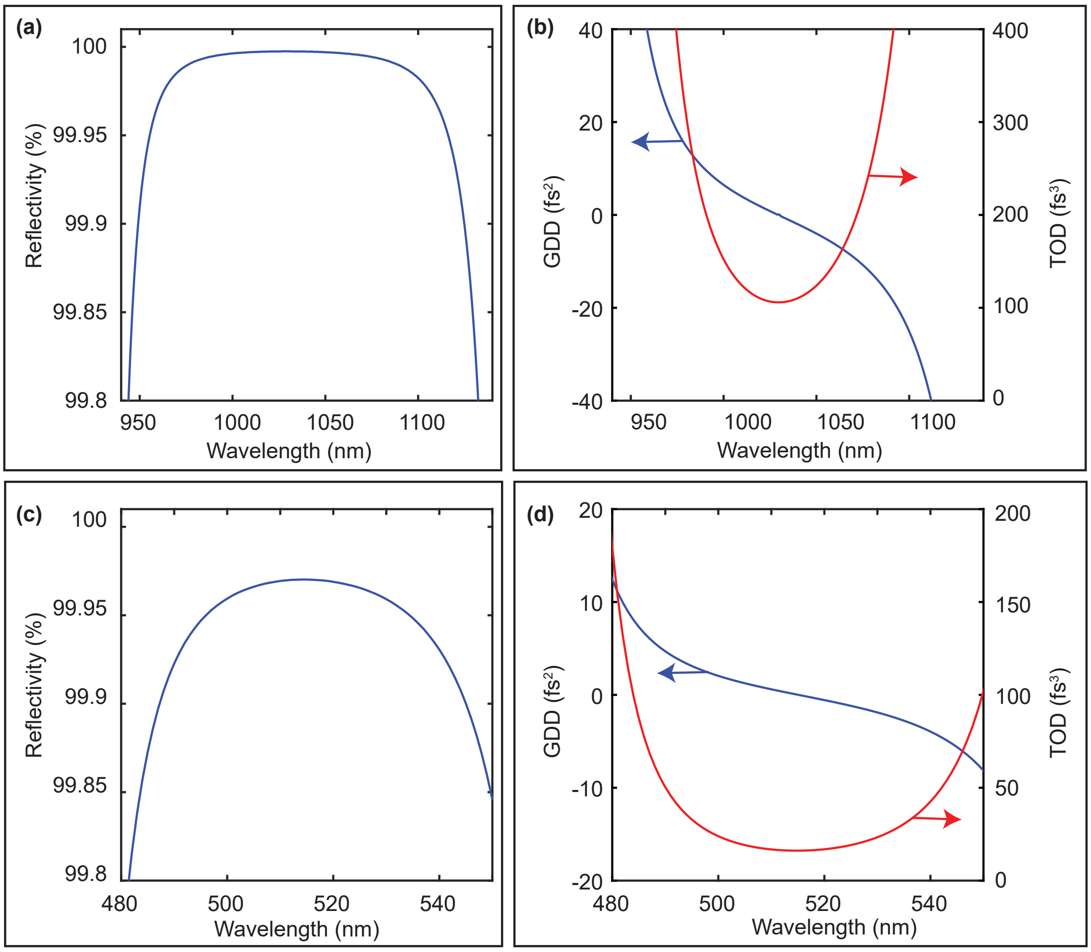

Figure F.1: (a) the reflectivity, (c) GDD (left) and TOD (right) of the mirrors used in enhancement cavity at 1030 nm discussed in section 4.4. (b) the Reflectivity, (d) GDD (left) and TOD (right) of the mirrors used in enhancement cavity at 515 nm discussed in section 4.5.

The reflectivity, GDD and TOD of the low loss cavity are key factors determining the characteristics of the enhancement cavities at 1030 nm and 515 nm. The specifications of the mirrors used in the enhancement cavities in sections 4.4 and 4.5 are presented here.

The reflectivity data provided by the manufacturer are shown in Figures F.1 (a) and (c), respectively. The corresponding GDD and TOD are shown in Figures F.1 (b) and (d), respectively.

APPENDIX G

SERRODYNE-SHIFT USING BROAD-BANDWIDTH DIELECTRIC MIRRORS

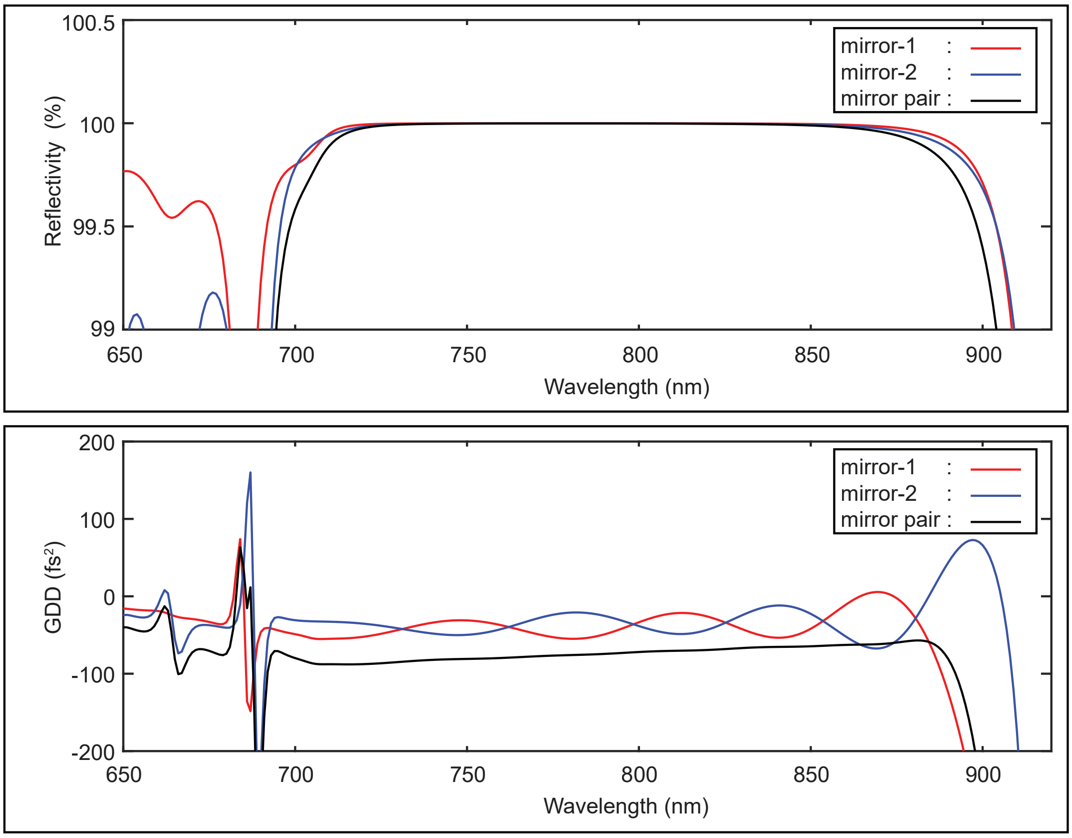

Figure G.1: (a) The reflectivity and (b) GDD of the mirrors used in numerical simulation of the serrodyne-frequency-shift which employs dielectric mirrors with broad-bandwidth.

To show that the mirrors needed for wavelength-tuning over a broad bandwidth using the serrodyne-frequency-shifting method are available considering state-of-the-art mirror technology, we select commercially available dielectric mirror pairs with a center wavelength of 800 nm. The mirror pair provides dispersion properties that are matched to compensate for 2 mm fused silica in a wavelength range of 710 nm to 890 nm. Figure G.1 shows the reflectivity and GDD of the mirrors.

An MPC consisting of four mirrors is considered to provide two mirror reflections between successive passes through the nonlinear medium (fused silica). In our simulations, we launch a pulse with a spectral phase, representing a good guess for a temporally asymmetric pulse form that approaches a saw-tooth shape (transform-limited pulse duration: 40 fs, Gaussian spectral amplitude) into the MPC. The accumulated nonlinear phase per pass ($\approx$1.7 radians) is within a range that enables MPC spectral broadening based on multiple plates, while supporting excellent spatial beam quality[95]. The number of round trips in the MPC is 40. The simulation is performed by solving the forward Maxwell equation[56], while using a numerical library called Optax[176,177], which supports automatic differentiation and optimization. Optax is a library developed for the training of neural networks. In the context of our simulations, Optax helps to optimize the phase required for spectral shifting iteratively. This efficiently enables optimization of a relatively large parameter space. In this numerical simulation, we only used phase shaping, amplitude shaping was not employed. Figure 6.1 shows the simulation results.

REFERENCES

[1] T. H. Maiman. Stimulated optical radiation in ruby. *Nature*, 187(4736):493–494, aug 1960.

[2] F. P. Schafer. *Topics in applied physics*. Springer, 1973.

[3] J. J. Snyder. Laser wavelength meters. *Laser Focus(Includes Electro-Optics)*, 18(5):55–61, 1982.

[4] Mark B. Morris, Thomas J. McIlrath, and James J. Snyder. Fizeau wavemeter for pulsed laser wavelength measurement. *Applied Optics*, 23(21):3862–3868, 1984.

[5] Jun Ishikawa, Nobuhiko Ito, and Keiichi Tanaka. Accurate wavelength meter for CW lasers. *Applied optics*, 25(5):639–643, 1986.

[6] R. Castell, W. Demtröder, A. Fischer, R. Kullmer, H. Weickenmeier, and K. Wickert. The accuracy of laser wavelength meters. *Applied Physics B*, 38:1–10, 1985.

[7] Christopher Reiser. Modern pulsed wavemeters. In *Pulse Single-Frequency Lasers: Technology and Applications*, volume 912, pages 214–225. SPIE, 1988.

[8] Laurent Nahon, Christian Alcaraz, Jean-Louis Marlats, Bruno Lagarde, François Polack, Roland Thissen, Didier Lepere, and Kenji Ito. Very high spectral resolution obtained with su5: A vacuum ultraviolet undulator-based beamline at super-aco. *Review of Scientific Instruments*, 72(2):1320–1329, 2001.

[9] H. Schnatz, B. Lipphardt, J. Helmcke, F. Riehle, and G. Zinner. First phase-coherent frequency measurement of visible radiation. *Physical Review Letters*, 76(1):18, 1996.

[10] David J. Jones, Scott A. Diddams, Jinendra K. Ranka, Andrew Stentz, Robert S. Windeler, John L. Hall, and Steven T. Cundiff. Carrier-envelope phase control of femtosecond mode-locked lasers and direct optical frequency synthesis. *Science*, 288(5466):635–639, 2000.

[11] T. M. Fortier, P. A. Roos, D. J. Jones, Steven T. Cundiff, R. D. R. Bhat, and John E. Sipe. Carrier-envelope phase-controlled quantum interference of injected photocurrents in semiconductors. *Physical review letters*, 92(14):147403, 2004.

[12] M. Niering, R. Holzwarth, J. Reichert, P. Pokasov, T. Udem, M. Weitz, T. W. Hänsch, P. Lemonde, G. Santarelli, M. Abgrall, P. Laurent, C. Salomon, and A. Clairon. Measurement of the hydrogen 1S - 2S transition frequency by phase coherent comparison with a microwave cesium fountain clock. *Physical Review Letters*, 84(24):5496, 2000.

[13] Tara Fortier and Esther Baumann. 20 years of developments in optical frequency comb technology and applications. *Communications Physics*, 2(1):153, 2019.

[14] Tara M. Fortier, Matthew S. Kirchner, F. Quinlan, J. C. B. J. Taylor, J. C. Bergquist, T. Rosenband, N. Lemke, A. Ludlow, Y. Jiang, C. W. Oates, and S. A. Diddams. Generation of ultrastable microwaves via optical frequency division. *Nature Photonics*, 5(7):425–429, 2011.

[15] Alexey Grinin. *Two-photon frequency comb spectroscopy of atomic hydrogen*. PhD thesis, Ludwig-Maximilians-Universität München, 2020.

[16] Boulder Atomic Clock Optical Network BACON Collaboration. Frequency ratio measurements at 18-digit accuracy using an optical clock network. *Nature*, 591(7851):564–569, 2021.

[17] Ian Coddington, Nathan Newbury, and William Swann. Dual-comb spectroscopy. *Optica*, 3(4):414–426, 2016.

[18] Morton A. Levine, R. E. Marrs, J. R. Henderson, D. A. Knapp, and Marilyn B. Schneider. The electron beam ion trap: A new instrument for atomic physics measurements. *Physica Scripta*, 1988(T22):157, 1988.

[19] Maria Schwarz, O. O. Versolato, Alexander Windberger, F. R. Brunner, Tim Ballance, S. N. Eberle, Joachim Ullrich, Piet O. Schmidt, Anders Kragh Hansen, Alexander David Gingell, et al. Cryogenic linear paul trap for cold highly charged ion experiments. *Review of Scientific Instruments*, 83(8), 2012.

[20] Bernhard Franzke. The heavy ion storage and cooler ring project ESR at GSI. *Nuclear Instruments and Methods in Physics Research Section B: Beam Interactions with Materials and Atoms*, 24:18–25, 1987.

[21] R. A. Maier. Cooler synchrotron COSY. *Nuclear Physics News*, 7(4):5–13, 1997.

[22] Jia-Wen Xia, Wen-Long Zhan, Bao-Wen Wei, Y. J. Yuan, M. T. Song, W. Z. Zhang, X. D. Yang, P. Yuan, D. Q. Gao, H. W. Zhao, X. T. Yang, G. Q. Xiao, K. T. Man, J. R. Dang, X. H. Cai, Y. F. Wang, J. Y. Tang, W. M. Qiao, Y. N. Rao, Y. He, L. Z. Mao, and Z. Z. Zhou. The heavy ion cooler-storage-ring project (HIRFL-CSR) at Lanzhou. *Nuclear Instruments and Methods in Physics Research Section A: Accelerators, Spectrometers, Detectors and Associated Equipment*, 488(1-2):11–25, 2002.

[23] Oldřich Novotnỳ, Patrick Wilhelm, Daniel Paul, Abel Kalosi, Sunny Saurabh, Arno Becker, Klaus Blaum, Sebastian George, Jürgen Göck, Manfred Grieser, Florian Grussie, Robert von Hahn, Claude Krantz, Holger Kreckel, Christian Meyer, Preeti M. Mishra, Damian Muell, Felix Nuesslein, Dmitry A. Orlov, Marius Rimmler, Viviane C. Schmidt, Andrey Shornikov, Aleksandr S. Terekhov, Stephen Vogel, Daniel Zajfman, and Andreas Wolf. Quantum-state–selective electron recombination studies suggest enhanced abundance of primordial HeH+. *Science*, 365(6454):676–679, 2019.

[24] Markus Steck and Yuri A. Litvinov. Heavy-ion storage rings and their use in precision experiments with highly charged ions. *Progress in Particle and Nuclear Physics*, 115:103811, 2020.

[25] Bernhard W. Adams, Christian Buth, Stefano M. Cavaletto, Jörg Evers, Zoltán Harman, Christoph H. Keitel, Adriana Pálffy, Antonio Picón, Ralf Röhlsberger, Yuri Rostovtsev, and Kenji Tamasaku. X-ray quantum optics. *Journal of modern optics*, 60(1):2–21, 2013.

[26] Jean-Philippe Karr. Hyperfine puzzle? *Nature Physics*, 13(6):533–534, 2017.

[27] G. W. F. Drake. Progress in helium fine-structure calculations and the fine-structure constant. *Canadian journal of physics*, 80(11):1195–1212, 2002.

[28] G. W. F. Drake and Z.-C. Yan. High-precision spectroscopy as a test of quantum electrodynamics in light atomic systems. *Canadian Journal of Physics*, 86(1):45–54, 2008.

[29] Paul Indelicato, O. Gorveix, and Jean-Paul Desclaux. Multiconfigurational Dirac-Fock studies of two-electron ions. II. radiative corrections and comparison with experiment. *Journal of Physics B: Atomic and Molecular Physics*, 20(4):651, 1987.

[30] M. G. Kozlov, M. S. Safronova, J. R. Crespo López-Urrutia, and P. O. Schmidt. Highly charged ions: Optical clocks and applications in fundamental physics. *Reviews of Modern Physics*, 90(4):045005, 2018.

[31] Ekkehard Peik, Thorsten Schumm, M.S. Safronova, Adriana Palffy, Johannes Weitenberg, and Peter G. Thirolf. Nuclear clocks for testing fundamental physics. *Quantum Science and Technology*, 6(3):034002, 2021.

[32] Benedict Seiferle, Lars von der Wense, Pavlo V. Bilous, Ines Amersdorffer, Christoph Lemell, Florian Libisch, Simon Stellmer, Thorsten Schumm, Christoph E. Düllmann, Adriana Pálffy, and Peter G. Thirolf. Energy of the ^{229}Th nuclear clock transition. *Nature*, 573(7773):243–246, 2019.

[33] Lars von der Wense and Chuankun Zhang. Concepts for direct frequency-comb spectroscopy of ^{229m}Th and an internal-conversion-based solid-state nuclear clock. *The European Physical Journal D*, 74:1–17, 2020.

[34] Yuri Shvyd'ko, Ralf Röhlsberger, Olga Kocharovskaya, Jörg Evers, Gianluca Aldo Geloni, Peifan Liu, Deming Shu, Antonino Miceli, Brandon Stone, Willi Hippler, Berit Marx-Glowna, Ingo Uschmann, Robert Loetzsch, Olaf Leupold, Hans-Christian Wille, Ilya Sergeev, Miriam Gerharz, Xiwen Zhang, Christian Grech, Marc Guetg, Vitali Kocharyan, Naresh Kujala, Shan Liu, Weilun Qin, Alexey Zozulya, Jörg Hallmann, Ulrike Boesenberg, Wonhyuk Jo, Johannes Möller, Angel Rodriguez-Fernandez, Mohamed Youssef, Anders Madsen, and Tomasz Kolodziej. Resonant X-ray excitation of the nuclear clock isomer ^{45}Sc. *Nature*, pages 1–5, 2023.

[35] Craig Benko. *Extreme ultraviolet frequency combs for precision measurement and strong-field physics.* PhD thesis, University of Colorado at Boulder, 2016.

[36] John M. J. Madey. Stimulated emission of bremsstrahlung in a periodic magnetic field. *Journal of Applied Physics*, 42(5):1906–1913, 1971.

[37] S. W. Epp, J. R. Crespo López-Urrutia, M. C. Simon, T Baumann, G. Brenner, R. Ginzel, N. Guerassimova, V. Mäckel, P. H. Mokler, B. L. Schmitt, et al. X-ray laser spectroscopy of highly charged ions at FLASH. *Journal of Physics B: Atomic, Molecular and Optical Physics*, 43(19):194008, 2010.

[38] Bernhard Adams, Gabriel Aeppli, Thomas Allison, Alfred Q. R. Baron, Phillip Bucksbaum, Aleksandr I. Chumakov, Christopher Corder, Stephen P. Cramer, Serena DeBeer, Yuntao Ding, Jörg Evers, Josef Frisch, Matthias Fuchs, Gerhard Grübel, Jerome B. Hastings, Christoph M. Heyl, Leo Holberg, Zhirong Huang, Tetsuya Ishikawa, Andreas Kaldun, Kwang-Je Kim, Tomasz Kolodziej, Jacek Krzywinski, Zheng Li, Wen-Te Liao, Ryan Lindberg, Anders Madsen, Timothy Maxwell, Giulio Monaco, Keith Nelson, Adriana Palffy, Gil Porat, Weilun Qin, Tor Raubenheimer, David A. Reis, Ralf Röhlsberger, Robin Santra, Robert Schoenlein, Volker Schünemann, Oleg Shpyrko, Yuri Shvyd'ko, Sharon Shwartz, Andrej Singer, Sunil K. Sinha, Mark Sutton, Kenji Tamasaku, Hans-Christian Wille, Makina Yabashi, Jun Ye, and Diling Zhu. Scientific opportunities with an X-ray free-electron laser oscillator. *arXiv preprint arXiv:1903.09317*, 2019.

[39] P. A. Franken, Alan E. Hill, C. W. el. Peters, and Gabriel Weinreich. Generation of optical harmonics. *Physical Review Letters*, 7(4):118, 1961.

[40] A. McPherson, G. Gibson, H. Jara, U. Johann, Ting S. Luk, I. A. McIntyre, Keith Boyer, and Charles K. Rhodes. Studies of multiphoton production of vacuum-ultraviolet radiation in the rare gases. *JOSA B*, 4(4):595–601, 1987.

[41] M. Ferray, Anne L'Huillier, X. F. Li, L. A. Lompre, G. Mainfray, and C. Manus. Multiple-harmonic conversion of 1064 nm radiation in rare gases. *Journal of Physics B: Atomic, Molecular and Optical Physics*, 21(3):L31, 1988.

[42] Jozsef Seres, E. Seres, Aart J. Verhoef, G. Tempea, Ch. Streli, P. Wobrauschek, V. Yakovlev, Armin Scrinzi, Ch. Spielmann, and Ferenc Krausz. Source of coherent kiloelectronvolt x-rays. *Nature*, 433(7026):596–596, 2005.

[43] Tenio Popmintchev, Ming-Chang Chen, Dimitar Popmintchev, Paul Arpin, Susannah Brown, Skirmantas Ališauskas, Giedrius Andriukaitis, Tadas Balčiunas, Oliver D. Mücke, Audrius Pugzlys, Andrius Baltuška, Bonggu Shim, Samuel E. Schrauth, Alexander Gaeta, Carlos Hernández-García, Luis Plaja, Andreas Becker, Agnieszka Jaron-Becker, Margaret M. Murnane, and Henry C. Kapteyn. Bright coherent ultrahigh harmonics in the keV X-ray regime from mid-infrared femtosecond lasers. *science*, 336(6086):1287–1291, 2012.

[44] Thomas Nubbemeyer, Martin Kaumanns, Moritz Ueffing, Martin Gorjan, Ayman Alismail, Hanieh Fattahi, Jonathan Brons, Oleg Pronin, Helena G. Barros, Zsuzsanna Major, Thomas Metzger, Dirk Sutter, and Ferenc Krausz. 1 kW, 200 mJ picosecond thin-disk laser system. *Optics letters*, 42(7):1381–1384, 2017.

[45] Michael Müller, Arno Klenke, Albrecht Steinkopff, Henning Stark, Andreas Tünnermann, and Jens Limpert. 3.5 kW coherently combined ultrafast fiber laser. *Optics letters*, 43(24):6037–6040, 2018.

[46] Giulio Cerullo and Sandro De Silvestri. Ultrafast optical parametric amplifiers. *Review of scientific instruments*, 74(1):1–18, 2003.

[47] Cristian Manzoni and Giulio Cerullo. Design criteria for ultrafast optical parametric amplifiers. *Journal of Optics*, 18(10):103501, 2016.

[48] Fetah Benabid, Jonathan C Knight, G Antonopoulos, and P St J Russell. Stimulated raman scattering in hydrogen-filled hollow-core photonic crystal fiber. *Science*, 298(5592):399–402, 2002.

[49] M Ziemienczuk, AM Walser, A Abdolvand, and P St J Russell. Intermodal stimulated raman scattering in hydrogen-filled hollow-core photonic crystal fiber. *JOSA B*, 29(7):1563–1568, 2012.

[50] I. Fischer and Thomas Schultz. Generation of tunable visible and near-IR light from 2.5 ps, high-power Ti: Sapphire pulses by raman shifting in hydrogen. *Applied Physics B*, 64(1):15–20, 1996.

[51] A. V. Konyashchenko, L. L. Losev, and S. Yu Tenyakov. Raman frequency shifter for laser pulses shorter than 100 fs. *Optics Express*, 15(19):11855–11859, 2007.

[52] A. V. Konyashchenko, L. L. Losev, V. S. Pazyuk, and S. Yu Tenyakov. Frequency shifting of sub-100 fs laser pulses by stimulated raman scattering in a capillary filled with pressurized gas. *Applied Physics B*, 93:455–461, 2008.

[53] Carlo Vicario, Mostafa Shalaby, Aleksandr Konyashchenko, Leonid Losev, and Christoph P. Hauri. High-power femtosecond raman frequency shifter. *Optics letters*, 41(20):4719–4722, 2016.

[54] A. V. Konyashchenko, L. L. Losev, and V. S. Pazyuk. Femtosecond raman frequency shifter–pulse compressor. *Optics Letters*, 44(7):1646–1649, 2019.

[55] Craig Benko, Thomas K. Allison, Arman Cingöz, Linqiang Hua, François Labaye, Dylan C. Yost, and Jun Ye. Extreme ultraviolet radiation with coherence time greater than 1 s. *Nature Photonics*, 8(7):530–536, 2014.

[56] A. Couairon, E. Brambilla, T. Corti, D. Majus, O. de J. Ramírez-Góngora, and M. Kolesik. Practitioner's guide to laser pulse propagation models and simulation: Numerical implementation and practical usage of modern pulse propagation models. *The European Physical Journal Special Topics*, 199(1):5–76, 2011.

[57] Robert W. Boyd, Alexander L. Gaeta, and Enno Giese. Nonlinear optics. In *Springer Handbook of Atomic, Molecular, and Optical Physics*, pages 1097–1110. Springer, 2008.

[58] Jun Ye and Steven T Cundiff. *Femtosecond optical frequency comb: principle, operation and applications*. Springer Science & Business Media, 2005.

[59] Birgitta Bernhardt. *Dual comb spectroscopy*. PhD thesis, Ludwig Maximilian University of Munich, 2011.

[60] TA Birks, WJ Wadsworth, and P St J Russell. Supercontinuum generation in tapered fibers. *Optics letters*, 25(19):1415–1417, 2000.

[61] Sarper Salman Haydar. *High -power frequency combs for precision spectroscopy in the extreme ultraviolet*. PhD thesis, University of Hamburg, 2023.

[62] T. R. Schibli, I. Hartl, D. C. Yost, M. J. Martin, A. Marcinkevičius, M. E. Fermann, and J. Ye. Optical frequency comb with submillihertz linewidth and more than 10 W average power. *Nature Photonics*, 2(6):355–359, 2008.

[63] Thomas Brabec, Misha Yu Ivanov, and Paul B Corkum. Coulomb focusing in intense field atomic processes. *Physical Review A*, 54(4):R2551, 1996.

[64] Maciej Lewenstein, Ph. Balcou, M. Yu Ivanov, Anne L'huillier, and Paul B. Corkum. Theory of high-harmonic generation by low-frequency laser fields. *Physical Review A*, 49(3):2117, 1994.

[65] Arthur Schönberg, Haydar Sarper Salman, Ayhan Tajalli, Sonu Kumar, Ingmar Hartl, and Christoph M Heyl. Below-threshold harmonic generation in gas-jets for th-229 nuclear spectroscopy. *Optics Express*, 31(8):12880–12893, 2023.

[66] J. Russell, P. Holzer, W. Chang, A. Abdolvand, and J. C. Travers. Hollow-core photonic crystal fibres for gas-based nonlinear optics. *Nat. Photon*, 8(278), 2014.

[67] Michael Müller, Joachim Buldt, Henning Stark, Christian Grebing, and Jens Limpert. Multipass cell for high-power few-cycle compression. *Optics Letters*, 46(11):2678–2681, 2021.

[68] John C. Travers, Teodora F. Grigorova, Christian Brahms, and Federico Belli. High-energy pulse self-compression and ultraviolet generation through soliton dynamics in hollow capillary fibres. *Nature Photonics*, 13(8):547–554, 2019.

[69] Laura Silletti, Ammar Bin Wahid, Esmerando Escoto, Prannay Balla, Supriya Rajhans, Katinka Horn, Lutz Winkelmann, Vincent Wanie, Andrea Trabattoni, Christoph M. Heyl, and Francesca Calegari. Dispersion-engineered multi-pass cell for single-stage post-compression of an ytterbium laser. *Optics Letters*, 48(7):1842–1845, 2023.

[70] Nour Daher, Florent Guichard, Xavier Délen, Yoann Zaouter, Marc Hanna, and Patrick Georges. Spectral compression in a multipass cell. *Optics Express*, 28(15):21571–21577, 2020.

[71] Anne-Lise Viotti, Marcus Seidel, Esmerando Escoto, Supriya Rajhans, Wim P. Leemans, Ingmar Hartl, and Christoph M. Heyl. Multi-pass cells for post-compression of ultrashort laser pulses. *Optica*, 9(2):197–216, 2022.

[72] Tamas Nagy, Martin Kretschmar, Marc J.J. Vrakking, and Arnaud Rouzée. Generation of above-terawatt 1.5-cycle visible pulses at 1 kHz by post-compression in a hollow fiber. *Optics Letters*, 45(12):3313–3316, 2020.

[73] Christoph M. Heyl, Marcus Seidel, Esmerando Escoto, Arthur Schönberg, Stefanos Carlström, Gunnar Arisholm, Tino Lang, and Ingmar Hartl. High-energy bow tie multi-pass cells for nonlinear spectral broadening applications. *Journal of Physics: Photonics*, 4(1):014002, 2022.

[74] Raymond C. Cumming. The serrodyne frequency translator. *Proceedings of the IRE*, 45(2):175–186, 1957.

[75] H. Scharfman and F. J. O'Hara. A ferrite serrodyne for microwave frequency translation. *IRE Transactions on Microwave Theory and Techniques*, 7(1):32–37, 1959.

[76] K. K. Wong, R. M. De La Rue, and S. Wright. Electro-optic-waveguide frequency translator in $LiNbO_3$ fabricated by proton exchange. *Optics letters*, 7(11):546–548, 1982.

[77] Rachel Houtz, Cheong Chan, and Holger Müller. Wideband, efficient optical serrodyne frequency shifting with a phase modulator and a nonlinear transmission line. *Optics express*, 17(21):19235–19240, 2009.

[78] D. M. S. Johnson, J. M. Hogan, S. W. Chiow, and M. A. Kasevich. Broadband optical serrodyne frequency shifting. *Optics letters*, 35(5):745–747, 2010.

[79] Ralf Kohlhaas, Thomas Vanderbruggen, Simon Bernon, Andrea Bertoldi, Arnaud Landragin, and Philippe Bouyer. Robust laser frequency stabilization by serrodyne modulation. *Optics letters*, 37(6):1005–1007, 2012.

[80] K. F. Lee and G. S. Kanter. All-optical serrodyne frequency shifter. *Optics Express*, 29(17):26608–26617, 2021.

[81] Gary Eden, Tom Galvin, and Kavita Desai. *Lecture notes on optical electronics: optical resonantor modes*. University of Illinois Urbana-Champagn, 2020.

[82] Willem Brouwer. Matrix methods in optical instrument design. *Matrix Methods in Optical Instrument Design*, 1964.

[83] Charles Fabry. Theorie et applications d'une nouvelle methods de spectroscopie intereferentielle. *Ann. Chim. Ser. 7*, 16:115–144, 1899.

[84] Alfred Perot and Charles Fabry. On the application of interference phenomena to the solution of various problems of spectroscopy and metrology. *Astrophysical Journal, vol. 9, p. 87*, 9:87, 1899.

[85] Anthony E. Siegman. *Lasers*. University science books, 1986.

[86] D. Herriott, H. Kogelnik, and R. Kompfner. Off-axis paths in spherical mirror interferometers. *Applied Optics*, 3(4):523–526, 1964.

[87] Donald R. Herriott and Harry J. Schulte. Folded optical delay lines. *Applied Optics*, 4(8):883–889, 1965.

[88] Devinder Kaur, A. M. De Souza, J. Wanna, Sameer A. Hammad, Louis Mercorelli, and David S. Perry. Multipass cell for molecular beam absorption spectroscopy. *Applied optics*, 29(1):119–124, 1990.

[89] Peter Werle, Franz Slemr, Karl Maurer, Robert Kormann, Robert Mücke, and Bernd Jänker. Near-and mid-infrared laser-optical sensors for gas analysis. *Optics and lasers in engineering*, 37(2-3):101–114, 2002.

[90] Jan Schulte, Thomas Sartorius, Johannes Weitenberg, Andreas Vernaleken, and Peter Russbueldt. Nonlinear pulse compression in a multi-pass cell. *Optics Letters*, 41(19):4511–4514, 2016.

[91] Johannes Weitenberg, Andreas Vernaleken, Jan Schulte, Akira Ozawa, Thomas Sartorius, Vladimir Pervak, Hans-Dieter Hoffmann, Thomas Udem, Peter Russbüldt, and Theodor W. Hänsch. Multi-pass-cell-based nonlinear pulse compression to 115 fs at 7.5 μJ pulse energy and 300 W average power. *Optics express*, 25(17):20502–20510, 2017.

[92] Edoardo Vicentini, Yuchen Wang, Davide Gatti, Alessio Gambetta, Paolo Laporta, Gianluca Galzerano, Kelly Curtis, Kenneth McEwan, Christopher R. Howle, and Nicola Coluccelli. Nonlinear pulse compression to 22 fs at 15.6 μJ by an all-solid-state multipass approach. *Optics express*, 28(4):4541–4549, 2020.

[93] Johannes Weitenberg, Andreas Vernaleken, Jan Schulte, Akira Ozawa, Thomas Sartorius, Vladimir Pervak, Hans-Dieter Hoffmann, Thomas Udem, Peter Russbüldt, and Theodor W. Hänsch. Multi-pass-cell-based nonlinear pulse compression to 115 fs at 7.5 μJ pulse energy and 300 W average power. *Optics express*, 25(17):20502–20510, 2017.

[94] Jiajun Song, Zhaohua Wang, Renchong Lv, Xianzhi Wang, Hao Teng, Jiangfeng Zhu, and Zhiyi Wei. Generation of 172 fs pulse from a Nd: YVO_4 picosecond laser by using multi-pass-cell technique. *Applied Physics B*, 127:1–6, 2021.

[95] Marcus Seidel, Federico Pressacco, Oender Akcaalan, Thomas Binhammer, John Darvill, Nagitha Ekanayake, Maik Frede, Uwe Grosse-Wortmann, Michael Heber, Christoph M. Heyl, and Ingmar Hartl. Ultrafast MHz-rate burst-mode pump–probe laser for the FLASH FEL facility based on nonlinear compression of ps-level pulses from an Yb-amplifier chain. *Laser & Photonics Reviews*, 16(3):2100268, 2022.

[96] Francesca Calegari, Giuseppe Sansone, Salvatore Stagira, Caterina Vozzi, and Mauro Nisoli. Advances in attosecond science. *Journal of Physics B: Atomic, Molecular and Optical Physics*, 49(6):062001, 2016.

[97] Annkatrin Sommer, E. M. Bothschafter, S. A. Sato, Clemens Jakubeit, Tobias Latka, Olga Razskazovskaya, Hanieh Fattahi, Michael Jobst, W. Schweinberger, Vage Shirvanyan, V. Shirvanyan, V. S. Yakovlev, R. Kienberger, K. Yabana, N. Karpowicz, M. Schultze, and F. Krausz. Attosecond nonlinear polarization and light–matter energy transfer in solids. *Nature*, 534(7605):86–90, 2016.

[98] Jérôme Faure, Dominikas Gustas, Diego Guénot, Aline Vernier, Frederik Böhle, Marie Ouillé, Stefan Haessler, R. Lopez-Martens, and Agustin Lifschitz. A review of recent progress on laser-plasma acceleration at kHz repetition rate. *Plasma Physics and Controlled Fusion*, 61(1):014012, 2018.

[99] Georg Schmid, Kirsten Schnorr, Sven Augustin, Severin Meister, Hannes Lindenblatt, Florian Trost, Yifan Liu, Tsveta Miteva, Mathieu Gisselbrecht, Stefan Düsterer, Harald Redlin, Rolf Treusch, Kirill Gokhberg, Alexander I. Kuleff, Lorenz S. Cederbaum, Claus Dieter Schröter, Thomas Pfeifer, and Robert Moshammer.

Tracing charge transfer in argon dimers by XUV-pump IR-probe experiments at flash. *The Journal of chemical physics*, 151(8), 2019.

[100] Georg Schmid, Kirsten Schnorr, Sven Augustin, Severin Meister, Hannes Lindenblatt, Florian Trost, Yifan Liu, Nikola Stojanovic, Alaa Al-Shemmary, Torsten Golz, Rolf Treusch, Michael Gensch, Matthias Kübel, Lutz Foucar, Artem Rudenko, Joachim Ullrich, Claus Dieter Schröter, Thomas Pfeifer, and Robert Moshammer. Terahertz-field-induced time shifts in atomic photoemission. *Physical review letters*, 122(7):073001, 2019.

[101] Joachim Ullrich, Robert Moshammer, Alexander Dorn, Reinhard Dörner, L. P. H. Schmidt, and H. Schmidt-Böcking. Recoil-ion and electron momentum spectroscopy: reaction-microscopes. *Reports on progress in physics*, 66(9):1463, 2003.

[102] F. J. Furch, T. Witting, M. Osolodkov, F. Schell, C. P. Schulz, and M. J. J. Vrakking. High power, high repetition rate laser-based sources for attosecond science. *Journal of Physics: Photonics*, 4(3):032001, 2022.

[103] Tamas Nagy, Peter Simon, and Laszlo Veisz. High-energy few-cycle pulses: post-compression techniques. *Advances in Physics: X*, 6(1):1845795, 2021.

[104] Claude Rolland and Paul B. Corkum. Compression of high-power optical pulses. *JOSA B*, 5(3):641–647, 1988.

[105] P. B. Corkum, D. Strickland, and C. Rolland. Compression of high power optical pulses. In *OSA Annual Meeting*, page FR1. Optica Publishing Group, 1989.

[106] S. Yu Mironov, S. Fourmaux, P. Lassonde, V. N. Ginzburg, S. Payeur, J. C. Kieffer, E. A. Khazanov, and G. Mourou. Thin plate compression of a sub-petawatt Ti:Sapphire laser pulses. *Applied Physics Letters*, 116(24):241101, 2020.

[107] G. Mourou, S. Mironov, E. Khazanov, and A. Sergeev. Single cycle thin film compressor opening the door to zeptosecond-exawatt physics. *The European Physical Journal Special Topics*, 223(6):1181–1188, 2014.

[108] Chih-Hsuan Lu, Yu-Jung Tsou, Hong-Yu Chen, Bo-Han Chen, Yu-Chen Cheng, Shang-Da Yang, Ming-Chang Chen, Chia-Chen Hsu, and Andrew H. Kung. Generation of intense supercontinuum in condensed media. *Optica*, 1(6):400–406, 2014.

[109] Yu-Chen Cheng, Chih-Hsuan Lu, Yuan-Yao Lin, and AH Kung. Supercontinuum generation in a multi-plate medium. *Optics express*, 24(7):7224–7231, 2016.

[110] Chih-Hsuan Lu, Tobias Witting, Anton Husakou, Marc J. J. Vrakking, A. H. Kung, and Federico J. Furch. Sub-4 fs laser pulses at high average power and high repetition rate from an all-solid-state setup. *Optics express*, 26(7):8941–8956, 2018.

[111] L. Bergé, S. Skupin, R. Nuter, Jérôme Kasparian, and Jean-Pierre Wolf. Ultrashort filaments of light in weakly ionized, optically transparent media. *Reports on progress in physics*, 70(10):1633, 2007.

[112] C. P. Hauri, A. Guandalini, P. Eckle, W. Kornelis, J. Biegert, and Ursula Keller. Generation of intense few-cycle laser pulses through filamentation–parameter dependence. *Optics Express*, 13(19):7541–7547, 2005.

[113] A. M. Zheltikov. Laser-induced filaments in the mid-infrared. *Journal of Physics B: Atomic, Molecular and Optical Physics*, 50(9):092001, 2017.

[114] A. V. Mitrofanov, A. A. Voronin, D. A. Sidorov-Biryukov, S. I. Mitryukovsky, A. B. Fedotov, E. E. Serebryannikov, D. V. Meshchankin, V. Shumakova, S. Ališauskas, A. Pugžlys, V. Ya. Panchenko, A. Baltuška, and A. M. Zheltikov. Subterawatt few-cycle mid-infrared pulses from a single filament. *Optica*, 3(3):299–302, 2016.

[115] Amelle Zair, Anna Guandalini, Florian Schapper, Mirko Holler, Jens Biegert, Lukas Gallmann, Arnaud Couairon, Michel Franco, André Mysyrowicz, and Ursulla Keller. Spatio-temporal characterization of few-cycle pulses obtained by filamentation. *Optics express*, 15(9):5394–5405, 2007.

[116] Mauro Nisoli, Sandro De Silvestri, and Orazio Svelto. Generation of high energy 10 fs pulses by a new pulse compression technique. *Applied Physics Letters*, 68(20):2793–2795, 1996.

[117] Sandro De Silvestri, Mauro Nisoli, Giuseppe Sansone, Salvatore Stagira, and Orazio Svelto. Few-cycle pulses by external compression. *Few-cycle laser pulse generation and its applications*, pages 137–178, 2004.

[118] Adrian L. Cavalieri, Eleftherios Goulielmakis, Balint Horvath, Wolfram Helml, Martin Schultze, Markus Fieß, Volodymyr Pervak, Laszlo Veisz, V. S. Yakovlev, Matthias Uiberacker, A. Apolonski, F. Krausz, and R. Kienberger. Intense 1.5-cycle near infrared laser waveforms and their use for the generation of ultra-broadband soft-x-ray harmonic continua. *New Journal of Physics*, 9(7):242, 2007.

[119] Tamas Nagy, Michael Forster, and Peter Simon. Flexible hollow fiber for pulse compressors. *Applied Optics*, 47(18):3264–3268, 2008.

[120] Jae Hee Sung, Ju-Yun Park, Tayyab Imran, Yong-Soo Lee, and Chang Hee Nam. Generation of 0.2-TW 5.5-fs optical pulses at 1 kHz using a differentially pumped hollow-fiber chirped-mirror compressor. *Applied Physics B*, 82:5–8, 2006.

[121] Juyun Park, Jae-hwan Lee, and Chang Hee Nam. Generation of 1.5 cycle 0.3 TW laser pulses using a hollow-fiber pulse compressor. *Optics letters*, 34(15):2342–2344, 2009.

[122] Yu Oishi, Akira Suda, Katsumi Midorikawa, and Fumihiko Kannari. Sub-10 fs, multimillijoule laser system. *Review of scientific instruments*, 76(9):093114, 2005.

[123] Samuel Bohman, Akira Suda, Tsuneto Kanai, Shigeru Yamaguchi, and Katsumi Midorikawa. Generation of 5.0 fs, 5.0 mJ pulses at 1khz using hollow-fiber pulse compression. *Optics letters*, 35(11):1887–1889, 2010.

[124] John E. Beetar, M. Nrisimhamurty, Tran-Chau Truong, Yangyang Liu, and Michael Chini. Thermal effects in molecular gas-filled hollow-core fibers. *Optics Letters*, 46(10):2437–2440, 2021.

[125] Elissa Haddad, Reza Safaei, Adrien Leblanc, Riccardo Piccoli, Young-Gyun Jeong, Heide Ibrahim, Bruno E. Schmidt, Roberto Morandotti, Luca Razzari, François Légaré, and Philippe Lassonde. Molecular gases for pulse compression in hollow core fibers. *Optics express*, 26(19):25426–25436, 2018.

[126] Tamas Nagy, Martin Kretschmar, Marc J.J. Vrakking, and Arnaud Rouzée. Generation of above-terawatt 1.5-cycle visible pulses at 1 kHz by post-compression in a hollow fiber. *Optics Letters*, 45(12):3313–3316, 2020.

[127] Tamas Nagy, Steffen Hädrich, Peter Simon, Andreas Blumenstein, Nico Walther, Robert Klas, Joachim Buldt, Henning Stark, Sven Breitkopf, Péter Jójárt, Imre Seres, Zoltán Várallyay, Tino Eidam, and Jens Limpert. Generation of three-cycle multi-millijoule laser pulses at 318 W average power. *Optica*, 6(11):1423–1424, 2019.

[128] T. Lang, S. Alisauskas, U. Große-Wortmann, T. Hülsenbusch, B. Manschwetus, C. Mohr, J. Müller, F. Peters, N. Schirmel, S. Schulz, A. Swiderski, J. Zheng, and I. Hartl. Versatile OPCPA pump-probe laser system for the FLASH2 XUV FEL beamline at DESY. In *The European Conference on Lasers and Electro-Optics*, page ca_2_1. Optica Publishing Group, 2019.

[129] Prannay Balla, Ammar Bin Wahid, Ivan Sytcevich, Chen Guo, Anne-Lise Viotti, Laura Silletti, Andrea Cartella, Skirmantas Alisauskas, Hamed Tavakol, Uwe Grosse-Wortmann, Arthur Schönberg, Marcus Seidel, Andrea Trabattoni, Bastian Manschwetus, Tino Lang, Francesca Calegari, Arnaud Couairon, Anne L'Huillier, Cord L. Arnold, Ingmar Hartl, and Christoph M. Heyl. Postcompression of picosecond pulses into the few-cycle regime. *Optics letters*, 45(9):2572–2575, 2020.

[130] Lars Von Der Wense, Benedict Seiferle, Mustapha Laatiaoui, Jürgen B. Neumayr, Hans-Jörg Maier, Hans-Friedrich Wirth, Christoph Mokry, Jörg Runke, Klaus Eberhardt, Christoph E. Düllmann, Norbert G. Trautmann, and Peter G. Thirolf. Direct detection of the ^{229}Th nuclear clock transition. *Nature*, 533(7601):47–51, 2016.

[131] Nikolay Minkov and Adriana Pálffy. Theoretical predictions for the magnetic dipole moment of ^{229m}Th. *Physical Review Letters*, 122(16):162502, 2019.

[132] Samuel M. Brewer, J. S. Chen, Aaron M. Hankin, Ethan R. Clements, Chin-wen Chou, David J. Wineland, David B. Hume, and David R. Leibrandt. Al^{+27} quantum-logic clock with a systematic uncertainty below 10^{-18}. *Physical review letters*, 123(3):033201, 2019.

[133] Sandro Kraemer, Janni Moens, Michail Athanasakis-Kaklamanakis, Silvia Bara, Kjeld Beeks, Premaditya Chhetri, Katerina Chrysalidis, Arno Claessens, Thomas E. Cocolios, João G.M. Correia, Hilde De Witte, Rafael Ferrer, Sarina Geldhof, Reinhard Heinke, Niyusha Hosseini, Mark Huyse, Ulli Köster, Yuri Kudryavtsev, Mustapha Laatiaoui, Razvan Lica, Goele Magchiels, Vladimir Manea, Clement Merckling, Lino M. C. Pereira, Sebastian Raeder, Thorsten Schumm, Simon Sels, Peter G. Thirolf, Shandirai Malven Tunhuma, Paul Van Den Bergh, Piet Van Duppen, André Vantomme, Matthias Verlinde, Renan Villarreal,

and Ulrich Wahl. Observation of the radiative decay of the ^{229}Th nuclear clock isomer. *Nature*, 617(7962):706–710, 2023.

[134] Teruto Kanai, Takeshi Kanda, Taro Sekikawa, Shuntaro Watanabe, Tadashi Togashi, Chuangtian Chen, Chengqian Zhang, Zuyan Xu, and Jiyang Wang. Generation of vacuum-ultraviolet light below 160 nm in a KBBF crystal by the fifth harmonic of a single-mode Ti:Sapphire laser. *JOSA B*, 21(2):370–375, 2004.

[135] C. T. Chen, G. L. Wang, X. Y. Wang, and Z. Y. Xu. Deep-uv nonlinear optical crystal $KBe_2BO_3F_2$—discovery, growth, optical properties and applications. *Applied Physics B*, 97:9–25, 2009.

[136] Tomoharu Nakazato, Isao Ito, Yohei Kobayashi, Xiaoyang Wang, Chuangtian Chen, and Shuntaro Watanabe. 149.8 nm, the shortest wavelength generated by phase matching in nonlinear crystals. In *Nonlinear Frequency Generation and Conversion: Materials and Devices XVI*, volume 10088, pages 15–24. SPIE, 2017.

[137] Tomoharu Nakazato, Isao Ito, Yohei Kobayashi, Xiaoyang Wang, Chuangtian Chen, and Shuntaro Watanabe. Phase-matched frequency conversion below 150 nm in $KBe_2BO_3F_2$. *Optics Express*, 24(15):17149–17158, 2016.

[138] Yuxuan Ma, Sarper H. Salman, Chen Li, Christoph Mahnke, Yi Hua, Stefan Droste, Jakob Fellinger, Aline S. Mayer, Oliver H. Heckl, Christoph M. Heyl, et al. Compact, all-pm fiber integrated and alignment-free ultrafast yb: fiber nalm laser with sub-femtosecond timing jitter. *Journal of Lightwave Technology*, 39(13):4431–4438, 2021.

[139] Sarper Salman, Mingqi Fan, Henrik Tünnermann, Prannay Balla, John Darvill, Dominic Laumer, Vito F. Pecile, Jakob Fellinger, Valentina Shumakova, Christoph Mahnke, Yuxuan Ma, Christian Mohr, Oliver H Heckl, Christoph M Heyl, and Ingmar Hartl. Smart and agile 88 W Yb-fiber frequency comb laser. In *European Physical Journal Web of Conferences*, volume 267, page 01057, 2022.

[140] Prannay Balla, Henrik Tünnermann, Sarper H. Salman, Mingqi Fan, Skirmantas Alisauskas, Ingmar Hartl, and Christoph M Heyl. Ultrafast serrodyne optical frequency translator. *Nature Photonics*, 17(2):187–192, 2023.

[141] Ruediger Paschotta. RP fiber power. *RP Photonics Inc.*

[142] Nicholas P. Dover, Tim Ziegler, Stefan Assenbaum, Constantin Bernert, Stefan Bock, Florian-Emanuel Brack, Thomas E Cowan, Emma J. Ditter, Marco Garten, Lennart Gaus, et al. Enhanced ion acceleration from transparency-driven foils demonstrated at two ultraintense laser facilities. *Light: Science & Applications*, 12(1):71, 2023.

[143] Na Xie, Wanqing Huang, Xiaodong Wang, Li Sun, Yi Guo, Qing Li, Runchang Zhao, and Jingqin Su. Improvement of temporal contrast for ultrashort laser pulses by cross-polarized wave generation. *Optik*, 123(7):565–568, 2012.

[144] Dario Polli, Daniele Brida, Shaul Mukamel, Guglielmo Lanzani, and Giulio Cerullo. Effective temporal resolution in pump-probe spectroscopy with strongly chirped pulses. *Physical Review A*, 82(5):053809, 2010.

[145] A. L. Viotti, Skirmantas Alisauskas, Ammar Bin Wahid, Prannay Balla, Nora Schirmel, Bastian Manschwetus, Ingmar Hartl, and Christoph M. Heyl. 60 fs, 1030 nm FEL pump–probe laser based on a multi-pass post-compressed Yb: YAG source. *Journal of synchrotron radiation*, 28(1):36–43, 2021.

[146] Ennio Arimondo, William Daniel Phillips, and Franco Strumia. *Laser manipulation of atoms and ions*, volume 118. Elsevier, 1993.

[147] R. Jason Jones, Kevin D. Moll, Michael J. Thorpe, and Jun Ye. Phase-coherent frequency combs in the vacuum ultraviolet via high-harmonic generation inside a femtosecond enhancement cavity. *Physical Review Letters*, 94(19):193201, 2005.

[148] Christoph Gohle, Thomas Udem, Maximilian Herrmann, Jens Rauschenberger, Ronald Holzwarth, Hans A. Schuessler, Ferenc Krausz, and Theodor W. Hänsch. A frequency comb in the extreme ultraviolet. *Nature*, 436(7048):234–237, 2005.

[149] Ronald W. P. Drever, John L. Hall, Frank V. Kowalski, James Hough, G. M. Ford, A. J. Munley, and H. Ward. Laser phase and frequency stabilization using an optical resonator. *Applied Physics B*, 31:97–105, 1983.

[150] T. K. Allison, A. Cingöz, D. C. Yost, and J. Ye. Extreme nonlinear optics in a femtosecond enhancement cavity. *Physical Review Letters*, 107(18):183903, 2011.

[151] Luis V. Rodríguez-de Marcos, Juan I. Larruquert, José A. Méndez, and José A. Aznárez. Self-consistent optical constants of SiO_2 and Ta_2O_5 films. *Optical Materials Express*, 6(11):3622–3637, 2016.

[152] Maximilian Högner. *Spatio-Spectrally Tailored Nonlinear Enhancement Cavities*. PhD thesis, LMU München, 2019.

[153] Arthur K. Mills, T. J. Hammond, Matthew H. C. Lam, and David J. Jones. Xuv frequency combs via femtosecond enhancement cavities. *Journal of Physics B: Atomic, Molecular and Optical Physics*, 45(14):142001, 2012.

[154] Akira Ozawa, Zhigang Zhao, Makoto Kuwata-Gonokami, and Yohei Kobayashi. High average power coherent vuv generation at 10 MHz repetition frequency by intracavity high harmonic generation. *Optics express*, 23(12):15107–15118, 2015.

[155] D. C. Yost, T. R. Schibli, and Jun Ye. Efficient output coupling of intracavity high-harmonic generation. *Optics letters*, 33(10):1099–1101, 2008.

[156] H.C. Lu, H.K. Chen, H.F. Chen, B.M. Cheng, and J.F. Ogilvie. Absorption cross section of molecular oxygen in the transition E $^3\Sigma_u^-$ v = 0 - X $^3\Sigma_g^-$ v = 0 at 38 k. *Astronomy & Astrophysics*, 520:A19, 2010.

[157] Ioachim Pupeza, M. Högner, J. Weitenberg, Simon Holzberger, D. Esser, T. Eidam, J. Limpert, A. Tünnermann, E. Fill, and Vladislav S. Yakovlev. Cavity-enhanced high-harmonic generation with spatially tailored driving fields. *Physical Review Letters*, 112(10):103902, 2014.

[158] Maximilian Högner, Tobias Saule, Stephan Heinrich, Nikolai Lilienfein, Dominik Esser, Michael Trubetskov, Volodymyr Pervak, and Ioachim Pupeza. Cavity-enhanced noncollinear high-harmonic generation. *Optics Express*, 27(14):19675–19691, 2019.

[159] Chuankun Zhang, Stephen B. Schoun, Christoph M. Heyl, Gil Porat, Mette B. Gaarde, and Jun Ye. Noncollinear enhancement cavity for record-high outcoupling efficiency of an extreme-uv frequency comb. *Physical Review Letters*, 125(9):093902, 2020.

[160] Benedict Seiferle, Lars Von Der Wense, and Peter G. Thirolf. Lifetime measurement of the ^{229}Th nuclear isomer. *Physical review letters*, 118(4):042501, 2017.

[161] S.B. Utter, P. Beiersdorfer, A. Barnes, R.W. Lougheed, J.R. Crespo López-Urrutia, J.A. Becker, and M.S. Weiss. Reexamination of the optical gamma ray decay in ^{229}Th. *Physical review letters*, 82(3):505, 1999.

[162] D. S. Richardson, D. M. Benton, D. E. Evans, J. A. R. Griffith, and G. Tungate. Ultraviolet photon emission observed in the search for the decay of the ^{229}Th isomer. *Physical review letters*, 80(15):3206, 1998.

[163] Xinxin Zhao, Yenny Natali Martinez de Escobar, Robert Rundberg, Evelyn M. Bond, Allen Moody, and David J. Vieira. Observation of the deexcitation of the ^{229m}Th nuclear isomer. *Physical review letters*, 109(16):160801, 2012.

[164] Ekkehard Peik and Kai Zimmermann. Comment on “observation of the deexcitation of the ^{229m}Th nuclear isomer”. *Physical Review Letters*, 111(1):018901, 2013.

[165] V. M. Shabaev, D. A. Glazov, A. M. Ryzhkov, C. Brandau, G. Plunien, W. Quint, A. M. Volchkova, and D. V. Zinenko. Ground-state g factor of highly charged th 229 ions: An access to the m1 transition probability between the isomeric and ground nuclear states. *Physical Review Letters*, 128(4):043001, 2022.

[166] Julian C. Berengut, Vladimir A. Dzuba, Victor V. Flambaum, and Sergey G. Porsev. Proposed experimental method to determine α sensitivity of splitting between ground and 7.6 eV isomeric states in ^{229}Th. *Physical Review Letters*, 102(21):210801, 2009.

[167] Richard P. Feynman, Robert B. Leighton, and Matthew Sands. The feynman lectures on physics: Volume i. *American Journal of Physics*, 33(9):750–752, 1965.

[168] P. Kienle. The SIS/ESR-project at GSI. *The Nuclear Equation of State: Part A: Discovery of Nuclear Shock Waves and the EOS*, 216:463, 2013.

[169] M. S. Sanjari, P. Hülsmann, F. Nolden, A. Schempp, J. X. Wu, Dinko Atanasov, F. Bosch, C. Kozhuharov, Yu A. Litvinov, P. Moritz, C. Peschke, P. Petri, D. Shubina, M. Steck, H. Weick, N. Winckler, Y. D. Zang, and Zhao T. C. A resonant schottky pickup for the study of highly charged ions in storage rings. *Physica Scripta*, 2013(T156):014088, 2013.

[170] Johannes Ullmann. *Laserspektroskopie an hochgeladenen Bismutionen zum Test der Quantenelektrodynamik*. PhD thesis, Dissertation, Jena, Friedrich-Schiller-Universität Jena, 2017.

[171] Supriya Rajhans, Praveen Kumar Velpula, Esmerando Escoto, Rob Shalloo, Bonaventura Farace, Kristjan Põder, Jens Osterhoff, Wim P. Leemans, Ingmar Hartl, and Christoph M. Heyl. Post-compression of 8.6 mJ ps-pulses from an Yb: YAG innoslab amplifier using a compact multi-pass cell. In *Advanced Solid State Lasers*, pages AW2A–6. Optica Publishing Group, 2021.

[172] Supriya Rajhans, Esmerando Escoto, Nikita Khodakovskiy, Praveen K. Velpula, Bonaventura Farace, Uwe Grosse-Wortmann, Rob J. Shalloo, Cord L. Arnold, Kristjan Põder, Jens Osterhoff, Wim P. Leemans, Ingmar Hartl, and Christoph M. Heyl. Post-compression of multi-millijoule picosecond pulses to few-cycles approaching the terawatt regime. *Optics Letters*, 48(18):4753–4756, 2023.

[173] M.J. Prandolini, R. Riedel, M. Schulz, and F. Tavella. A review of high power OPCPA technology for high repetition rate free-electron lasers. *Proceeding of FEL2014, TUA02*, 2014.

[174] V. Bagnoud, J. Hornung, M. Afshari, U. Eisenbarth, C. Brabetz, Z. Major, and B. Zielbauer. Implementation of a phase plate for the generation of homogeneous focal-spot intensity distributions at the high-energy short-pulse laser facility phelix. *High Power Laser Science and Engineering*, 7:e62, 2019.

[175] Erik Zeek, Kira Maginnis, Sterling Backus, Ulrich Russek, Margaret Murnane, Gérard Mourou, Henry Kapteyn, and Gleb Vdovin. Pulse compression by use of deformable mirrors. *Optics Letters*, 24(7):493–495, 1999.

[176] Matteo Hessel, David Budden, Fabio Viola, Mihaela Rosca, Eren Sezener, and Tom Hennigan. Optax: composable gradient transformation and optimisation, in jax! *Github*, 2020.

[177] James Bradbury, Roy Frostig, Peter Hawkins, Matthew James Johnson, Chris Leary, Dougal Maclaurin, George Necula, Adam Paszke, Jake VanderPlas, Skye Wanderman-Milne, and Qiao Zhang. Jax: composable transformations of python and numpy programs. *Github*, 2018.

ACKNOWLEDGMENTS

I express my deepest and most sincere gratitude to Dr. Christoph Heyl from the bottom of my heart for his role as my primary supervisor. I thank him for all the guidance he has provided me to perform research and for writing my dissertation. I would also like to thank him for his encouragement in participating in the spectroscopy experiment at GSI Darmstadt. I find great joy and encouragement in the fact that the publications resulting from this dissertation have contributed to the development of new research projects, the employment of new staff members, and the formation of a new research group, photonics research and innovation (PRI), directed by Dr. Christoph Heyl, at the Deutsches Elektronen-Synchrotron (DESY).

I express my deep gratitude to Dr. Ingmar Hartl, who is the group leader of the laser research and development group (FS-LA) at DESY. His efforts in facilitating our experiments and developing the high power frequency comb laser were essential to the success of this project. I also like to thank him for staying up late to repair the laser, along with Dr. Christoph Heyl at the free electron laser in Hamburg (FLASH) during our post-compression experiments. He could have easily asked someone else to do it, but he chose to do it himself. I also thank Mrs. Marianne Turczyk for all of the help and support she provided me with the administrative work.

I am grateful to Dr. Franz Kärtner for agreeing to be part of my doctoral committee at the start of this program and for the thought-provoking discussions we had during my doctoral committee meetings. I also thank Mrs. Uta Freydank for all of the help and support she provided me with the administrative work.

I am grateful to Dr. Carsen Brandau for welcoming me to participate in the experiment at GSI Darmstadt, providing a comprehensive introduction to the ESR, and taking the time to explain various parts of the experiment in detail. I would like to thank Dr. Rodolfo Sanchez for taking the time out of his busy schedule to discuss the problems with the laser.

I express my gratitude to my colleagues at the Helmholtz Institute Jena, especially to Dr. Thomas Stöhlkner, Dr. Renate Märtin and Dr. Christoph Hahn, who made this dissertation possible through the administrative support and funding.

I express my gratitude to my colleague Dr. Mingqi Fan for the collaboration in the work on the enhancement cavity, as well as for several stimulating dinner conversations we had during my doctorate. I thank Dr. Sarper H. Salman for his help with the high-power frequency comb laser as well as his willingness to change the position of the pulse shaper. I express my deep gratitude to Dr Henrik Tunnermann for his assistance with the pulse shaper, as well as sharing his insights and expertise on machine learning. I thank Mr. Ammar bin Wahid for the collaboration during the post-compression experiments at FLASH. I thank Mr. Uwe Grossmann for his extremely helpful support with the electronics needed for my experiments. He was always willing to share his expertise and propose a better alternative, which often made a big difference in the success of my experiments. I thank Dr. Tino Lang for all of the useful conversations we've had in regards to frequency conversion in a nonlinear crystal. I thank Mr. Oender Akcaalan for the help with fiber splicing and providing spare parts during my experiments. I also thank Dr. Bastian Manschwetus for his support and help with several experiments which were conducted at FLASH. I express my gratitude to my friend and colleague Dr. Skirmantas Alisauskas for his support with the AMPHOS laser during my experiments at FLASH, as well as for the several parts I had borrowed from him for several other experiments. I express my gratitude to Dr. Lutz Winkelmann and Dr. Caterina Viddoli for their suggestions and support with NX software, which was immensely helpful. I also thank them for the mechanical components for the temperature-stabilized SHG crystal mount. I express my gratitude to Dr. Marcus Seidel for his support during experiments at FLASH in DESY. I thank him for continuing the work on multi-pass cells for NEOLASE in Hannover and helping to bring the project to a successful conclusion. I also thank him for a number of interactions we have had in recent years, particularly on the topic of the damage of Kerr plates. Many thanks also to Dr. Christian Mohr, Dr. Dominic Laumer, Dr. Yuxuan Ma, Dr. Christoph Mahnke, Mr. Arthur Schöenberg, Mr. Hamed Travolka, Mr. Areeb Ahmed, Mr. John Darvill, Mr. Mindauguas Mecejus and all other colleagues at FS-LA.

I would also like to thank Dr. Guang Yang, Dr. Jiaan Zheng, Dr. Chen Li, Dr. Federico Pressacco, Dr. Esmerando Escoto, Dr. Nikita Khodakovskiy, Dr. Hanna Izabela Stawska, Ms. Supriya Rajhans, Mr. Sonu Kumar, Mr. Yannick Schroedel, Mr. Daniel Klein, Mr. Tim Lenzke, Mr. Nhat-Phi Hoang, Dr. Ayhan Tajalli Seifi, Dr. Victor Hariton and Dr. Timo F. J. Eichner for providing me with useful information that pertains to my doctorate.

I thank my collaborators Dr. Anne-Lise Viotti, Dr. Ivan Sytcevich, Dr. Chen Guo, Dr. Cord L. Arnold and Dr. Anne L'Huillier from Lund university for their extremely valuable support and help during the MPC based experiments at DESY.

I am also grateful to Ms. Laura Silletti, Dr. Andrea Cartella, Dr. Vincent Wanie, Dr. Andrea Trabattoni and Dr. Francesca Calegari for their assistance with experiments at FLASH and for their cooperation with further multi-pass cell-based experiments at FS-ATTO.

I thank Dr. Arnaud Couairon from the institut polytechnique for the many conversations we have had on the topic of the nonlinear refractive index, and for helping me to understand the Perelomov-Popov-Terent'ev model.

I thank Mr. Bjorn Hager, Mr. Markus Kowalski, Mr. Marcel Bichoff and Mr. Carten Conrad for their assistance in the fabrication of several components in the mechanical workshop. I also thank Mr. Manfred Spiwek for his work at the glass workshop and for sharing his expertise on how to protect dielectric coatings. This was essential for the experiments conducted in chapters 3 and 4.

I thank the staff at Partnership for Innovation, Education and Research (PIER) graduate school, Ms. Stefanie Tepass and Mr. Mirko Seimmens in particular, for their help and support during my time at PIER graduate school and the university of Hamburg. I thank the staff at the international office in DESY, in particluar Mrs. Steffi Killough, Ms. Anna Kazakova and Ms. Xiao Xiao for their help with the various documents with the Hamburg welcome centre.

I am especially grateful to Dr. Gleb Kutuzov and Dr. Ted Lang for their support and encouragement during my doctorate studies.

I also thank my Master's thesis supervisor, Dr. Govind Agrawal from the university of Rochester, for encouraging me to pursue a doctorate and for the refreshing conversations we have had over the last 8 years.

I express my most profound gratitude to my parents and brother, who were always encouraging and supportive throughout this entire dissertation process. I am grateful to my grandparents and my extended family for their support and help. I thank my grand-uncle Balaswamy and his wife for their continuous support throughout my education.

I express thanks and praise to the Almighty God for all the blessings I have received, including my colleagues, friends and family members.

I would like to express my gratitude to the many other people who have supported me throughout this doctorate and whose names are not mentioned here.